LEVEL

RADC-TR-79-339
Interim Report
January 1980

RADAR RESOURCES ALLOCATION STUDY

Sperry Gyroscope

F. J. Scire
W. R. Hanley

DTIC
ELECTED
JUL 2 1980

A

ROME AIR DEVELOPMENT CENTER
Air Force Systems Command
Griffiss Air Force Base, New York 13441

Best Available Copy

80 7 1 114

This report has been reviewed by the RADC Public Affairs Office (PA) and is releasable to the National Technical Information Service (NTIS). At NTIS it will be releasable to the general public, including foreign nations.

RADC-TR-79-339 has been reviewed and is approved for publication.
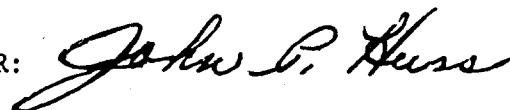
APPROVED:

DANIEL JACAVANCO
Project Engineer

APPROVED:

ALLAN C. SCHELL
Chief, Electromagnetic Sciences Division

FOR THE COMMANDER:

JOHN P. HUSS
Acting Chief, Plans Office

REPORT DOCUMENTATION PAGE		READ INSTRUCTIONS BEFORE COMPLETING FORM
1. REPORT NUMBER RADC-TR-79-339	2. GOVT ACCESSION NO. AD-A086 122	3. RECIPIENT'S CATALOG NUMBER
4. TITLE (and Subtitle) RADAR RESOURCES ALLOCATION STUDY		5. TYPE OF REPORT & PERIOD COVERED Interim Report 1 Oct 78 — 30 Sep 79
		6. PERFORMING ORG. REPORT NUMBER SG-4253-1143
7. AUTHOR(s) F. J. Scire W. R. Hanley		8. CONTRACT OR GRANT NUMBER(s) F19628-78-C-0228
9. PERFORMING ORGANIZATION NAME AND ADDRESS Sperry Gyroscope - Sperry Division Great Neck NY 11020		10. PROGRAM ELEMENT, PROJECT, TASK AREA & WORK UNIT NUMBERS 62702F 46001527
11. CONTROLLING OFFICE NAME AND ADDRESS Deputy for Electronic Technology (RADC/EEC) Hanscom AFB MA 01731		12. REPORT DATE January 1980
		13. NUMBER OF PAGES 162
14. MONITORING AGENCY NAME & ADDRESS(if different from Controlling Office) Same		15. SECURITY CLASS. (of this report) UNCLASSIFIED
		15a. DECLASSIFICATION/DOWNGRADING SCHEDULE N/A

16. DISTRIBUTION STATEMENT (of this Report)

Approved for public release; distribution unlimited.

17. DISTRIBUTION STATEMENT (of the abstract entered in Block 20, if different from Report)

Same

18. SUPPLEMENTARY NOTES

RADC Project Engineer: Daniel Jacavanco (RADC/EEC)

19. KEY WORDS (Continue on reverse side if necessary and identify by block number)

Radar Algorithms	Arctic Environment
Unattended Radar	Track Initiation/Maintenance
Automatic Operation	Baseline Radar
Computer Simulation	
Radar Resource Allocation	

20. ABSTRACT (Continue on reverse side if necessary and identify by block number)

This interim report defines an advanced technology phased array baseline radar with potential for automatically allocating its resources according to a preselected set of algorithms. Performance data of the radar, operating in a minimally adverse environment, has been generated both mathematically and from the simulation runs of integrated radar, clutter and target math models.

TABLE OF CONTENTS

TABLE OF CONTENTS - Continued

TABLE OF CONTENTS - Continued

3

LIST OF ILLUSTRATIONS

LIST OF ILLUSTRATIONS - Continued

LIST OF ILLUSTRATIONS - Continued

LIST OF TABLES

SUMMARY REPORT

This document, the first interim report on the 30-month study contract "Radar Resources Allocation Study," details the technical effort and progress made from October, 1978 to September 1979. The overall study objective is to generate an unattended radar design that will perform optimally under adverse arctic siting and environmental conditions, by developing and evaluating new techniques and algorithms for the automatic allocation of radar resources. The effectiveness of the techniques and algorithms will be judged on the radar's capability to initiate, maintain, and terminate track in accordance with the major constraints given below.

Constraints

o One false report in 30 days

o Probability of track initiation . . . 0.95 (within 16 seconds of a 0.5-meter^2 target penetrating the detection volume defined by R = 30 nmi, azimuth = 360 degrees, altitude = 100 feet) AGL to 15,000 feet)..

o Accuracy . . . . $\pm$20 degrees heading
                 $\pm$10 percent speed

o Resolution . . . . 0.5 nmi in range
                3 degrees in azimuth

The technical problem driving the system is meeting the above constraints when performing in non-optimal siting conditions containing low level penetration routes and terrain shadowing, and weather, ground, and bird clutter.

In concert with the study objectives during the initial 12 months of effort, a flexible and versatile baseline radar design has evolved, capable of rapid, automatic, and adaptive allocation of hardware and energy to perform optimally in a time-varying and spatially non-uniform environment. It is a multi-functional radar design that can provide for the efficient allocation of resources: - multiple independent steerable transmit and receive beams with position to position agility; burst-to-burst RF agility; variable prfs, beamwidths, and dwell times, adaptive signal and data processor; and hardware flexibility. As the time-varying environment is sensed, each of the flexible system parameters can be tailored adaptively to values required for optimum performance at each beam position.

Algorithms[1] have been generated for the baseline system to insure adequate performance in the minimally adverse environment of optimal siting,

— — — — — — —

[1]Section 3

and ground, sea, and rain clutter. This group of algorithms enables a track-while-scan mode of operation to meet environment performance requirements through its adaptive decision-making logic and for correlating, tracking and reporting targets in noise and clutter. The algorithms provide for (1) burst-to-burst frequency/prf waveform selection and scheduling to maximize detectability, (2) resolution of ambiguities, (3) suppression of clutter, and (4) track logic associated with window size, initiation, maintenance, and termination. Both mathematical analysis and simulated performance evaluation demonstrate, for this optimally sited radar, the detection and track-while-scan performance capability against penetrators in a cluttered environment. However, a preliminary examination of proposed arctic radar siting and terrain irregularities indicate that greater TEM flexibility than is available in a track-while-scan system is necessary. For this topography, targets can only be detected in narrow visibility gaps along the penetration route requiring higher data rates,[2] additional energy, and possibly doppler waveform tailoring. Discrimination against birds is also expected to utilize tailored radar parameters in extracting any identifying bird/flock signatures. An initial set of candidate algorithms that will be evaluated against adverse environment, siting, and terrain problems is included in the report.

The baseline radar subsystem descriptions which have provided the necessary inputs for the performance simulation/analysis, power consumption, and reliability are also included.

------

[2]Figures 12 and 13

10

Section 1

INTRODUCTION

During the past twelve month period, a phased array baseline radar was defined, modeled, and tested in a minimally adverse environment. The radar contains state-of-the-art features, which provide the necessary flexibility to permit the automatic and adaptive allocation of resources as required in a changing environment. The environment for this study varies from an optimally sited radar with minimal clutter effects to a non-optimally sited radar with terrain shadowing, multipath, and excessive non-homogeneous weather and clutter effects. The follow-on effort will proceed to develop and evaluate algorithms and techniques required to extend the baseline performance to that which will perform optimally in an adverse arctic environment.

This report is organized into five sections plus appendices. Section 2 describes the baseline radar system, defining and outlining the operating parameters, characteristics, and features. The section also includes the search, track and operational modes, followed by the radar's performance in ground, sea, and rain clutter. Section 3 details the baseline radar algorithms that are required to insure automatic and adaptive operation while meeting the performance requirements. These algorithms define the decision-making logic and resources allocated for search, initiate/maintain track, smoothing and prediction, discrimination, overload, and coast. Technical discussions of all the major baseline radar subsystems are provided in Section 4. Its contents detail the information necessary to evaluate system and subsystem performance, and to determine power consumption and reliability factors. The computer simulation effort is presented in Section 5. The development of the radar functional relationships between input signal, noise, and clutter to output detection probability and false-alarm probability (for pulse bursts and selected signal processing) is discussed. Additionally, this section describes how these functional relationships are integrated with the set of baseline algorithms and environmental models for radar test and evaluation against target scenarios in a minimally adverse arctic environment. Performance data in terms of heading and speed accuracy for targets in ground and/or rain clutter are presented. Reliability analysis follows in Section 6, with resultant plots of probability of success and mean-time-between failure as a function of the site maintenance interval.

Section 2

BASELINE RADAR SYSTEM

2.1 BASELINE DESIGN DRIVING FACTORS

The primary driving factors leading to the baseline radar design are the performance specifications for a short range, air surveillance radar operation in a relatively benign version of an arctic environment, and utilization of advanced technology hardware with flexible architectures which permit automatic allocation of radar resources to optimize performance. In operation, however, the radar system is essentially unmanaged in order to provide a basis for evaluation, comparison, and ranking of allocation strategies. To provide a realistic comparison base, some automatic features such as clutter threshold maps and a priori tailoring of transmitted power and antenna beam patterns with elevation are incorporated to meet performance requirements. Radar design synthesis studies focused on meeting the performance specification with design trade-off factors of flexible architecture, unattended arctic operation, low prime power, and system cost - weighted in that order.

Features of the baseline which make it flexible and adaptable to resource allocation include an electronic scan antenna, solid state modular transmitter, distributed data processing, modular signal processor, and software controlled space-time-energy management. The antenna contains column array networks which form three beams in elevation and are electronically step-scanned in azimuth. While these beams are simultaneously pulsed and uniformly scanned in azimuth as a shaped fan beam, each beam has the potential for individual control by modification of switching networks. The modular transmitter is all solid state, with redundancy for reliability, and it is capable of coherent transmission with waveform and frequency diversity. Variable distribution of power between beams, if desirable, can be achieved with additional switching circuitry. The digital signal processor includes pulse compression, MTI, doppler filtering, hard limiting CFAR, beam time sharing error correction codes, and self-healing redundancy. As a major system element, it is presently configured in a minimum power, maximum reliability configuration. As other waveform diversity and allocation strategies are evaluated, the incremental power consumption, reliability degradation, and processor costs will be evaluated and traded off against increased performance/efficiency. Waveform selection, frequency, beam pointing, and scheduling is controlled by the data processor, which also performs some video processing and essentially all of the track processing. The baseline radar only implements a constant azimuth scan rate with a preselected waveform and frequency pattern similar to a rotating antenna system. More complex and responsive control can readily be implemented by software or firmware changes.

2.2 BASELINE RADAR DESCRIPTION

The RRAS baseline radar is an automatic, unattended, L-band cylindrical array radar performing a low altitude, track-while-scan (TWS) air

surveillance mission in a minimally adverse arctic environment. The radar physical configuration is illustrated in figure 1. A cylindrical antenna aperture, 24 feet in diameter and 12 feet high, is mounted on a 100-foot tower. The cylinder is capped by a protective dome which provides a sheltered environment for electronic equipment and for maintenance personnel who periodically access the antenna from an entry hatch in the floor. The array is fed by 180 column networks which form a 3-beam elevation stack. The stack is scanned in azimuth by a switching network which activates groups of 45 columns. The networks occupy a ring inside the array leaving space in the center for azimuth distribution networks, solid state transmit modules, and radar electronics.

Radar system parameters, table 1, are designed to detect a 0.5-square meter cruise missile at 30 nmi. The waveform and initiate track criterion provides a 0.95 probability of track initiation within 16 seconds of penetrating the detection contour. TWS on a minimum of 20 targets is provided in the baseline.

The basic operating mode of the baseline radar is a 4-second data rate TWS surveillance of a 360-degree azimuth, 60-nmi maximum range, 15,000-foot altitude, 30-degree elevation coverage volume. A 3-beam elevation stack is scanned in one hundred-twenty 3-degree steps with four 9-pulse bursts transmitted per beam position. The basic waveform is a coherent 9-pulse burst which is used in all beam positions. One pulse is transmitted to illuminate second-time clutter, and the remaining eight are coherently processed to generate eight doppler filters. It has been postulated for the baseline because it is representative of the waveforms required to operate in the expected arctic environment. The coherent processing provides land, sea, and weather clutter rejection, and, in addition, multiple filter outputs provide doppler resolution for isolating effects of non-cancellable bird clutter or excessive local storms. All three elevation beams are pulsed simultaneously to form a composite transmit pattern and then are received individually on separate beams. Each burst in the beam is at a different frequency and prf. A large prf shift is programmed to cover blind speeds; a small prf increment is programmed to permit resolution of range ambiguities.

The solid state transmitter is a two-stage, modular design with built-in test, redundancy, and automatic self-healing features. It consists of a solid state driver stage and 45 transmit power amplifiers which are integrated with the antenna feed network. The driver generates power for three azimuth power distribution networks, with each one dedicated to a separate elevation beam. Since the upper two beams require very little power, no further amplification is necessary, and the 45 network output ports are successively switched to 45 column networks to scan the beam. In the long range, low elevation beam, high power requirements are provided by 45 transmit power amplifiers located at the output ports of the low beam azimuth network. The aperture illumination taper in azimuth is implemented by amplitude control on the power amplifier outputs. A 3-degree azimuth beamwidth is achieved by radiating from 45 column networks. A 4-second data rate is achieved by scanning in 3-degree steps, allowing 4 bursts/scan.

14

UNATTENDED RADAR

180 COLUMN NETWORKS

ANTENNA
NETWORK
CABINET

BEAM
STEERING
CONTROL
CABINET

RADOME

ENTRY
HATCH

SIGNAL
PROCESSOR
& DATA
PROCESSOR

RECEIVER
TEST CONSOLE
STATUS
DISPLAY

SOLID STATE
TRANSMITTER

FLOOR PLAN
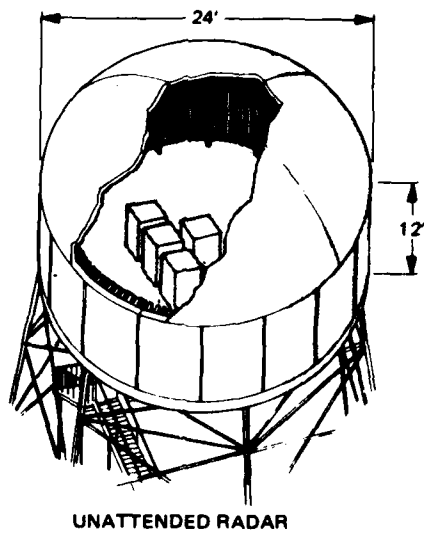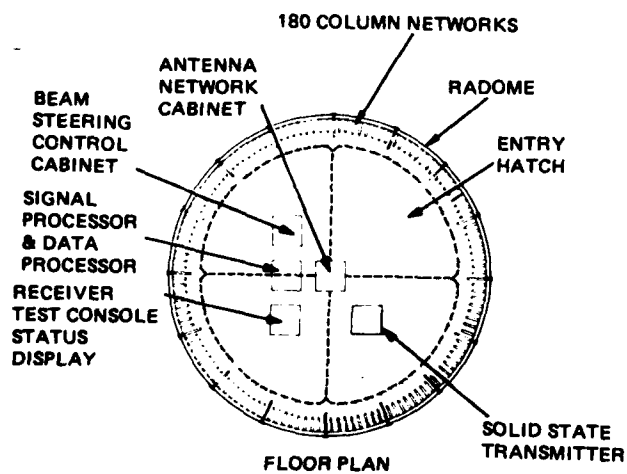
Figure 1.   Baseline Radar, Physical Configuration

Table 1.   RRAS Baseline Radar Parameters and Characteristics

Frequency	1215 - 1400 MHz
Frequency Diversity	25 frequencies preprogrammed as 16 pairs

Coverage   - Azimuth
            Elevation
            Range
            Height
	360 deg
	-1 to 30 deg
	5 to 60 nmi
	100 ft AGL to 15,000 ft

Resolution - Azimuth
            Elevation
 	
            Range
	3 deg
	30-deg transmit beam
	6.75-deg, 8.0-deg, 14.5-deg receive beams
	1/6 nmi (2 usec)

Frame Time	4 seconds - 120 beam positions
Waveforms	9-pulse burst 64-usec transmit pulse 2-usec compressed pulse Burst prf's: 1239, 1231, 982, 976 pps

Transmitter
   Peak Power per Beam
   Total Average Power
	Solid state modules
	2450, 382, 93 watts
	202 watts

Antenna	Cylindrical array 3 elevation beams

BW (deg)	Gain (dB)	Tilt (deg)
6.75	30.5	2.5
8.0	28.9	11.1
14.5	27.0	24.1

12-ft high aperture
24-ft diameter
180 columns

Sidelobes Azimuth	-25 dB first sidelobe (transmit and receive)
Receiver Channels	3 (1 per elevation beam)
Noise Figure	2 dB

Table 1. RRAS Baseline Radar Parameters and Characteristics (Cont'd)

Signal Processor	Parallel processing of 2 channels (mid and high beams are time shared) 8 parallel doppler filters 32:1 linear pulse compression 1-usec range sampling Limiting CFAR, doppler filters 1-7 Clutter threshold map (doppler filter 0) Receiver automatic noise leveling
Tracking	Track-while-scan
Number of Tracks	Greater than 20
Track Accuracy	$\pm$ 20 deg heading $\pm$ 10% speed
False Track Rate	1 in 30 days
Detection Range	30 nmi
Target RCS	0.5 meter^2 Swerling I
Detection Probability	0.9 per scan (4 burst cumulative)
Pfa	1×10^{-5}/cell/scan

The receiver, figure 2, contains three channels, one for each elevation beam. Each channel provides automatic stand-by redundancy after the low noise stage. The receiver incorporates a 2 dB noise figure, STC, BITE, and a digital output to the signal processor. The signal processor is a 3-channel, digital doppler filter providing pulse compression, hard limiting CFAR, adapter clutter threshold maps, error correction codes, and self-healing redundancy. One channel is dedicated to the lower beam, a second channel is time shared by the upper two beams, and the third channel is stand-by redundant. A three-pulse MTI in the initial doppler processing cancels large clutter and reduces dynamic range requirements in the remaining processing. CFAR digital outputs are buffered for adjacent beam, data collapsing logic.

Twenty-five crystal controlled frequencies are synthesized for psuedo-random selections on successive pulse bursts. The maximum prf is determined by a 60-nmi requirement, and the minimum prf is selected to move the first blind speed beyond 400 meters per second. Frequencies and prf's are selected in pair to maintain blind speed coverage while providing burst-to-burst frequency diversity. Sixteen pairs of frequencies are selected randomly.

2.3 RADAR PERFORMANCE

2.3.1 Search and Track Initiate

The detection performance of the RRAS baseline system is based on a detection criterion of 0.9 Pd per scan, a 10^{-5} Pfa per scan, a 0.95 probability of track initiate in 4 scans (16 seconds), and a false track initiate rate of 1 in 30 days. To achieve the 0.9 Pd per scan, four pulse bursts per beam are transmitted with frequency diversity to decorrelate a Swerling I target and convert it into a Swerling II target with burst-to-burst fluctuation. Since one burst detection out of four bursts per scan is used, the corresponding Pfa per burst must be 0.25×10^{-5} to meet the 10^{-5} Pfa per scan goal. The 0.9 Pd/scan yields a 0.95 probability of track initiate for a 3 out of 4 scan detection criterion. Using the same criterion, the 10^{-5} Pfa per scan provides a false track initiate rate of less than 1 in 30 days. To achieve a 0.9 Pd/scan on a 1 out of 4 cumulative, the single burst Pd must be 0.44. At a Pfa of 0.25×10^{-5}, the corresponding S/N requirement is 11.7 dB.

Blake charts detailing the parameters required to achieve this S/N are shown in tables 2, 3, 4. Corresponding loss budgets are detailed in table 5. These calculations treat each beam independently assuming no interaction between beams. The latter effect will be illustrated below. The visibility factor on the Blake chart is the single pulse S/N required for detection. The 11.7 dB S/N required assumes coherent integration of 8 pulses. For the 9-pulse burst, only the last 8 pulses are coherently processed. The first bulse is transmitted only for the purpose of illuminating the second-time-around clutter so that all 8 returns have the same second-time clutter. Because of the doppler filter weighting, the coherent integration is less than ideal, and the difference is included in the processing loss budget. The 2.7 dB visibility factor is therefore computed by subtracting the entire 8-pulse integration gain (9 dB) from 11.7 dB. A beam shape loss in azimuth of 2.2 dB is also included to make the calculation represent the average or expected value of detection performance. An elevation beam shape loss is not included because the calculation is made specifically for the beam peak in elevation, and the gain variation will be accounted for deterministically in computing the elevation coverage profile. The resulting range at the peak of the first beam is 32.5 nmi.

In the baseline system, the three elevation beams are pulsed simultaneously, and the power adds coherently in space to modify the coverage patterns. A 60-degree phase angle is introduced between beams to avoid nulls due to cancellation and to provide the best fill-in between beams. An elevation coverage diagram for the simultaneously pulsed transmit beam is shown in figure 3. The nominal coverage of the profile is 30 nmi in range, 15,000 feet in altitude, and 30 degrees in elevation. The plot takes into account a beam shape loss in azimuth, a variation in atmospheric loss with range, and a detectability loss due to STC.
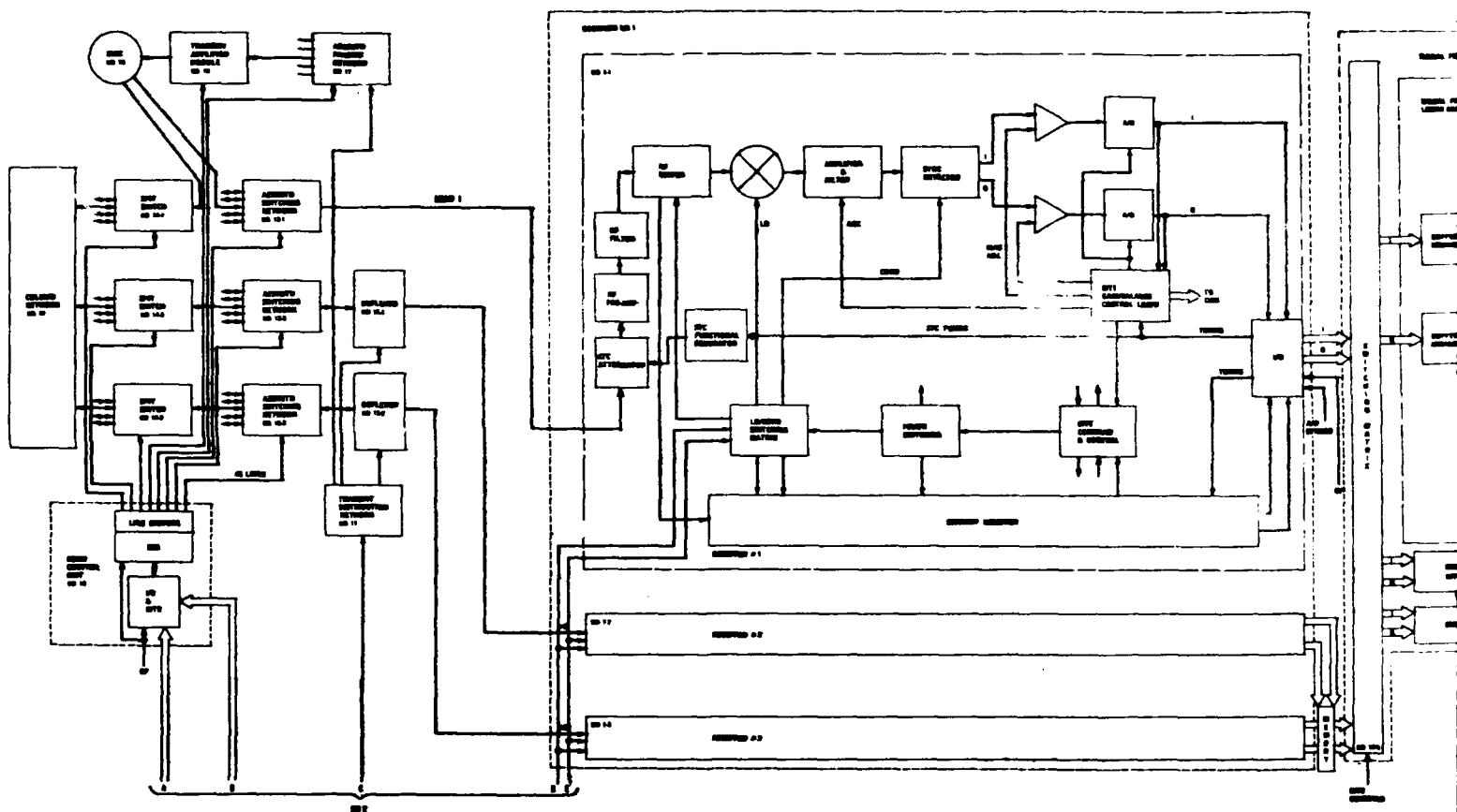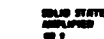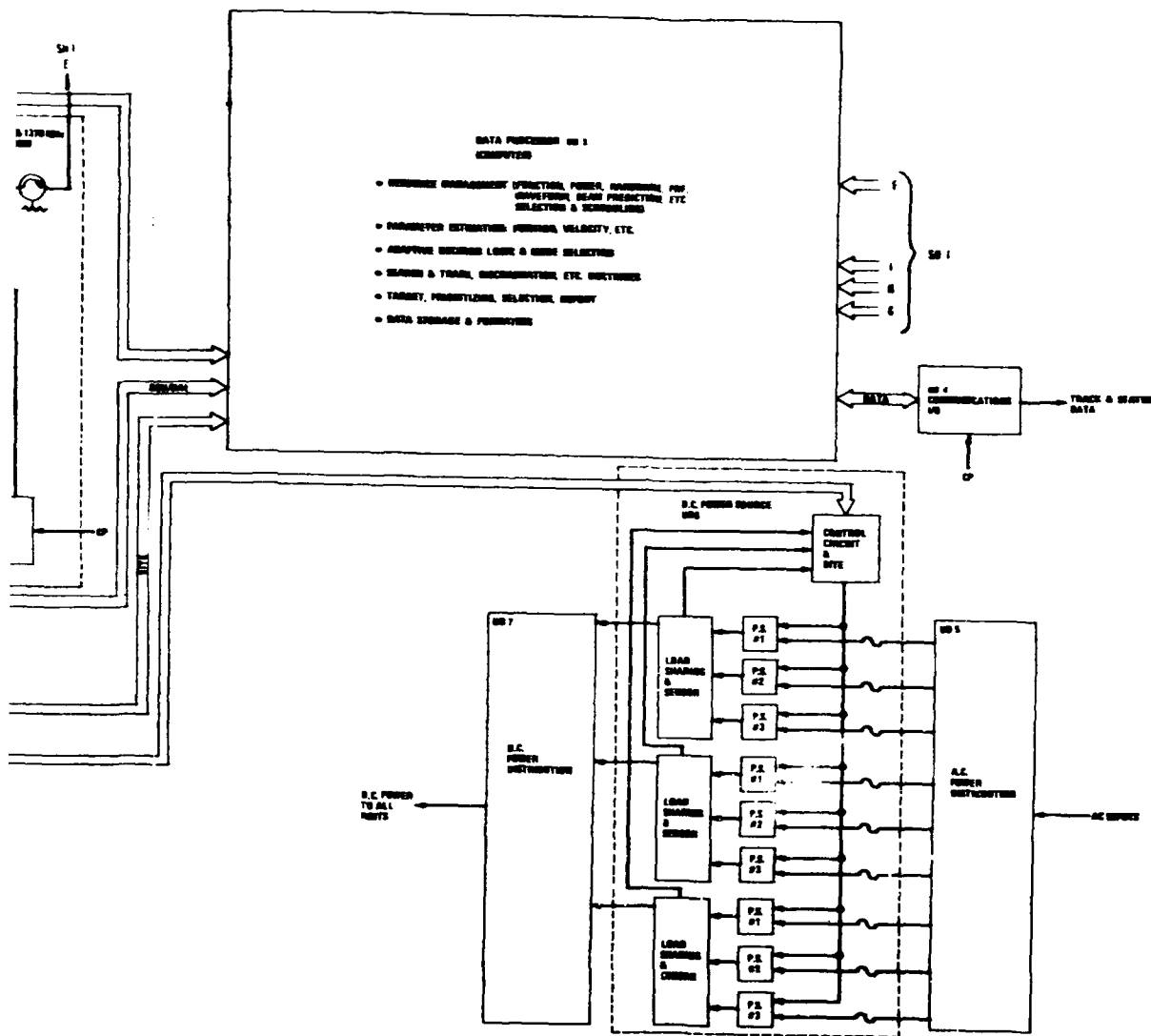
18

1

Figure 2. NBAS Baseline System
Block Diagram (1 of 2)

19

20

1

Figure 2. KRAS Baseline System
Block Diagram (2 of 2)

Table 2. RRAS Baseline - Low Beam at 2.5 Degrees

PULSE-RADAR RANGE-CALCULATION WORK SHEET

1. Compute the system input noise temperature T_s, following the outline in section A below.
2. Enter range factors known in other than decibel form in section B below, for reference.
3. Enter logarithmic and decibel values in section C below, positive values in the plus column and negative values in the minus column. For example, if $V_{o(dB)}$ as given by Figs. 4 through 9 is negative, then $-V_{o(dB)}$ is positive and goes in the plus column.

Radar antenna height: $h =$ ____ ft.   Target elevation angle: $\theta = 2.5°$.

A. Computation of T_s:	B. Range Factors		C. Decibel Values	Plus (+)	Minus (−)
$T_s = T_a + T_r + L_r T_e$	$P_{t(kW)}$	2.45	$10 \log P_{t(kW)}$	3.89	.
(a) Compute T_a.	$\tau_{\mu sec}$	64	$10 \log \tau_{\mu sec}$	18.06	
For $T_{tg} = T_{ta} = 290$ and	G_t	30.5 dB	$G_{t(dB)}$	30.5	.
$T_d = 36$ use Eq. (37a).	G_r	30.5 dB	$G_{r(dB)}$	30.5	.
Read T_a' from Fig. 11.	$\sigma_{(sq\,m)}$	0.5	$10 \log \sigma$	.	3.01
$L_{a(dB)}$: __2.3__ L_a: __1.7__	f_{MHz}	1300	$-20 \log f_{MHz}$	.	62.28
$T_a = (0.876\,T_a' - 254)/L_a + 290$	$T_s\ (°K)$	772.6	$-10 \log T_s$	.	28.88
90°K $\boxed{T_a = 186.9\,°K}$	V_o	2.7 dB	$-V_{o(dB)}$	.	2.7
(b) Compute T_r using Eq. (40).	C_B	5.2 dB	$-C_{B(dB)}$	////	5.2
For $T_{tr} = 290$ use Table 1.	L_t	0.0 dB	$-L_{t(dB)}$	////	0.0
$L_{r(dB)}$: __2.8__ $\boxed{T_r = 262.6\,°K}$	L_p	2.2 dB	$-L_{p(dB)}$	////	2.2
	L_x	2.0 dB	$-L_{x(dB)}$	////	2.0
(c) Compute T_e using Eq. (41)	Range-equation constant (40 log 1.292)			4.45	////
or using Table 1.	4. Obtain the column totals ⟶			87.40	106.27
$F_{n(dB)}$: __2.0__ T_e: __169.6__ °K	5. Enter the smaller total below the larger ⟶			.	87.40
L_r: __1.905__ $\boxed{L_r T_e = 323.2\,°K}$	6. Subtract to obtain the net decibels (dB) ⟶			. (+)	−18.87 (−)
Add. $\boxed{T_s = 772.6\,°K}$	7. In Table 2 find the range ratio corresponding to this net decibel (dB) value, taking its sign (±) into account. Multiply this ratio by 100. This is R_0 ⟶				$\boxed{33.75}$

8. Multiply R_0 by the pattern-propagation factor $\boxed{F =}$ (see Eqs. (42) through (65) and Figs. 12 through 19):

$R_0 \times F = R'$ ⟶ $\boxed{}$

9. On the appropriate curve of Figs. 21 and 22 determine the atmospheric-absorption loss factor, $L_{a(dB)}$, corresponding to R'. This is $L_{a(dB)(1)}$. ⟶ $\boxed{0.65}$

10. Find the range factor δ_1 corresponding to $-L_{a(dB)(1)}$ from the formula $\delta = $ antilog $(-L_{a(dB)}/40)$ or by using Table 2. ⟶ $\boxed{0.963}$

11. Multiply R' by δ_1. This is a first approximation of the range R_1. ⟶ $\boxed{}$

12. If R_1 differs appreciably from R', on the appropriate curve of Figs. 21 and 22, find the new value of $L_{a(dB)}$ corresponding to R_1. This is $L_{a(dB)(2)}$. ⟶ $\boxed{}$

13. Find the range-increase factor (Table 2) corresponding to the difference between $L_{a(dB)(1)}$ and $L_{a(dB)(2)}$. This is δ_2. ⟶ $\boxed{}$

14. Multiply R_1 by δ_2. This is the radar range in nautical miles, R. ⟶ $\boxed{32.5\ nmi}$

Note: If the difference between $L_{a(dB)(1)}$ and $L_{a(dB)(2)}$ is less than 0.1 dB, R_1 may be taken as the final range value, and steps 12 through 14 may be omitted. If $L_{a(dB)(1)}$ is less than 0.1 dB, R' may be taken as the final range value, and steps 9 through 14 may be omitted. (For radar frequencies up to 10,000 megahertz, correction of the atmospheric attenuation beyond the $L_{a(dB)(2)}$ value would amount to less than 0.1 dB.)

21

Table 3. RRAS Baseline - Mid Beam at 11.1 Degrees

PULSE-RADAR RANGE-CALCULATION WORK SHEET

1. Compute the system input noise temperature T_s, following the outline in section A below.
2. Enter range factors known in other than decibel form in section B below, for reference.
3. Enter logarithmic and decibel values in section C below, positive values in the plus column and negative values in the minus column. For example, if $V_{0(dB)}$ as given by Figs. 4 through 9 is negative, then $-V_{0(dB)}$ is positive and goes in the plus column.

Radar antenna height: $h =$ ___ ft.   Target elevation angle: $\theta = 11.1°$.

A. Computation of T_s:		B. Range Factors		C. Decibel Values	Plus (+)	Minus (-)
$T_s = T_a + T_r + L_r T_e$		$P_{t(kW)}$	0.382	$10 \log P_{t(kW)}$	.	4·18
(a) Compute T_a.		$\tau_{\mu sec}$	64	$10 \log \tau_{\mu sec}$	18·06	.
For $T_{tg} = T_{ta} = 290$ and		G_t	28.9 dB	$G_{t(dB)}$	28·9	.
$T_g = 36$ use Eq. (37a).		G_r	28.9 dB	$G_{r(dB)}$	28·9	.
Read T_a' from Fig. 11.		$\sigma_{(sq\,m)}$	0.5	$10 \log \sigma$	.	3·01
		f_{MHz}	1300	$-20 \log f_{MHz}$	.	62·28
$L_{a(dB)}: 3.2$ $L_a: 2.09$		T_s (°K)	724.9	$-10 \log T_s$	.	28·60
$T_a = (0.876 T_a' - 254) L_a + 290$		V_0	2.7 dB	$-V_{0(dB)}$	.	2·7
$24°K$ $\boxed{T_a = 178.5 \text{ °K}}$		C_B	5.2 dB	$-C_{B(dB)}$	////////	5.2
		L_t	2.8 dB	$-L_{t(dB)}$	////////	2·8
(b) Compute T_r using Eq. (40).		L_p	2.2 dB	$-L_{p(dB)}$	////////	2·2
For $T_{tr} = 290$ use Table 1.		L_x	2.0 dB	$-L_{x(dB)}$	////////	2·0
$L_{r(dB)}: 2.6$ $\boxed{T_r = 237.7 \text{ °K}}$		Range-equation constant (40 log 1.292)			4.45	////////
		4. Obtain the column totals ────►			80.31	112·97
(c) Compute T_e using Eq. (41)		5. Enter the smaller total below the larger─►			.	80·31
or using Table 1.		6. Subtract to obtain the net decibels (dB) ──►			. (+)	-32·66 (-)

$F_{n(dB)}: 2.0$ $T_e: 169.6$ °K

$L_r: 1.82$ $\boxed{L_r T_e = 308.7 \text{ °K}}$

Add. $\boxed{T_s = 724.9 \text{ °K}}$

7. In Table 2 find the range ratio corresponding to this net decibel (dB) value, taking its sign (±) into account. Multiply this ratio by 100. This is R_0 ──► $\boxed{15.26}$

8. Multiply R_0 by the pattern-propagation factor $\boxed{F = \quad}$ (see Eqs. (42) through (65) and Figs. 12 through 19): $R_0 \times F = R'$ ──► $\boxed{\quad}$

9. On the appropriate curve of Figs. 21 and 22 determine the atmospheric-absorption loss factor, $L_{a(dB)}$, corresponding to R' This is $L_{a(dB)(1)}$ ──► $\boxed{0.30}$

10. Find the range factor δ_1 corresponding to $-L_{a(dB)(1)}$ from the formula $\delta = $ antilog $(-L_{a(dB)} 40)$ or by using Table 2. ──► $\boxed{0.983}$

11. Multiply R' by δ_1. This is a first approximation of the range R_1. ──► $\boxed{\quad}$

12. If R_1 differs appreciably from R', on the appropriate curve of Figs. 21 and 22, find the new value of $L_{a(dB)}$ corresponding to R_1. This is $L_{a(dB)(2)}$. ──► $\boxed{\quad}$

13. Find the range-increase factor (Table 2) corresponding to the difference between $L_{a(dB)(1)}$ and $L_{a(dB)(2)}$. This is δ_2. ──► $\boxed{\quad}$

14. Multiply R_1 by δ_2. This is the radar range in nautical miles, R. ──► $\boxed{15.0 \text{ nmi}}$

Note: If the difference between $L_{a(dB)(1)}$ and $L_{a(dB)(2)}$ is less than 0.1 dB, R_1 may be taken as the final range value, and steps 12 through 14 may be omitted. If $L_{a(dB)(1)}$ is less than 0.1 dB, R' may be taken as the final range value, and steps 9 through 14 may be omitted. (For radar frequencies up to 10,000 megahertz, correction of the atmospheric attenuation beyond the $L_{a(dB)(2)}$ value would amount to less than 0.1 dB.)

22

Table 4. RRAS Baseline - High Beam at 24.1 Degrees

PULSE-RADAR RANGE-CALCULATION WORK SHEET

1. Compute the system input noise temperature T_s, following the outline in section A below.

2. Enter range factors known in other than decibel form in section B below, for reference.

3. Enter logarithmic and decibel values in section C below, positive values in the plus column and negative values in the minus column. For example, if $V_{0(dB)}$ as given by Figs. 4 through 9 is negative, then $-V_{0(dB)}$ is positive and goes in the plus column.

Radar antenna height: $h =$ ft.		Target elevation angle: $\theta = 24.1°$.		
A. Computation of T_s:	**B. Range Factors**	**C. Decibel Values**	**Plus (+)**	**Minus (−)**
$T_s = T_a + T_r + L_r T_e$	$P_{t(kW)}$ 0.093	$10 \log P_{t(kW)}$	.	10·30
(a) Compute T_a.	$\tau_{\mu sec}$ 64	$10 \log \tau_{\mu sec}$	18·06	.
For $T_{tg} = T_{ta} = 290$ and	G_t 27.0 dB	$G_{t(dB)}$	27·0	.
$T_g = 36$ use Eq. (37a).	G_r 27.0 dB	$G_{r(dB)}$	27·0	.
Read T_a' from Fig. 11.	$\sigma_{(sq\,m)}$ 0.5	$10 \log \sigma$	.	3·01
$L_{a(dB)}$: 2.5 L_a: 1.78	f_{MHz} 1300	$-20 \log f_{MHz}$	.	62·28
$T_a = (0.876\,T_a' - 254)/L_a + 290$	T_s (°K) 702.4	$-10 \log T_s$	.	28·47
18°K $T_a = 156.0°K$	V_0 2.7 dB	$-V_{0(dB)}$	.	2·7
	C_B 5.2 dB	$-C_{B(dB)}$	///	5·2
	L_t 2.8 dB	$-L_{t(dB)}$	///	2·8
(b) Compute T_r using Eq. (40).	L_p 2.2 dB	$-L_{p(dB)}$	///	2·2
For $T_{tr} = 290$ use Table 1.	L_x 2.0 dB	$-L_{x(dB)}$	///	2·0
$L_{r(dB)}$: 2.6 $T_r = 237.7°K$	Range-equation constant (40 log 1.292)		4.45	///
	4. Obtain the column totals ————→		76·51	118·96
(c) Compute T_e using Eq. (41) or using Table 1.	5. Enter the smaller total below the larger→		.	76·51
	6. Subtract to obtain the net decibels (dB)—→		. (+)	−42·45 (−)
$F_{n(dB)}$: 2.0 T_e: 169.6°K	7. In Table 2 find the range ratio corresponding to this net decibel (dB) value, taking its sign (±) into account. Multiply this ratio by 100. This is R_0 —→			8.68
L_r: 1.82 $L_r T_e = 308.7K$				
Add. $T_s = 702.4°K$	8. Multiply R_0 by the pattern-propagation factor (see Eqs. (42) through (65) and Figs. 12 through 19): $F =$			
	$R_0 \times F = R'$ ——————			

9. On the appropriate curve of Figs. 21 and 22 determine the atmospheric-absorption loss factor, $L_{a(dB)}$, corresponding to R' This is $L_{a(dB)(1)}$. —————→ **0.17**

10. Find the range factor δ_1 corresponding to $-L_{a(dB)(1)}$ from the formula $\delta = $ antilog $(-L_{a(dB)}/40)$ or by using Table 2. —————→ **0.990**

11. Multiply R' by δ_1. This is a first approximation of the range R_1. —————→ [ ]

12. If R_1 differs appreciably from R', on the appropriate curve of Figs. 21 and 22, find the new value of $L_{a(dB)}$ corresponding to R_1. This is $L_{a(dB)(2)}$. —————→ [ ]

13. Find the range-increase factor (Table 2) corresponding to the difference between $L_{a(dB)(1)}$ and $L_{a(dB)(2)}$. This is δ_2. —————→ [ ]

14. Multiply R_1 by δ_2. This is the radar range in nautical miles, R. —————→ **8.6 nmi**

Note: If the difference between $L_{a(dB)(1)}$ and $L_{a(dB)(2)}$ is less than 0.1 dB, R_1 may be taken as the final range value, and steps 12 through 14 may be omitted. If $L_{a(dB)(1)}$ is less than 0.1 dB, R' may be taken as the final range value, and steps 9 through 14 may be omitted. (For radar frequencies up to 10,000 megahertz, correction of the atmospheric attenuation beyond the $L_{a(dB)(2)}$ value would amount to less than 0.1 dB.)

23

Table 5. RRAS Baseline Radar Loss Budget (in dB)

LOSSES

Antenna	Low Beam	Mid Beam	High Beam
Column Network	0.8	0.8	0.8
Orthogonality	0.3	1.2	0.5
Cable	0.7	0.7	0.7
SP4T Switch	0.5	0.5	0.5
Antenna Ohmic Losses (L_a)	2.3	3.2	2.5

Transmit Microwave

	Low Beam	Mid Beam	High Beam
Azimuth Switching Network	0	1.8	1.8
Duplexer	0	0.5	0.5
Transmit Distribution Network	0	0.5	0.5
Total Transmit Microwave (L_t)	0	2.8	2.8

Receive Microwave

	Low Beam	Mid Beam	High Beam
Circulator	0.7	-	-
Azimuth Switching Network	1.8	1.8	1.8
Cable	0.3	0.3	0.3
Duplexer	-	0.5	0.5
Total Receive Microwave (L_r)	2.8	2.6	2.6

Processing

	Low Beam	Mid Beam	High Beam
Amplitude Quantization	0.2	0.2	0.2
P.C. Loss Due to Sampling, Doppler Mismatch, and Weighting	1.2	1.2	1.2
Doppler Filter Loss	2.6	2.6	2.6
CFAR Limiter	1.2	1.2	1.2
Total Processing (C_b)	5.2	5.2	5.2

	Low Beam	Mid Beam	High Beam
Beam Shape (L_p)	2.2	2.2	2.2
Miscellaneous (L_x)	2.0	2.0	2.0
Atmospheric (L_a)	0.65	0.30	0.17
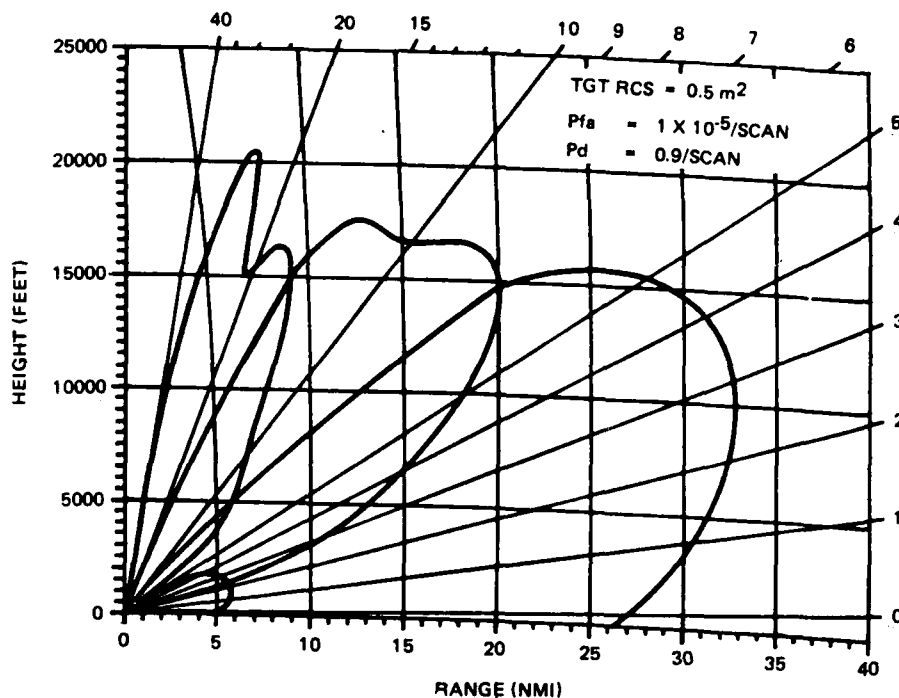
Figure 3. Detection Elevation Coverage Profile

The track initiate point is defined as the condition where a tracked target first becomes reportable. The criterion used in the baseline is that a target is in track and has been detected in three of the first four scans. A target is placed into track by a correlation routine that first locates a scan detection that does not correlate with any present or candidate track, and then generates a correlation window for the next two scans. If a subsequent target falls within the window, the two hits are used to initialize a Kalman track. This candidate track will not be reported until the three-out-four crtierion is met, and it will be dropped from track if two consecutive misses occur in the first four scans after initial detection. After the first four scans, target track will be maintained as long as three consecutive missed detections do not occur. This will assure a continued track maintenance probability of greater than 0.95 for over two minutes. Changes in the maintain track criterion can be provided to extend this time interval.

2.3.2 Target Track and Accuracy

Parameter estimation techniques and tracking filter characteristics of the baseline radar are designed to permit acquisition, track, and reporting

25

of heading and velocity on a minimum of 20 targets to an accuracy of 20 degrees in heading and 10 percent in speed. It is anticipated that the adverse arctic environment will require greater accuracy for bird discriminants, larger track files to accommodate non-threat targets, smaller prediction windows to reduce false target correlations in the denser object environment, and greater flexibility to adjust to siting problems. The purpose of the baseline radar is to provide a reference performance level to quantify the degraded performance caused by the adverse environment, and also to define an equipment reference level to establish the incremental implementation penalty of each resource allocation technique. The baseline implementation, performance, and possible growth paths are discussed below.

2.3.2.1 **Parameter Estimation.** Range, bearing, and elevation are estimated and reported to the track filter on each scan of the 4-second volume search. Range is derived from the output of a 32:1 digital pulse compression processor with a compressed pulsewidth of 2 microseconds. The return is sampled twice per pulsewidth to reduce processing losses and therefore produces an output every 150 meters. A "greatest of" logic selects the sample which peaks in both range and doppler filter outputs. Data from three elevation beams which are pulsed simultaneously and processed in parallel are collapsed into a single target report per burst. Four bursts per beam are then collapsed into a single report per beam position. Since the return is independent from burst to burst, because of frequency agility, the range estimate can vary. Range reports from each of the 12 elevation beam/burst combinations are averaged when collapsed into a single report. Details of the beam output data association rules are discussed in the processing algorithm subsection (3.1.3). If only one elevation beam and one burst registers a detection, the range output is a discrete estimate with 150 meters, quantization or approximately 50 meters rms error for large S/N. The baseline simulation was exercised for this input.

Two growth paths for increased accuracy are readily available. One is to implement a pulse splitting estimator; the other is to reduce range resolution. The least incremental cost is associated with an improved range estimator for which the digital ranger could take the form of a second order curve fit to three successive range sample amplitudes. This is implemented simply by taking the weighted sum of 3 amplitudes in a moving window hardware circuit. Resultant errors are approximately 60 meters at maximum range to 15 meters at mid range. The costs of increased resolution are greater, although there are collateral benefits. At a minimum, the wider bandwidth of the narrower pulse requires higher A/D sampling rates, faster clocking of the digital processor which could involve more parallel operation and more chips, a higher PC ratio or more peak power for a shorter pulse, and increased bandwidth requirements and losses through the entire antenna, microwave, and receiver channels. The improved range resolution would however decrease the clutter cell size and improve multiple target resolution, and the higher PC ratio would increase dynamic range. Because of this interrelation, incremental costs for individual resource algorithms must be recomputed when composite sets are selected. Composite performance improvements are similarly related.

26

2.3.2.2 <u>Angle Estimation.</u> Azimuth and elevation data are generated by a logical association of detection reports from adjacent beams. (See subsection 3.2.3.) This method was selected because amplitude comparison information is lost in hard limiting CFAR, and implementation costs of monopulse were not justified for the baseline. When adjacent beams detect a target in the same resolutiuon cell, the target angular position is reported as the peak of the center beam for an odd number of beams or the center beam crossover for an even number of beams. As the target passes through a sequence of 3-degree azimuth beams, it is reported in 1.5-degree quantized steps.

An analysis of the accuracy of this approach was conducted for a simplified simulation of the outputs of three adjacent azimuth beams with four bursts per beam. The target was stepped across the beams from the peak of the center beam to the next crossover. At each target position, the cumulative probability of detection in 4 bursts was computed in each beam for a 0.5-square meter target at 30 nautical miles. From the individual beam reports, the probability of each of 8 possible outcomes of the detection status of 8 beams was computed. The output for each combination is tabulated below.

Beam Detection	Reported Position
1 0 0	- 3°
1 1 0	- 1.5°
0 1 0	0
1 1 1	0
1 0 1	0
0 1 1	+ 1.5°
0 0 1	+ 3°
0 0 0	-----

The error is then computed on the difference between the target location and reported position. The cumulative probability of target detection in one of the three beams is given by the sum of all outcomes having at least one detection. The discrete probability density function $P(\epsilon)$ for each error is given by the probability of the event leading to the error divided by the overall Pd. The rms error is then given by the summation

$$(rms)^2 = \sum_{i=1}^{7} \epsilon_i^2 \ P(\epsilon_i)$$

This function was then integrated over the beamwidth to obtain the rms error for a target position uniformly distributed across the beam cluster.

27
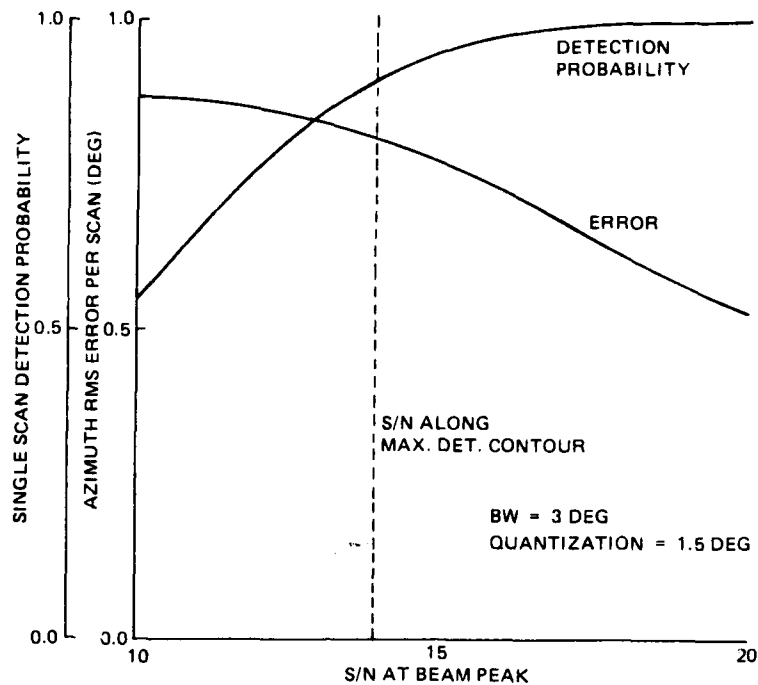
Figure 4. Azimuth Accuracy and Detection Probability Versus S/N

Figure 4 shows the variation of error as a function of S/N at the beam peak. For a target at the maximum range contour of the coverage diagram, the value of 13. 9 dB is the sum of the 2. 7 dB visibility factor of the Blake worksheet, 9 dB of coherent integration gain, and 2. 2 dB of beam shape loss which was included in the visibility factor computation. The error varies from0. 8 degree at maximum range conditions to 0. 5 degree with a 6 dB higher S/N. The improvement of accuracy at high S/N is caused primarily by an increasing frequency of correct decisions when the beam is near crossover.

A target at beam peak has zero mean and variance because it is almost always detected in only one beam and is reported at the correct position. A target at crossover also has a zero mean, but a large variance. It is often reported as alternating from one beam to the other.

2. 3. 2. 3 Target Track. The tracking filter is a five-state extended Kalman where the states are (x,y,z) in position and ($\dot{x}$, $\dot{y}$) in velocity. Its inputs are quantized range and bearing from a scan detection list which is updated on each four-second scan. The algorithm is structured in a track-while-scan (TWS) configuration for multiple targets. Each target is processed by the same set of equations on each scan, with an addressable memory to store all data for that track required for the next iteration. The Kalman filter smooths the scan-to-scan data, predicts the future position of

28

the target on the next scan, and uses data from its covariance matrix to ad-
just the acceptance window size for the next scan to the estimated error in
prediction. When a missed detection occurs, it automatically coasts to the
next scan. Details of the tracking filter are discussed in Section 3.

Figure 5 is an example of a tracking filter performance in the baseline
radar simulation which generates quantized range and angle outputs as de-
scribed above. Additional data are presented in Appendix D. The run corres-
ponds to an offset course where the crossover range is 10 kilometers and the
altitude is 4.5 kilometers. The target therefore enters the search volume
beyond maximum range (120 kilometers) and penetrates along the top of the
coverage volume thus operating at the outer boundary of the coverage profile
for the entire flight. Each point represents a scan period, and the point-
to-point fluctuation is representative of the filter smoothing. The speed
and heading errors are less than the 10 percent and 20 degrees, respectively,
with occasional fluctuation on the order of the specified values. The base-
line radar parameter estimation techniques, tracking filter smoothing, and
specified output errors appear to be a consistent set.
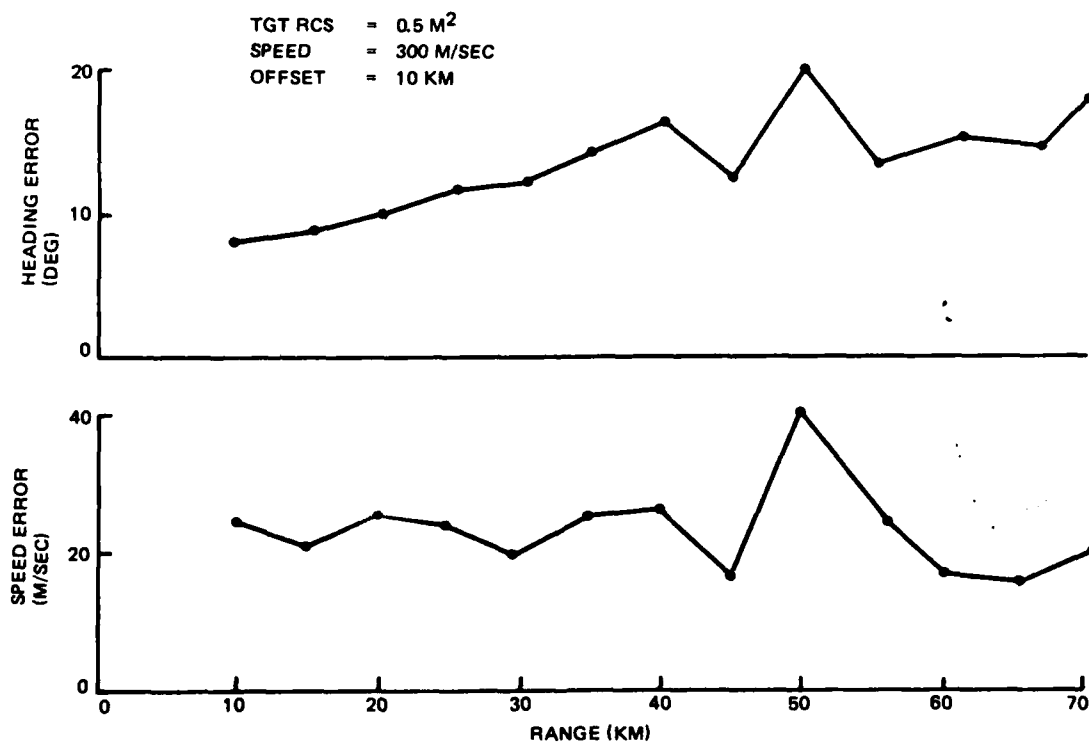
Figure 5. Speed and Heading Error Versus Range

29

Growth paths to improved tracking performance lie primarily in the areas of improved accuracy on the input or higher data rate tracks. The tracking filter itself is capable of much greater accuracy, given better input data. For the managed system, a resource demand generator algorithm will be considered which will evaluate the track via error history or covariance matrix and generate demands for update pulses. The general resource allocation scheduler then can adjust search frame time and update rates to apportion time and energy. Minor modifications in the areas of re-initializing the system for changes in input variance, target maneuver modeling, and window size generation are under consideration. Special purpose discrimination algorithms involving trajectory constraints may also impact on filter design adjustments.

2.3.3 PERFORMANCE IN CLUTTER

The signal-to-clutter performance of the doppler processor in the RRAS baseline radar was evaluated in a clutter environment of terrain, sea, and rain. Details of the clutter analysis are given in Appendix A. The clutter model used in the analysis, and summarized in Appendix B, has been extracted from the EDEW Draft Specification of the SEEK FROST program. The doppler processor evaluated contains eight doppler filters (0 through 7) and utilizes two prf's to move the first blind velocity beyond 400 meters/second as shown in figure 6. Implementation of the doppler processor is discussed in
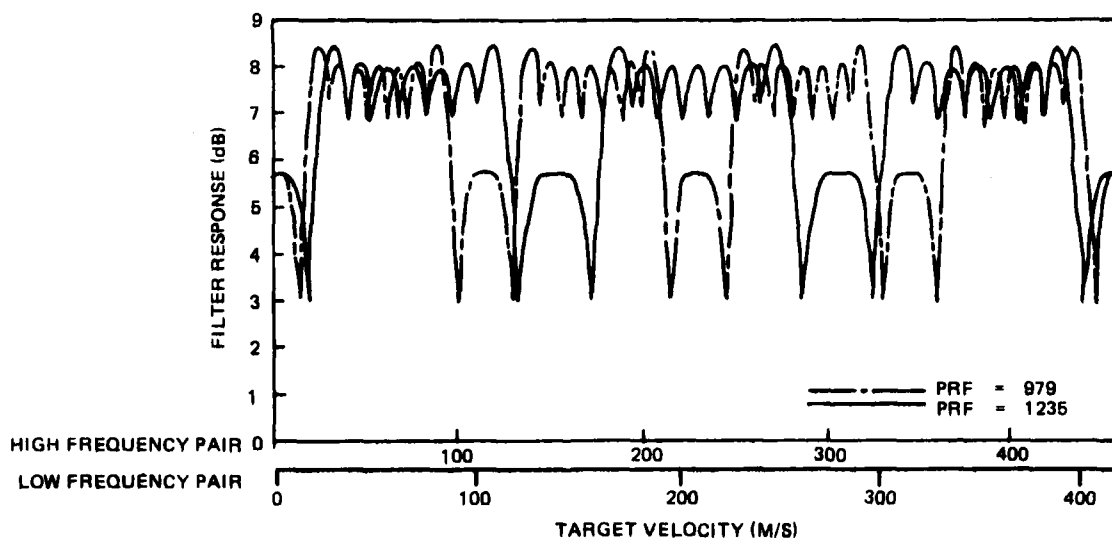
Figure 6. Velocity Response of Doppler Filter

30

Section 4. Filter 0 is included to provide supra-clutter visibility on zero radial velocity targets at crossing trajectories. A threshold map is incorporated in this filter to prevent false reports on clutter from entering the system and to permit detection of any target exceeding the clutter. The threshold map is also discussed in Section 4. Filters 1 to 7 incorporate double cancellation MTI followed by hard limiting CFAR processing to cancel or suppress clutter returns while maintaining a constant false alarm rate. The frequency-prf scheduling is designed to cover the doppler spectrum with overlapping filters such that at least one of the CFAR filters 1 to 7 cover each target velocity.

Ground clutter was included in the baseline radar requirements because a clutter-free radar design would not produce a realistic reference system. Birds and weather extremes, and sea clutter, are assigned to the degraded environment because many of the techniques used to counter them fall in the managed radar category. The baseline radar performance satisfies all the terrain clutter and sea clutter requirements in the central and western DEW Line sites. High altitude sites in the eastern sector, however, will have a reduced detection range for maximum sea states. This high altitude siting problem will be addressed in the managed radar to determine if the reduced visibility zones and possible penetration routes combine to create a vulnerability.

Results of the weather clutter analysis demonstrate that rain clutter is effectively cancelled in the central filters for all range and environmental conditions, but that the edge filters are desensitized for extreme wind velocities. To satisfy the signal-to-clutter improvement factor criterion (SCI), the 99 percentile clutter must be suppressed 6 dB below the noise at a range of 30 nmi. This results in a signal-to-clutter plus noise degradation of 1 dB which is included in the loss budget as a residue loss factor. Filters which do not meet the SCI requirements are gradually desensitized while maintaining a constant false alarm rate (CFAR) via hard limiting and noise leveling. The 0.5-meter^2 target is therefore detected with a lower probability, and the filter retains full visibility for larger targets or the 0.5-meter^2 target at shorter ranges.

Mean rain velocities of 25 meters per second are so high that the peak of the velocity spectrum is actually shifted into the main lobes of filters 1 and 2. Under this condition, there is no effective method of clutter suppression other than a very costly reduction in the range and angle resolution cell of the system. A more cost-effective approach is to detect targets on an intra-clutter basis using the doppler resolution of the filter bank. The doppler filter response isolates the clutter to one or two filters while maintaining visibility at other doppler frequencies. The relative position of the target response in the filter bank will shift because of changes in prf, RF frequency, or a change in radial velocity component as the aircraft penetrates in range. A target can therefore be detected because of the frequency and prf random diversity.

In the TWS mode of the baseline system, however, a target passing through a desensitized filter will be dropped if it fails the target maintenance test and can later be reacquired in the next filter. In the managed radar, the

31

track data can be obtained by scheduling a dedicated update at the proper prf and frequency. The smoothed track data provides the necessary trajectory data to compute the location of a clear filter. A dedicated track update is not required for those cases where proper selection of the search frequency is adequate to insure detection, and where there are not two conflicting targets in that beam. Additional signal processor flexibility and dwell time resources are required to implement this algorithm.

Some of the quantative results of the clutter analysis in Appendix A are summarized below for terrain, sea, and weather.

The terrain distributed clutter is defined by a Weibull probability density function. For a 99-percentile probability, a range of 30 nmi, and the Weibull parameters given by the SEEK FROST clutter model (Appendix B), the clutter RCS is 32.4, 123.0, and 631.0 meters^2, respectively, for tundra, moderate hills/mountains, and severe hills/mountains. The power spectral density for the terrain clutter is defined by an impulse function at zero doppler, plus a symmetric, continuous polynomial function. Based on this spectrum, the signal-to-cluter improvement factor of each doppler filter (except the zero filter) is more than adequate to allow detection of a 0.5-meter^2 target with 2.7 dB single pulse visibility factor (an 11.7 dB integrated signal-to-interference ratio) for each system prf burst. For doppler filters 1 through 7, approximately 49.5 dB of signal-to-clutter improvement is required. This is provided by a theoretical SCI of > 90 dB which is limited to 60 dB by system instabilities.

Distributed sea clutter is also characterized by a Weibull amplitude function. For eastern sector sites at maximum altitude, a 99-percentile design value, a 30-nmi range, a median value of -45.4 dB, and a shape parameter of 1.472, the clutter RCS is 236.2 meters^2. The sea clutter spectrum is defined by a Gaussian function with a 3 dB width of 2.5 meters/ second, and a mean velocity varying between -2.5 and +2.5 meters/second. All of the non-zero doppler filters, except 1 and 7, satisfy the required improvement factor to detect a 0.5-meter^2 target for all mean clutter velocities. Doppler filter 1 (7) does not have the required improvement factor over a small range of positive (negative) mean velocities. For central and western sector sites which have a smaller maximum altitude, the clutter RCS is reduced to 13.6 meters^2, and all of the doppler filters exceed the signal-to-clutter improvement factor requirements.

The weather clutter model is defined separately for both Labrador and Arctic Circle sites, and consists of cellular, uniform, and bright band rainfall. In Labrador, the precipitation extends to 10,000 feet, the maximum rainfall rate is 10 millimeters/hour (cellular), and the clutter cross section is 0.90-meter^2 at 30 nmi. In the arctic, the precipitation extends to 6000 feet, the cellular rate is 6 millimeters/hour, and the clutter RCS is 0.24 meter^2 at 30 nmi. The clutter spectrum is a Gaussian density function with a mean velocity having any value between ±25 meters/second. The standard deviation (at 30 nmi) is 5.2 and 3.3 meters/second, respectively,

32

for Labrador and the Arctic Circle. For this worst-case set of conditions, portions of filters 1, 2, and 3 do not satisfy the required improvement factors in Labrador and the Arctic Circle for all values of mean velocity. This is based on a 0.5-meter^2 target. When less intense rainfall rates of 2 and 1 millimeter/hour are used (uniform precipitation model), the clutter RCS is reduced by approximately 12 dB. This results in a substantial increase in the range of clutter mean velocities for which the filter responses satisfy the signal-to-clutter improvement factor requirements. In fact, for Labrador sites, only filters 1 and 2 and, for the arctic, only filter 1, do not satisfy the required SCI for all mean velocities of the clutter. Details of the clutter performance are given in Appendix A.

Section 3

RADAR ALGORITHMS

The first part of this section contains descriptions of algorithms included in the baseline radar system to permit adequate performance as a track-while-scan system in a minimally adverse environment. The algorithms provide adaptive decision making logic from α search through track-while-scan to target parameter estimating and reporting. A description of the algorithms and the rationale for their selection is included.

The second part of this section includes a description of additional algorithms (not in itself complete) which are considered candidates in optimizing radar performance in adverse arctic environment.

3.1 BASELINE RADAR ALGORITHMS

3.1.1 Search Algorithms

The baseline system search is a straightforward, constant rate scan with azimuth beams stepped around at the rate of 30 per second resulting in a 4-second data rate. Four bursts of 9 pulses each are transmitted for each beam position, with the burst prf varied between bursts to eliminate velocity holes caused by clutter desensitizing the zero doppler filter. Burst-to-burst frequency agility is provided to decorrelate target fluctuation between bursts, thereby improving detection probability.

3.1.2 Detection Algorithm

The signal processor provides coherent integration and doppler filtering on signals from 8 of the 9 pulses of the burst, the 9th pulse allowing clutter cancellation of second-time-around returns. Signals are independently thresholded for each burst, and detection reports containing range, doppler, signal amplitude, and elevation beam are transferred to the data processor. Further detection processing is performed in the data processor.

3.1.3 Detection Processing Algorithm

Detection processing in the data processor includes associating and consolidating all the adjacent beam and multi-burst detections caused by a single target into a single report. The processing will estimate range, elevation, azimuth, and doppler, and will resolve range and doppler ambiguities where possible. These reports are stored in a scan detection list for use in the subsequent target track and track initiation procedures. The primary discriminant for associating detections is range, with doppler frequency playing a secondary role. A tolerance of ± 1 range sample (1/2 pulsewidth or 150 meters) is used for range correlation, and ± 1 filter used for doppler. If a non-limiting CFAR is used in the signal processor,

35

elevation becomes available as a discriminant for the consolidation of burst detections (from a single burst) into beam detections (due to the total of four bursts).

Range ambiguities of targets detected with more than one burst in a beam position are resolved. Detections which correlate in ambiguous range are first time around, and marked as ambiguity resolved. If no correlation is found, then the 2nd and 3th time around ambiguous ranges are checked. If correlated, then the unambiguous range is calculated, and the ambiguity is marked as resolved. The doppler ambiguity is similarly resolved to the extent possible. With the limiting CFAR, doppler interpolation is not feasible, and the accuracy is insufficient to allow high confidence ambiguity resolution for targets of all speeds. Detection on two different bursts is sufficient for resolving the doppler ambiguity when doppler interpolation is used. The range and doppler ambiguity status is tagged, and if not resolved on one beam position, it may be resolved in adjacent beam positions or subsequent scans.

Range estimate is the mean of the range from each of the detections associated with the target adjusted as required for the range ambiguity. Similarly, doppler velocity estimate is the mean of the doppler of each of the detections adjusted for ambiguity. Elevation estimate for the non-limiting signal processor is a weighted mean of the elevation estimates from each burst. With the limiting CFAR, the signal amplitude limits approximately 4 db above the threshold level. The high probability of limit makes estimating the target angular position more difficult. Estimation of target elevation is therefore postponed until data from all of the detections associated with the target are accumulated.

The procedure used to estimate elevation with limiting CFAR is as follows: The elevation estimate is quantized to one of five values - the angles of the three beam peaks, and the two crossover angles. The selection of any one of the five values is based on the following tests, after all bursts associated with the target have been received. The sequence of tests is applied in the order shown. As soon as a test is satisfied, the procedure is stopped and selection is made.

Test 1: On the same burst, detection takes place in both of two adjacent elevation beams, neither of which is at the amplitude limit level.

- Assign the elevation of the crossover between the two beams.

Test 2: On the same burst, a detection occurs in only one beam. (No restriction on limiting.)

- Assign the elevation of the peak of the beam of the detection.

36

Test 3: On the same burst, detections take place on two adjacent elevation beams. (No restriction on limiting.)

- Assign the elevation of the crossover between two beams.

Test 4: On the burst, detections take place on the low and high elevation beams. (No restriction on limiting.)

- Assign the elevation of the peak of the low beam.

Test 5: On the same beam, detections take place on all three elevation beams. (No restriction on limiting.)

- Assign the elevation of the low beam to mid-beam crossovers to the detection.

Several different azimuth estimation algorithms have been considered. The simplest, selected for the baseline with limiting, is to take the midpoint of azimuth interval over which continuous (adjacent beam) detections from the target are obtained. With a continuous step scan, this is implemented by taking the azimuth of the beam for which the target is first detected, and then incrementing the azimuth by 1/2 the beam step for each subsequent beam position in which the target is detected. For non-limiting signals, comparative levels are used to select beam peak or crossover. Alternate algorithms include sequential beam lobing and azimuth monopulse.

3.1.4 STC Algorithm

Sensitivity time control (STC) is applied to each of the elevation beams. The STC serves to increase the effective dynamic range of the system, reducing the probability of receiver and signal processor saturation on close-in clutter, and on targets prior to the initial MTI processing. It also serves to desensitize the small radar cross section targets close-in, minimizing the number of short range bird detections. Examination of the probability density function of birds and bird flocks shows that the number of detections increases greatly as the system sensitivity is increased below 1 square meter.

The STC applied in the baseline system is as follows: For the low beam, sensitivity increases as the range cubed between minimum range (5 nmi) and 20 nmi, with maximum sensitivity at and beyond 20 nmi. For the mid-beam, sensitivity increases as range cubed from minimum range to 9 nmi, and is proportional to range between 9 and 20 nmi, with maximum sensitivity at and beyond 20 nmi. The high beam STC is proportional to range between minimum range and 8.4 nmi.

STC has an effect on the coverage diagram. The elevation coverage diagram (figure 3) includes the effects of STC. The primary effects are to reduce the effective sidelobes for the low and mid-beams, and to pull down the higher elevation coverage of parts of the mid and high beams to the 15,000-foot altitude line.

37

Care must be taken during the implementation of the STC to account for possible interaction with constant false alarm (CFAR) circuits. For example, introducing a programmed reduction in receiver gain reduces receiver noise as well as signal level, when inserted after the low noise amplifier. A threshold map CFAR sets the detection threshold relative to the noise level, thus negating the effect of the gain reduction. This can be overcome by setting a floor below which the threshold is not allowed to drop; the floor being set to the threshold produced by full sensitivity noise. (The noise false alarm rate is lowered in the reduced sensitivity region.) One way to avoid this interaction is to place the STC attenuation ahead of the low noise amplifier so that CFAR always has the noise to limit the sensitivity.

3.1.5 Initiate Track Algorithm

The RRAS baseline radar track initiate requirements were defined to achieve a probability of track initiate of 0.95 within 16 seconds of penetration by the target into the radar volume. For the baseline radar, an m out of n algorithm was chosen where $m/n = 3/4$. This means that three detections out of the first four initial scans are required to place a target in a reportable status. This criterion achieves the required 95 percent track initiate probability.

The track initiate process is started by associating two residual scan detections - one a detection from the Nth scan and the other from the N-1 or N-2 scan. A residual detection is a detection that cannot be identified with an existing track. The basic requirement is that the locations be separated in space by a distance no greater than the maximum speed (400 meters/second) multiplied by the elapsed time between the detections, plus allowances for location estimate errors of the two detections. If reliable estimates of elevation and/or doppler velocity are available, then these dimensions will be included in the acquisition window with suitable allowances for target maneuver and estimate errors. (Target maneuver capabilities limit the usefulness of doppler for moderate or low speed targets with time between detections greater than approximately 4 seconds.)

3.1.6 Maintain/Drop Track Algorithm

A trade-off study was performed to select the track maintenance algorithm for the baseline radar. Two candidate algorithms were investigated:

o drop track for two consecutive missed detections

o drop track for three consecutive missed detections.

The following recursive formulas were generated for each criterion. (The derivation of these expressions appears in Appendix C).

Define   PMT(n)   = the probability of maintaining track on
                     the nth scan

          PMT(n+1) = the probability of maintaining track on
                     the $(n+1)^{st}$ scan

38

$$PMT(n+2) = \text{the probability of maintaining track on the } (n+2)^{nd} \text{ scan}$$

$$Pd = \text{the probability of detection per scan}$$

and $\quad Q \quad = 1 - Pd$

For two consecutive misses,

$$PMT(n+2) = Pd [PMT(n+1) + QPMT(n)]$$

where $\quad PMT(1) = PMT(2) = 1$

For three consecutive missed detections,

$$PMT(n+3) = Pd [PMT(n+2) + QPMT(n+1) + Q^2PMT(n)]$$

where $\quad PMT(1) = PMT(2) = PMT(3) = 1.$

Figure 7 is a plot of the track maintenance probability PMT for two consecutive missed detections as a function of the number of scans and the scan detection probability Pd. The graph is for a tangentially moving target so that Pd remains constant from scan to scan. The RRAS requirements specify a track initiate probability of 0.95. As can be seen, for a 90 percent scan detection probability, the 95 percent cumulative track maintenance probability will be crossed at the end of 8 scans. This was judged to be unsatisfactory. Therefore, the three consecutive missed detection algorithm was plotted similarly and is shown as figure 8. For the same 90 percent scan probability of detection, the 95 percent cumulative track probability is maintained out to 60 scans.

As a result, a combined algorithm was selected which employed the two consecutive miss criterion for N scans, with a switchover at the $(N+1)^{st}$ scan to three consecutive misses. This is demonstrated in figure 9. The curve is for a 90 percent detection probability per scan and a tangential target. Selecting a switchover at N = 4, which gives a cumulative track maintenance probability of 0.95 for 41 scans, the maintain/drop track algorithm can be stated as follows:

o For the first 4 scans after the initial detection, any target placed in a track file will be maintained in that file as long as two consecutive missed detections do not occur. If two consecutive misses occur, the target will be dropped and removed from the file.

o From the 5th scan on, any target already in a track file will be maintained in that file as long as three consecutive missed detections do not occur. If three consecutive misses occur, the target will be terminated and the target removed from the track file.
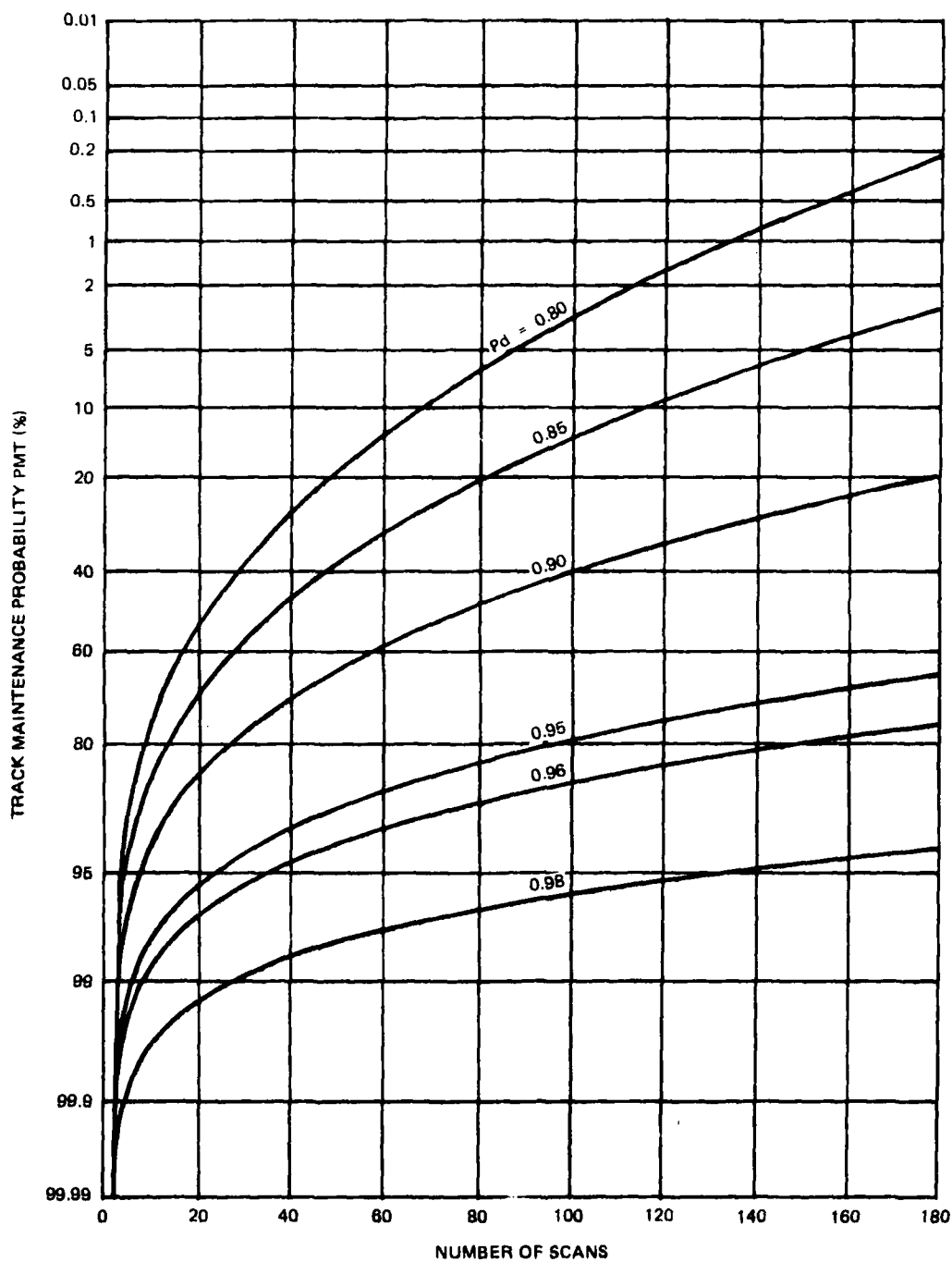
Figure 7. Probability of Track Maintenance Versus Number of Scans
as Function of Per Scan Pd for Two Consecutive Misses
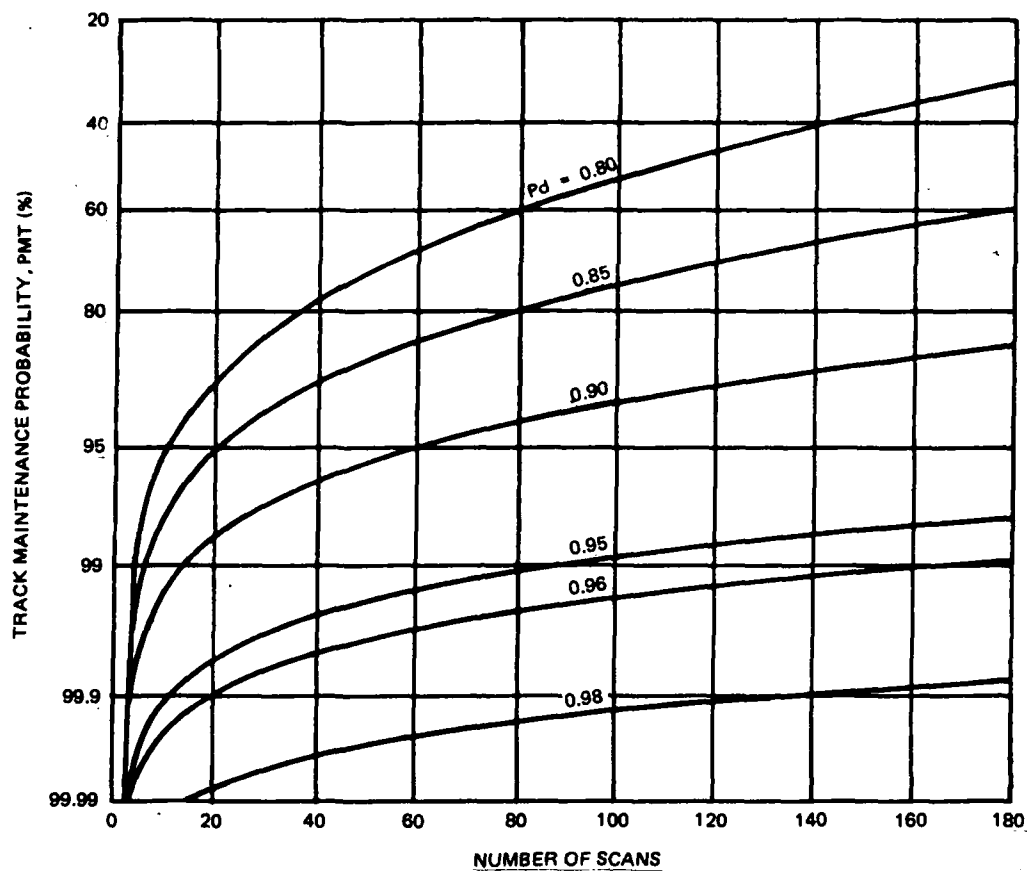
Figure 8. Probability of Track Maintenance Versus Number of Scans as Function of Per Scan Pd for Three Consecutive Misses
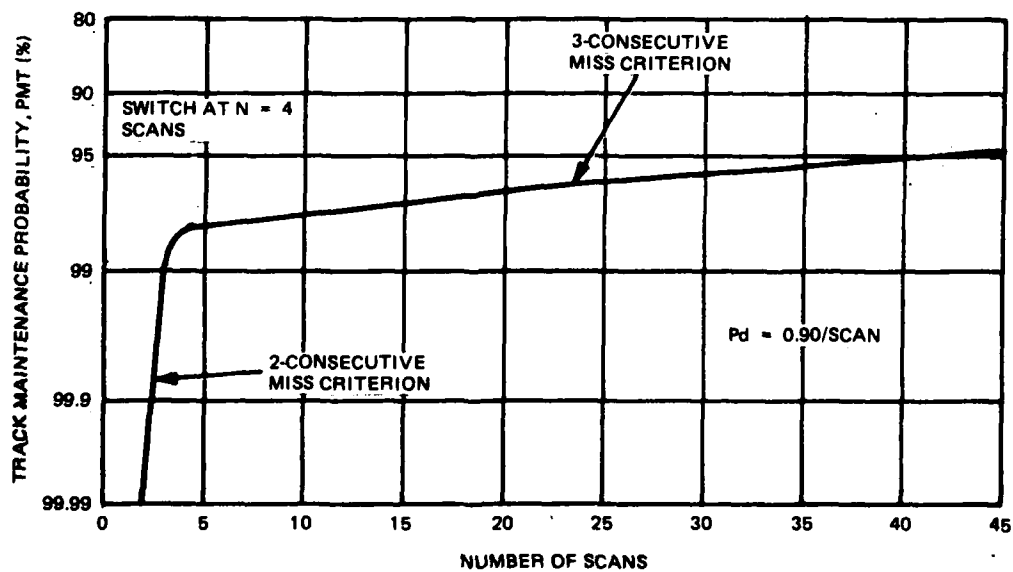
Figure 9. Probability of Track Maintenance Versus Number of Scans for 90 Percent Scan Pd with Switch from Two to Three Consecutive Misses

41

3.1.7 Tracking, Smoothing, and Prediction Algorithm

The purpose of the RRAS tracking, smoothing, and prediction algorithm is (1) to transform the available "noisy" radar measurements of present target position to accurate target position/ velocity/heading and (2) to provide predicted target position (and track window tolerances) on the next scan. The latter function is generally used to associate tracks in a multi-target/ clutter environment.

A variety of filter algorithms has been used in radar track-while-scan systems. These include polynomial, Kalman-related, and other types of filters. The (α, β) and (α, β, γ) are the primary examples of polynomial filters. There are a number of variants, including configurations with time-varying (rather than constant) parameters, "yoked" (rather than independent channels), and those providing specific weighting of past data (e.g., fixed memory and exponential weighting). Linear, quasi-linear, and non-linear Kalman-related algorithms have also been used. There are a large number of variations, depending on the coordinate systems chosen to represent plant dynamics and the measurements, methods for weighting past data, multi-stage iterations for measurement updates, and adaptive configurations.

The optimal performance characteristics of the Kalman filter make it a prime candidate in many estimation/prediction applications, and the use of re-lated algorithms in track-while-scan systems has been discussed frequently in the literature. The algorithm selected to perform the tracking, smoothing, and prediction function for the baseline system is a five-state extended Kalman filter. This filter is used to perform the tracking, smoothing, and prediction function. The filter configuration reflects a mathematical model of target motions in which zero mean random accelerations are assumed to cause perturbations from a straight line trajectory.

The five states are designated $[R_X, V_X, R_Y, V_Y, R_Z]$ where R_X, R_Y, R_Z represent, respectively, the easterly, northerly, and vertical position of the target relative to the radar, and V_X, V_Y represent, respectively, the E/W, N/S velocity of the target. The filter uses available radar range, bearing, and elevation measurements to generate optimal real-time estimates of target position, velocity, and heading. The predicted position of the target on the next scan, i.e., the track window center, is also computed.

Fortran simulation programs have been generated to facilitate studies of filter performance in response to various target trajectories and radar measurement errors. The computer runs conducted to date have used constant velocity targets "in the clear", and quantized radar measurements. Several variations in filter structure and parameter values have been investigated. Current studies are focused on a filter structure in which target acceler-ations are modeled in a target track-oriented coordinate system. Advantages have been demonstrated over structures based on modeling independent random accelerations in the X, Y axes.

42

The use of a Kalman filter appears well suited to the track-while-scan application, and it has been widely used in such systems. Features include the generation of the track window center and of track window tolerances (using covariance matrix data), automatic provision for "missed looks" (coast mode), and flexibility/growth to probabilistic weighting schemes for uncertain observations (clutter), multi-target tracking, and adaptive configurations. The use of modern algorithms (such as square root, etc.) minimize the computational burden. The structure of the filter is described in Appendix D.

3.1.8 Discrimination Algorithm

The major effort expended on discrimination to date has been with the respect of the overload characteristics of the baseline system. The targets of interest are air-breathing aircraft, with an effective cross section of 0.5 square meter or greater, having speeds over 80 knots, within the defined coverage out to 30 nmi in range and up to 15,000 feet in altitude. Objects for which responses are not desired include ground clutter, large discrete fixed targets and icebergs, sea clutter, weather clutter, aurora and atmospheric anomalies, and angel clutter (i.e., birds, bird flocks, and insects), both distributed and discrete (dot angels). Clutter considerations are major factors driving the design configuration and parameters of the radar. Examples of these include selection of the smallest resolution cell size consistent with cost limits, the use of pulse doppler processing with its multi-pulse burst, the inclusion of the threshold clutter map, other CFAR techniques and STC, and other cross section discriminants. Discrete point clutter can be eliminated by use of a point clutter table. All detections occurring at point clutter resolution cells are deleted from processing, but are used to update the table. The same function is performed by the censor map described under the candidate algorithms.

Distributed angels will be handled by the CFAR, particularly the threshold map. Also, both distributed and dot angels tend to concentrate at the lower altitudes, and must therefore compete with surface clutter, particularly in the lower beam. Altitude as a discriminant is limited by the fact that bird flocks and individual large birds are occasionally found at altitudes up to 20,000 feet or more. However, it may be useful at particular sites and times. The primary form of clutter not fully handled in the baseline by these techniques is dot angels (primarily bird flocks). In the baseline system, the discriminant against the residual dot angels is speed. They will be placed and retained in a form of non-reportable track to avoid the processing burden of initiate track during reacquisition.

3.1.9 Overload Algorithms

Overload is a major consideration in the design of any fully automatic radar, particularly one which is unattended. The information handling capacity and overload response should be considered from the signal processor through to the output communications of the system. In general, when overload does occur, the degradation should be graceful with preference given (where possible) to the highest priority targets.

Within the signal processor, overload can take place in the output data buffers prior to transfer to the data processor. The signal processor incorporates a local peak detector in range/doppler detection rule. With two range samples per compressed pulsewidth and 8 doppler filters, the maximum possible number of detections is four per pulsewidth for each elevation beam.

The tentatively selected detection reporting capacity is 30 detections for the low beam, 20 for the mid-beam, and 10 for the high beam. Taking into account the instrumented range for each beam, the detection reporting capacity (as a percent of the maximum possible number of detections) is 2.2 percent for the low beam, 3.7 percent for the mid-beam, and 4.2 percent for the high beam. The detection density can be expected to be greater at the closer-in ranges due to less masking of earth curvature, and greater cross section sensitivity; hence, the greater percent capacity for the mid and high beams.

The signal processor overload rules are subject to change when the additional optimizing resource allocation algorithms are introduced. For the baseline, however, only one detection is allowed per range sample, with preference given to the detection closest to the middle filter. When a buffer is full, detections are discarded in the order of minimum range detection up to 10 nmi, then, maximum range detections. The rationale is that the region between 10 to 30 nmi is expected to be the most important, and this rule is readily implemented in the signal processor hardware.

Details of the algorithms used to process the detection data in the data processor are dependent on whether limiting CFAR is used in the signal processor. The following discussion on overload in the detection data processing is based primarily on the algorithms for the limiting CFAR used in the baseline radar. The basic approach and target handling capacity are similar for a non-limiting CFAR configuration, although the order of operations is revised and less buffer is required.

The detection data processing for the baseline system includes a set of four data buffers. These are an input data buffer holding the detection data for the last three beam positions plus the current beam position, a burst detection list buffer, a beam detection list buffer, and a scan detection list buffer. All of these buffers, except the scan detection list, contain data from the last three beam positions plus partial data from the current beam position. The scan detection list contains current scan detection reports plus detections not associated with current tracks nor formed into new tracks for the two previous scans.

The input detection data buffer has sufficient capacity to hold all of the data received from the signal processor. The burst detection list has a capacity of 40 detections per burst, the maximum input data detections from the three beams being 60. Overload, however, is improbable since each of a number of targets are expected to be detected on more than one beam. In view of the improbability of buffer overload, priority is simply given to the closest (unambiguous) range detections.

44

The beam detection list has a capacity of 50 detections per beam position. Overload can take place at this level, but is not probable since many targets will normally be detected on more than one burst. As with the burst detection list, priority is given first to the closest range detections beyond 10 nmi (unambiguous if resolved).

The sizing of the buffers for the scan detection lists is dependent on the track initiate algorithms as well as the expected target density. Using the baseline system algorithm of initiating a provisional track, the number of residual N scan detections on the scan detection list (i.e., targets detected on the Nth scan not already in track) is a little over twice the number of targets first appearing within the coverage during the scan period plus the false alarms per scan. This results essentially from the fact that a new target must be detected at least twice to initiate a track. Similarly, the number of items remaining on the scan detection list from the N-1 scan can be shown to be approximately equal to the number of new targets appearing within the coverage during the scan. The number of items remaining on the scan detection list from the N-2 scan is a little over 10 percent of the new targets first appearing within the coverage, with a detection probability of 0.9 per scan.

The scan detection lists are not static over a scan period. Items are added to the list as detections take place, and are removed when associated with an existing track or formed into new tracks. The track acquisition and maintenance windows extend over 11 beam positions, at most, and normally much less. Correlation of detections can therefore start within 1/10 scan period (0.4 second) after detection and can normally be expected to be completed within 1/4 scan (1 second). Similarly, associating current scan detections with previous scan detections can start when correlation with existing tracks is complete or, typically, 1/4 scan after detections are received from an azimuth beam position. The scan detection list buffer size should therefore be equal to about 1/4 to 1/2 the maximum number of tracks plus about 3 times the maximum number of targets entering the surveillance volume (new targets) per scan (i.e., the number of targets plus number of N-1 and N-2 residual detections on the scan detection list). The number of new targets/scan should also include tracks which were dropped or rejected, but which are still in the coverage area.

In the case of buffer overload, detections are discarded in the following order: detections greater than 60 nmi (i.e., multiple time around targets), residual detections greater than 35 nmi, residual detections greater than 30 nmi, and then detections within a predesignated sector(s) of increasing width.

3.1.10 Coast Mode

A coast capability is built into the track algorithms to allow for missed detections. The possibility of including a special coast mode was considered and discarded for the baseline track-while-scan radar. The rationale is that there are two situations where coast is considered - when target tracks cross and when a target passes through a high clutter region, particularly zero doppler.

45

The prediction of a crossing track conflict takes considerable data processing, particularly with a large number of tracks. Unless dedicated track bursts are scheduled, it serves little purpose. With the baseline system, the detections from crossing tracks are processed normally. When a detection falls within more than one track maintenance window and/or more than one detection falls within the same track maintenance window, then the detections are assigned to tracks on the basis of discriminants such as correspondence of range rate to doppler and elevation where possible, or on the basis for relative closeness to the predicted location. A one-to-one correspondence of detection is forced, i.e., one and only one detection is assigned to a track if one or more detections fall within a range-angle-doppler track window, and a detection is assigned to only one track.

For the case of a tangential crossing, where the target is approaching the zero doppler filter, there is an increasingly high probability that the target will not be visible because of clutter. The threshold and clutter maps are presumed to handle the problem of false detections along with algorithms used to associate detections with tracks. The question to be considered is the extent to which detection requirements for maintaining track should be modified. The crossover between the doppler filters 0 and 1 occurs at a phase progression per pulse period of 48 degrees. This corresponds to a radial speed of between 13.3 meters/second to 20.4 meters/second, depending on the prf and frequency.

The total time required to traverse the zero doppler filter can be shown to be:

$$T_c = 2 \frac{R_c V_R}{V_T \sqrt{V_T^2 - V_R^2}}$$

where: R_c = crossing range
V_T = target speed
V_R = filter crossover radial speed

For representative targets, the time required to traverse the zero doppler filter varies from 1.8 seconds for a 400-meter/second target crossing at 5 nmi, to 20.2 minutes for a 40-meter/second target crossing at 30 nmi. A target with an acceleration as little as 0.2 g will deviate about 1/2 nmi from its predicted location in 15 seconds. A 200-meter/second target with a 10 percent error in speed estimate, will produce a 1/6 nmi error in predicted location in 15 seconds. Fifteen seconds is, therefore, about the longest reasonable time without a detection. The present maintain track criterion allows for 3 consecutive missed detections before dropping track (or 12 seconds without a detection).

3.1.11 Track-While-Scan Maintenance Window

Sizing the track maintenance window includes allowances for detection location estimate errors, predicted location errors, and target maneuver.

46

The allowance for detection location estimate errors is $\pm$150 meters in range (1/2 range resolution), and $\pm$1.5 degrees in azimuth (1/2 beamwidth), which is equivalent to that used for the acquisition window.

The predicted location error allowance is derived from the tracking covariance matrix after the target has been in track a sufficient time for the distribution to settle; e.g., $W_{\gamma\rho} = \epsilon_x + \epsilon_{\dot{x}}\Delta t$, etc., where the ϵ's are the component errors to the desired confidence level (2 or 3σ).

Target capabilities of up to $\pm$3 g turns and $\pm$1/2 g linear acceleration within the speed limits of 40 to 400 meters/second were considered in establishing a maneuver allowance for the window size. Looking first at the effect of 3 g turns, the envelope of possible target positions at the end of an 8-second interval relative to a straight line predicted position is shown in figure 10 for several speeds between 40 and 400 meters/second. For given

PREDICTED
LOCATION

400 M/SEC

200 M/SEC

40 M/SEC

100 M/SEC

60 M/SEC

100 M
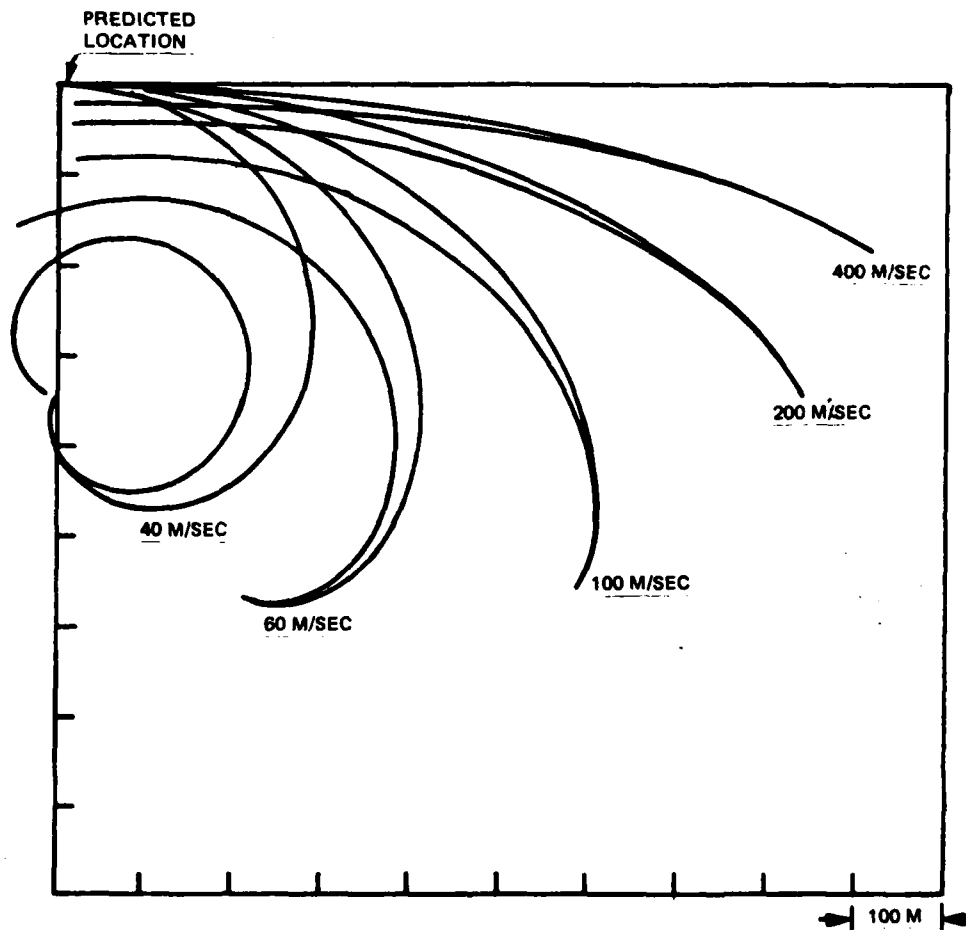
Figure 10. Maneuver Envelopes for Constant Speed Target Executing
Turns Up to 3 g at End of 8 Seconds

47

constant higher speed targets, the envelope is constrained to primarily the cross track direction. Over the continuum of target speeds, the target position at the end of the period will fall within the contour shown in figure 11. Adding an along track acceleration of $\pm1/2$ g, the maximum along-track and cross-track deviations from the predicted position are given in table 6 for several target speeds and time intervals.

In table 7, the data were collapsed, first to eliminate target speed and then to eliminate cross-track/along-track variation, arriving at a single radius maneuver allowance. In case of multiple detections within a window, a more restrictive maneuver allowance can be used since target speed estimate will be available. However, because of the extra computational complexity and burden, it was not adopted for general use in the baseline.

PREDICTED
(STRAIGHT LINE) LOCATION

4 SEC

8 SEC

12 SEC

0.1 KM
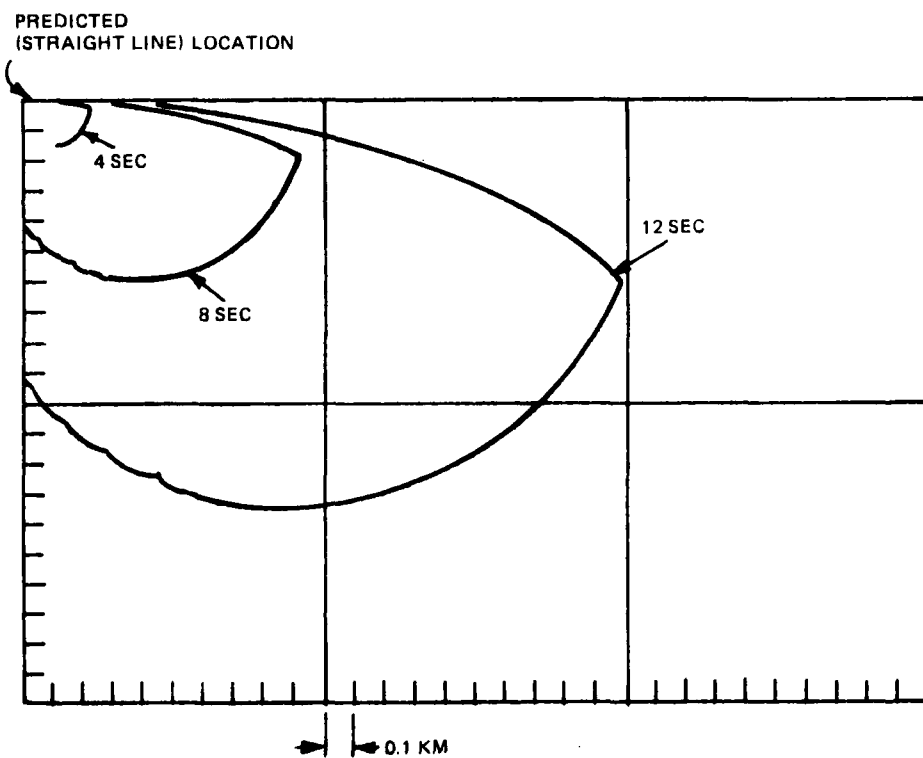
Figure 11.   Maneuver Envelopes for Targets With Speeds of 40 to 400 Meters/Second and Turn Acceleration of 3 g

48

Table 6. Maneuver Deviations from Predicted Position

Speed (m/sec)	1/2 g Linear Along Track	3 g Turn Along Track	3 g Turn Cross Track	Combined Along Track	Combined Cross Track
		4-second maneuver period (meters)			
40	+39	+0	+129	+39	+163
	−0	−149		−150	
100	+40	+0	+208	+39	+225
	−40	−86		−125	
200	+40	−45	+228	+40	+236
	−40	+0		−88	
400	+0	−23	+233	+0	+233
	−40	+0		−70	
		8-second maneuver period (meters)			
40	+156	+0	+289	+156	+441
	−0	−469		−557	
100	+156	+0	+605	+156	+732
	−156	−557		−642	
200	+156	+0	+836	+156	+901
	−156	−342		−498	
400	+0	+0	+912	+0	+912
	−156	−180		−344	
		12-second maneuver period (meters)			
40	+352	+0	+449	+352	+796
	−0	−789		−1073	
100	+352	+0	+1005	+352	+1328
	−352	−1330		−1262	
200	+352	+0	+1622	+352	+1855
	+5	−1061		−1361	
400	+0	+0	+1980	+0	+1980
	−352	−596		−952	

49

Table 7. Maneuver Allowance

Time (seconds)	Along Track (meters)	Cross Track (meters)	Radial Allowance (meters)
2	+10 -20	±60	±60
4	+40 -150	±230	±230
6			±520
8	+155 -640	±910	±900
10			±1400
12	+350 -1360	±1980	±2000
16			±3600
20			±5600
24			±6400

3.2 CANDIDATE ALGORITHMS

Most candidate algorithms can be categorized as a form of adaptive/non-adaptive time-energy-management (TEM), a constant false alarm rate (CFAR) technique, or prioritization. The TEM is essentially transmission selection and scheduling; i.e., RF selection, azimuth and elevation beam positions, rate of scheduling, modes (e.g., search, track), waveform type, and burst energy. The CFAR techniques include the various forms of threshold, censor, and/or point clutter maps. Prioritization include the rules for minimizing performance degradation under system overload. Some of these were included in the baseline algorithms. They may also include such techniques as signature discriminants. One candidate not included in the above categories is the netting or cooperative use of adjacent radars.

The form and specifics the algorithms take are highly dependent on the particulars of the problem being addressed and the context of the radar requirements and basic implementation. The number of possible combinations of techniques for allocating radar resources is very large. Specific examples will be described in the context of known or anticipated problem areas for the baseline radar in an adverse arctic environment. As the study progresses, new problems requiring additional algorithms are expected.

3.2.1 Map Algorithms

3.2.1.1 Threshold Map. A threshold map is included in the baseline radar for the zero doppler channel. Its inclusion allows visibility of crossing targets in regions of light to moderate clutter (depending on target cross section) without causing excessive false alarms. If the limiting CFAR is not used in the other doppler channels, then the map may be expanded to include the other doppler channels. Doppler channels 1 and 7 and probably 2 and 6 would be independently mapped, but channels 3, 4, and 5 would be collapsed to save hardware. Ground clutter is confined to the zero doppler channel; however, weather clutter will extend into one or more of the non-zero channels so that independent thresholding is desirable. The threshold map is also effective against sea clutter, and it will be useful in the presence of distributed bird clutter.

The threshold map is implemented to censor signals in that map cell whenever the clutter exceeds the maximum map level, since no expected target would be visible over that clutter level.

3.2.1.2 Censor Map. The censor map, which is normally implemented in hardware, functions in a different manner than the threshold map. It operates to either pass or censor all signals within the map cell as opposed to reducing sensitivity within the cell. The threshold map is effective against essentially stationary and distributed clutter, while the censor map is used against point clutter moving at speeds below a design cutoff, particularly dot angel type of clutter.

The censor map does cause a loss of visibility, and it is therefore desirable for censoring the least amount consistent with the environmental conditions. The map operation can be made responsive by varying the ease with which censoring can be invoked or dropped with respect to each of the doppler channels included in the censoring.

3.2.1.3 Point Clutter Map. Point clutter which fluctuates may occassionally exceed the threshold level, particularly if it has a long tailed probability density function. If the detections produced are infrequent, it has little effect on the system. If they become more frequent, more resources become tied up. This can be avoided by generating a table of these locations in the data processor. Detections at these locations are then censored prior to processing.

3.2.2 Transmission Selection and Scheduling Algorithms

A large number of possible algorithms exist in the areas of transmission scheduling and time energy management for responsive allocation of radar resources. Consider, for example, search data rate. One limitation on the maximum search rate period is that imposed by the time the target is visible

within the coverage, i.e., allowing a minimum track time after detection to
establish heading, speed, etc., within required accuracy. Such a case is il-
lustrated in figure 12 for the actual siting of two adjacent radars. In this
figure, line-of-sight contours for each of the radars are presented against
targets flying 300 feet above the terrain. The highly probable penetration
corridor is indicated by the cross-hatched flight path where radar visibility
occurs over a 3-kilometer patch. Data rate requirements to meet the 10 per-
cent speed accuracy requirement for a 300-meter/second target are illustrated
in figure 13. For this case, a 0.5-second data rate would be required as
compared to the 4-second TWS rate. The application of flexible beam
scheduling allows increasing the search data rate in such short visible gaps.
Another limitation to the maximum scan period for a track-while-scan
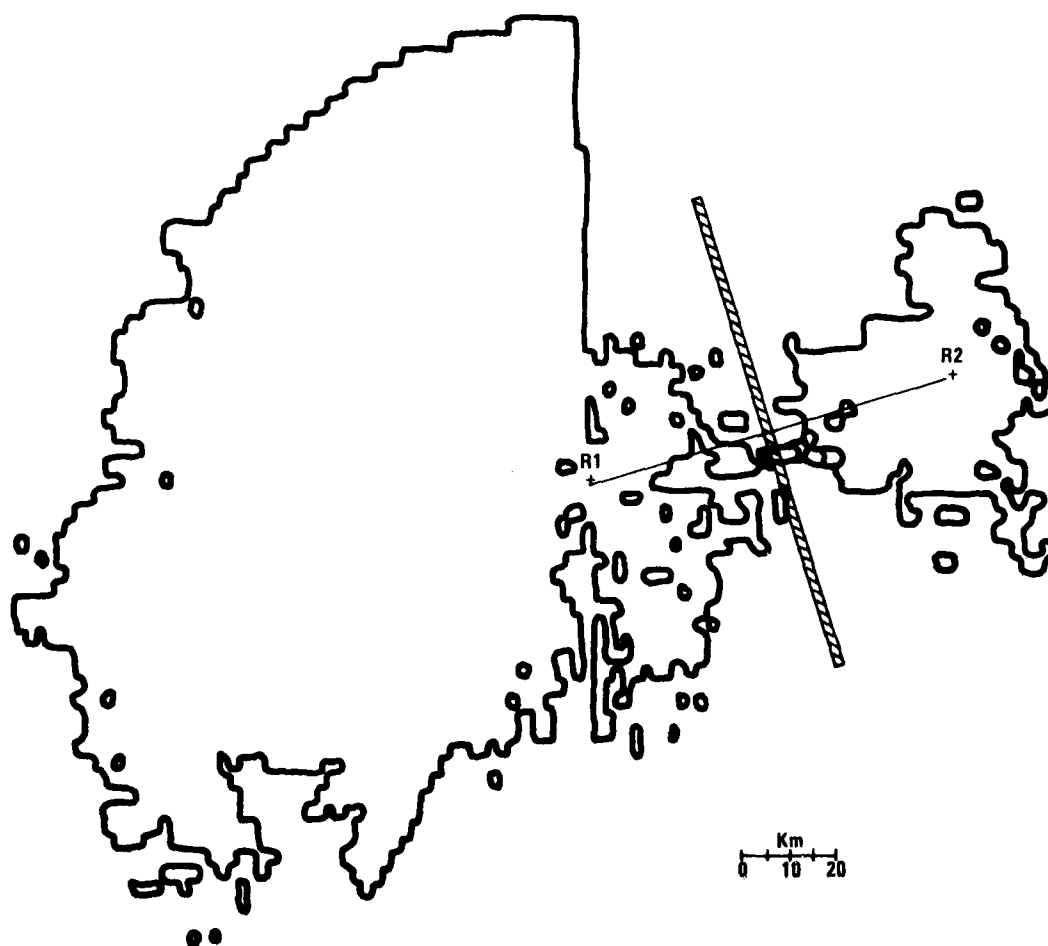
Figure 12. 300-Foot Line-of-Sight Contours for Radars R1 and R2

52

system (or where a search verify is used) is imposed by the increased size of
the acquisition windows, increasing the probability of multiple detections.
Therefore, a higher search data rate which reduces the acquisition window
size could be used for regions with a high density of detections. Similarly
with track, the flexible beam scheduling permits increased track data rates
for either dedicated track transmissions or augmented track-while-scan
transmissions.
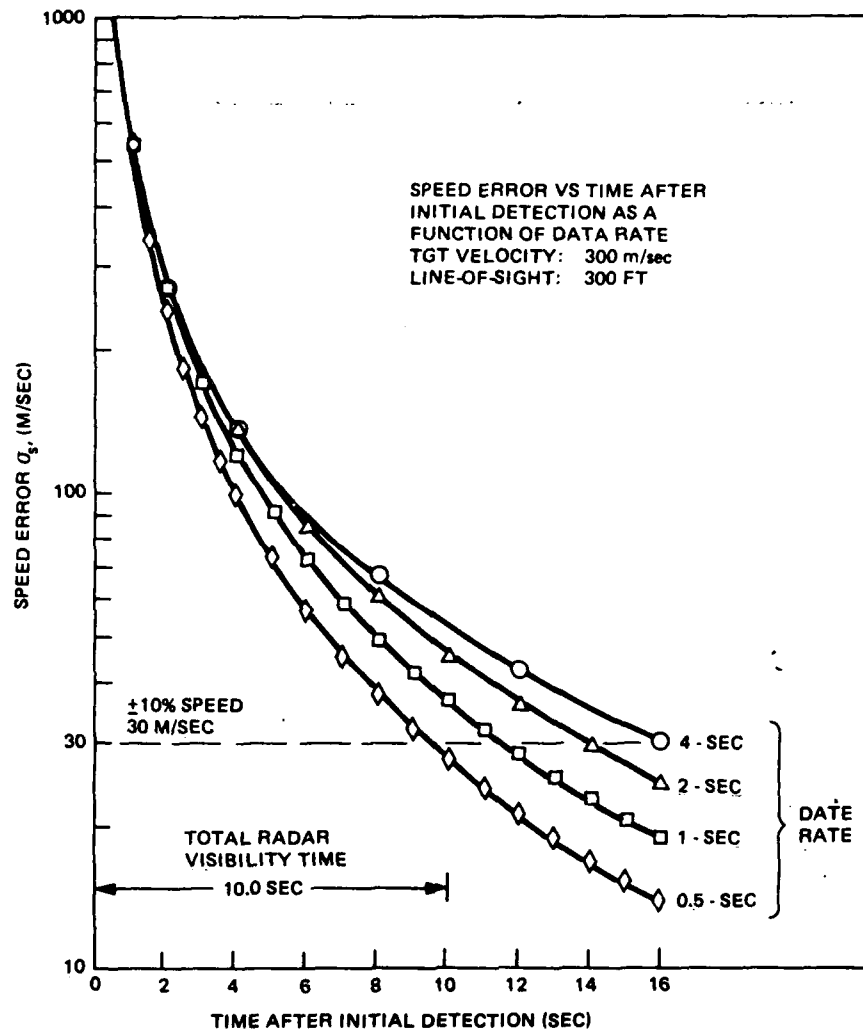
Figure 13. Speed Error Versus Time

Other areas where flexible beam scheduling may allow better allocation of
radar resources include, first, the restricted transmission of high resolu-
tion and multiple pulse waveform to times and regions providing maximum bene-
fits, and, second, the programming of pulse energy to match detection and

accuracy requirements. In the former instance, such transmissions would be applied to reduce ground and/or weather clutter, or for target idendification, avoiding the primary power, reliability penalty, and time penalty (for multiple pulse waveforms) incurred in the signal processing. The programming of pulse energy can be a function of elevation, range, and target amplitude.

Since the need for a higher data rate is greatest at low elevation angles (high bird density and terrain masking), periodic redirecting of the resources normally associated with the upper beams (to provide simultaneous multiple azimuth low elevation beams) is a way of increasing the data rate with minimum impact on the available transmission time.

3.2.3 Cooperative Adjacent Radars

One of the critical coverage areas for surveillance radars is the overlapping region between adjacent radars. This is generally the region where the visible track time is smallest due to zero doppler clutter levels and the minimum penetration path through the radars' coverage volume. Combining detection and track data from the overlapping region between the adjacent radars can materially assist in reducing missed detections, allowing tracks to be maintained when masked to a single radar without the transients, etc., associated with reacquisition.

Section 4

BASELINE RADAR SUBSYSTEMS

This section describes the following Radar Resources Allocation Study (RRAS) baseline radar subsystems:

o   Antenna and beam steering

o   Solid state bottle transmitter/antenna module

o   Frequency synthesizer

o   Digital signal processor

o   Zero doppler filter clutter map threshold

o   Receiver

o   Data processor

o   Power supplies.

4.1   ANTENNA AND BEAM STEERING

4.1.1   Functional Baseline Antenna Description

A cylindrical phased array antenna, using solid state transmit modules in a reliable and low cost configuration, has been selected for the baseline radar. In many respects, this antenna is an ideal configuration for the subject application. The arrangement provides invariant beam characteristics over the entire 360-degree azimuth scan sector, with beam pointing direction independent of frequency and elevation coverage angle. Feed network techniques are capable of low loss azimuthal beam switching while achieving maximum aperture gain with a minimum number of radiating elements. Vertical column network techniques are available for multiple beam pattern synthesis while maintaining low insertion loss, light weight, and low unit cost.

A functional block diagram for the baseline antenna system is shown in figure 14. Basically, the antenna consists of 180 column networks, containing integral dipole radiating elements arranged radially inside a cylindrical radome, with an azimuth distribution/commutation network embodying switches, electronic beam steering phase shifters, and an associated special purpose beam steering computer unit for setting up the three elevation beams.

For transmit operation, the RF energy from the solid state exciter amplifier is split by a 3:1 transmit distribution network to provide a signal for each of the three elevation channels. The lower beam channel contains an azimuth phasing network which comprises an equal 1:45 port power divider and 5-bit collimation phase shifters. Each of the 45 outputs are followed by a solid state transmit amplifier module and a circulator.

55
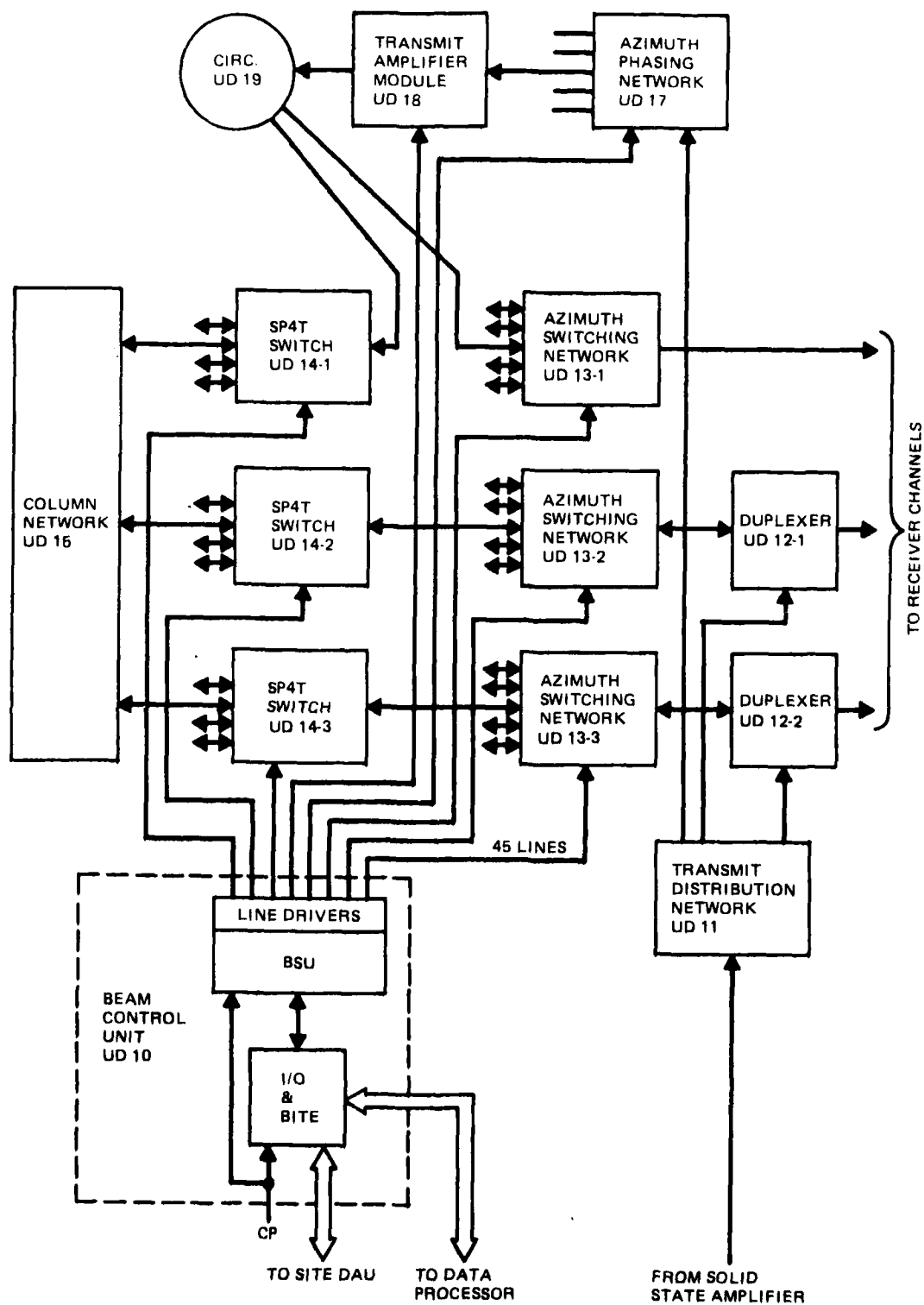
Figure 14. Baseline Antenna, Block Diagram

For the two upper transmit channels, amplifier modules are not utilized, and the output of the transmit distribution network is followed by a duplexer and an azimuth switching network which consists of a 1:45 port amplitude commutator and 5-bit collimation phase shifters. A SP4T commutation switch sequentially places the output distribution for each of the three channels at 45 consecutive column networks to provide the desired azimuthal illumination over a sector of the cylindrical antenna. The ports of the SP4T switches connect to column networks which are separated by 90 degrees in azimuth. The SP4T switches thereby select a portion of the cylindrical array, consisting of 45 column networks over a 90-degree sector, to collimate the 3-degree azimuth beam. Azimuth beam scanning is accomplished, for each channel, through use of the SP4T switches in conjunction with the collimation phase shifters and the amplitude commutator networks. This network switches the active sector around the cylinder in 1.5 column steps to position the beam in 3-degree azimuth increments. For transmit, the signal from each of the three channels is combined in space to produce a fan beam with elevation coverage from 0 to 30 degrees.

The operation of the cylindrical array on receive is similar to that on transmit. The three receive channels from the column networks each contain SP4T sector switches and an azimuth switching network containing phase shifters and an amplitude commutator network. Using the same switching techniques for both transmit and receive provides similar azimuth beam positioning capability.

Table 8 summarizes the key physical features and electrical performance parameters of the selected baseline antenna.

4.1.2 Physical Description

The baseline cylindrical array antenna is shown conceptually in figure 1. An economical, high performance, reliable, electronic scanning antenna is generated by utilization of state-of-the-art subsystems having a minimum number of active components. The antenna consists of a 24-foot diameter cylindrical array with a height of 12 feet, mounted atop a support tower. As was seen in figure 1, the cylindrical array is generated by a circumferential arrangement of the 180 column networks within a protective radome structure. The radome structure provides environmental protection to the enclosed system and serves as the packaging structure for the column networks by controlling the radial and circumferential positions of the networks.

The basic antenna structure is envisioned as a one-piece floor and ceiling with a modularized radome comprising 15 fiberglass sandwich panels, each being 5 feet wide by 12 feet high. The floor structure interfaces with the tower deck and contains false flooring for electrical cables, mounting provisions for the electronic cabinetry, and personnel entry hatches. The floor structure is designed to transmit, directly to the tower structure, all vertical and horizontal loads and moments resulting from equipment weight, and snow, ice, and wind loads. The ceiling structure is sized to withstand the

Table 8. Baseline Antenna Summary

Antenna Type	Cylindrical phased array
Operating Frequency	1215-1400 MHz
Polarization	Vertical
Diameter	24 feet
Height	12 feet
Number of Vertical Columns	180
Number of Elements per Column	24
Number of Transmit Modules	45
Azimuth Beamwidth	3 degrees
Azimuth Scan Coverage	360 degrees
Number of Azimuth Beams	120 at 3° increments
Number of Elevation Beams - Transmit	1 fan beam
- Receive	3 beams
Elevation Coverage	0 to 30 degrees
Elevation Receive Beamwidths	6.75°/8.0°/14.5°
Elevation Beam Peaks	2.5°/11.1°/24.1°
Elevation Beam Directivity (dBi)	32.8/32.1/29.5
Maximum Sidelobe Level	-25 dB

design snow loads for the arctic application. These loads are transmitted to the floor structure by means of vertical structural columns tying the two structures together. The columns effectively unload the radome panels with respect to vertical loads due to snow and ceiling dead weight, resulting in a radome sized to withstand only the design wind and icing loads. Both the floor and ceiling structures are thermally insulated and contain mounting provisions for the radome using circumferential flanges at the 24-foot radome diameter. These structures also contain slide mechanisms to position the 12-foot high column networks which are inserted radially towards the radome surface. The multi-piece radome design affords ease of fabrication, reduced manufacturing costs, and eased transportation requirements as compared to one-piece cylindrical design.

4.1.3 Cylindrical Antenna Performance

4.1.3.1 Pattern Performance.
The pattern performance objectives for the baseline antenna are consistent with the selected cylindrical array configuration. Analysis of the cylindrical array antenna shows that the far-field pattern is separable into azimuth and elevation functions. While the elevation pattern is solely dependent upon elevation angle, the azimuth pattern is dependent upon both azimuth and elevation angles. This effect, which typically produces azimuthal defocussing with elevation angle for a cylindrical array, can be neglected for the baseline antenna which uses three independently collimated elevation beam channels.

The far-field pattern performance of a cylindrical array antenna can be expressed as

$$
\begin{aligned}
E\,(\alpha,\beta) = \sum_{n=1}^{N}\ & A_n(\alpha)G_n(\alpha)\exp(jk_oR_o)\Bigg\{\cos\beta_o\ \sin^2\!\left[\frac{\phi_n-\alpha_o}{2}\right] \\
& - \cos\beta\ \sin^2\!\left[\frac{\phi_n-\alpha}{2}\right]\Bigg\} \\
\times\ & \sum_{m=1}^{M} B_m(\beta)H_m(\beta)\exp[\,jk_oR_o\ Z_m\ (\sin\beta_o - \sin\beta\,)]
\end{aligned}
$$

where α and β are angular directions in azimuth and elevation, A_n and B_m are illumination taper functions, G_n and H_m are array element factors, ϕ_n is the angular location of the nth element, α_o and β_o are the beam peak directions, R_o is the cylindrical array radius, N is the number of elements in a circumferential ring and M is the number of elements in a column, n and m are integer indices, Z_m is the normalized element location, and $k_o = 2\pi/\lambda_o$.

The above expression typically indicates that the far-field pattern for the cylindrical array is separable into a function that varies with the vertical columns and a function that varies with the rings. The azimuth pattern function, however, is dependent upon both the azimuth angle (α) and the elevation angle (β). Calculated azimuth pattern characteristics for the baseline antenna are shown in figure 15 for the lower beam, figure 16 for the mid-beam, and figure 17 for the upper beam. Pattern cuts are shown through the collimated beam peak and for elevation angles, corresponding to 3-dB levels, above and below the beam peak.

The pattern data indicate no significant amount of defocussing for either the low or the center beam. For the high beam, the worst case azimuth beamwidth due to defocussing is less than 3.6 degrees, and shouldering occurs below -18 dB. For the high beam only, the small amount of azimuth defocussing is considered acceptable for the baseline antenna, and no special techniques are recommended for collimation correction.
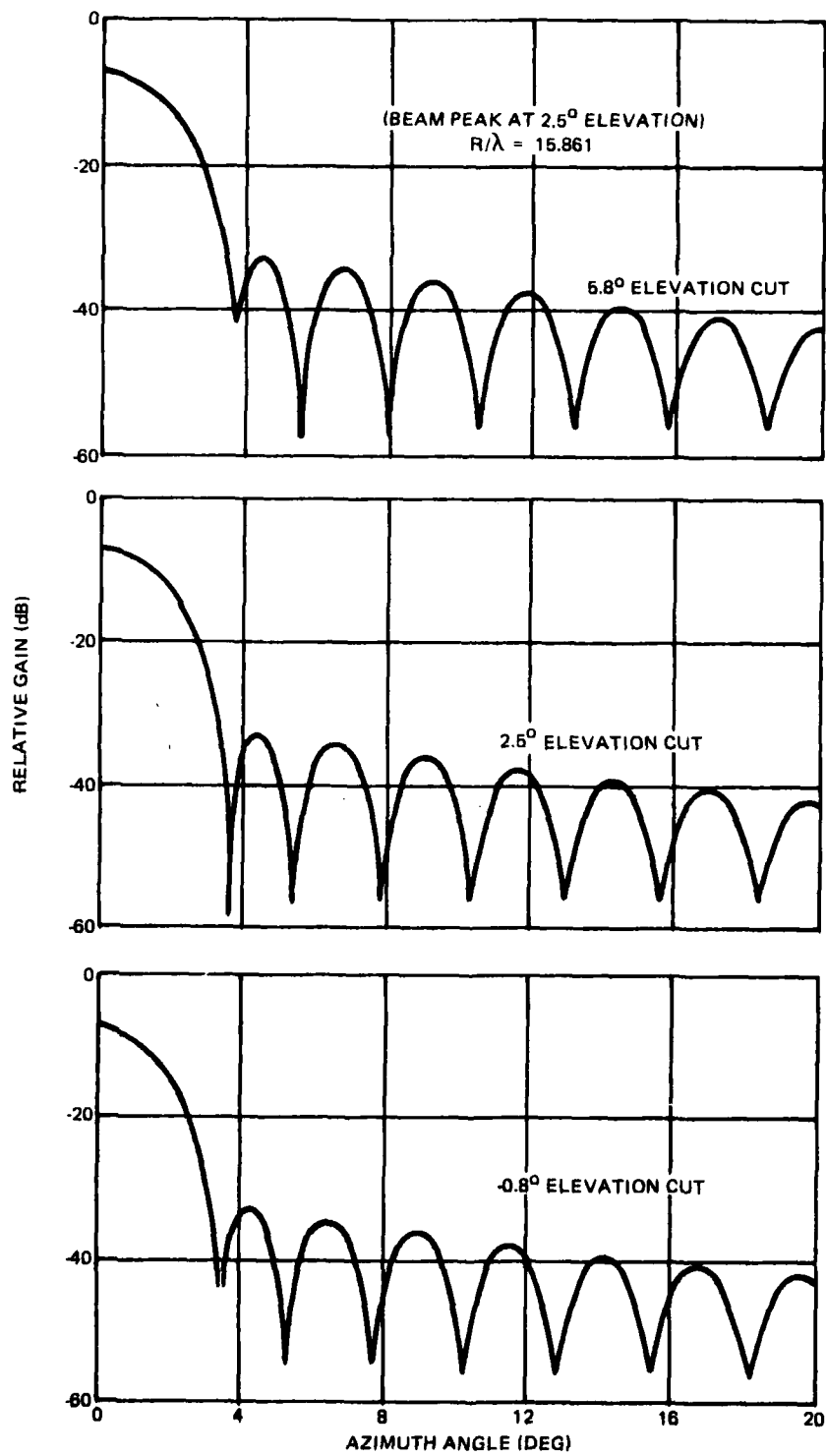
Figure 15. Azimuth Pattern Performance for Low Beam

60
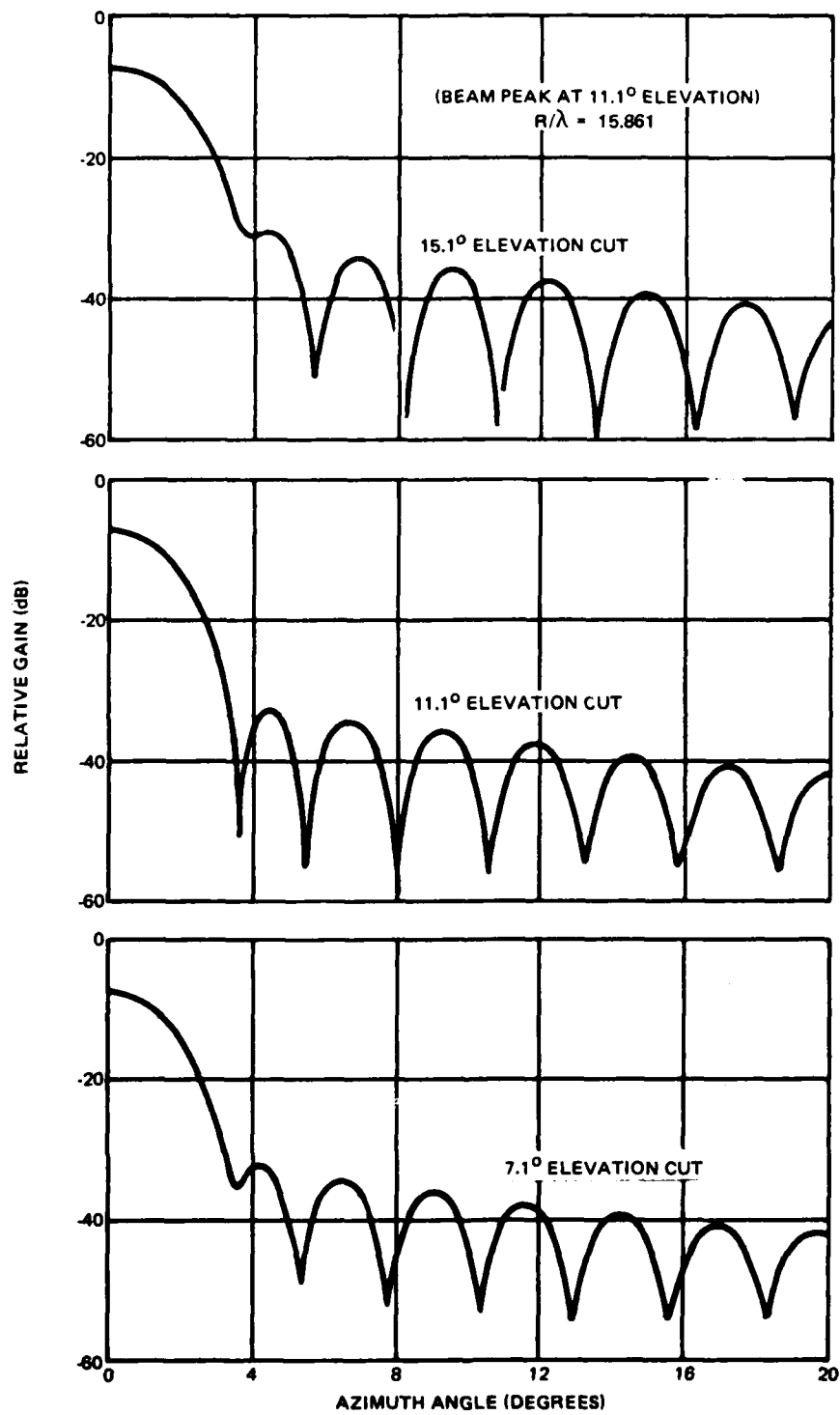
Figure 16. Azimuth Pattern Performance for Center Beam
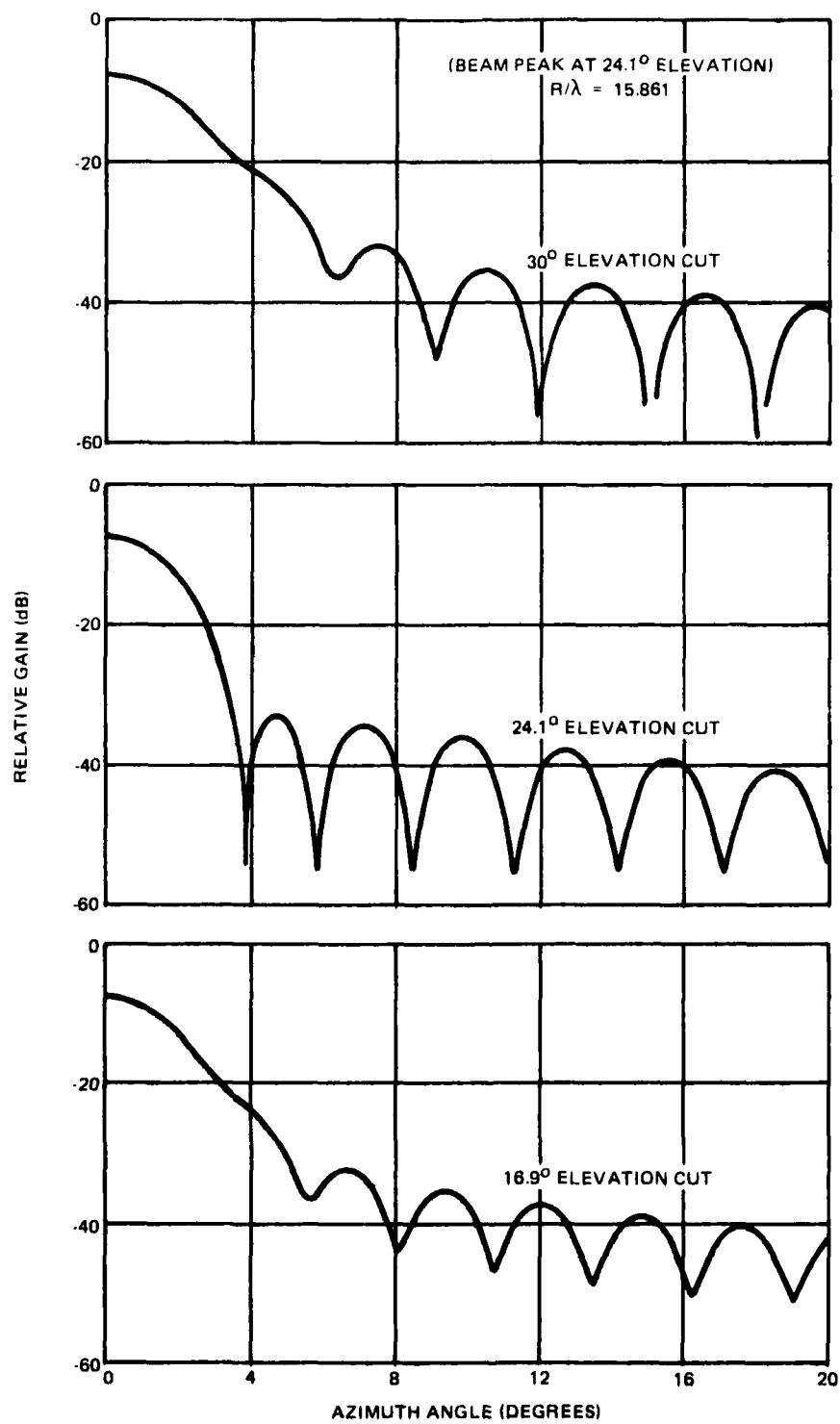
Figure 17. Azimuth Pattern Performance for High Beam

Beam collimation for the baseline cylindrical array is established using phase shifters within the azimuth switching network of figure 14. The phase delay in radians is given by:

$$\psi_i = \frac{-2 \pi R_o}{\lambda} \sin \theta_o \cos (a_i - a_o)$$

where a_i is the angular position of the ith element, a_i = 0, 2, 4, 6,...
(degrees) for 180 elements, and a_o is the azimuth beam position, a_o =
0, 3, 6, 9,... (degrees) for 120 beams. The quantity θ_o is the polar
elevation angle, where θ_o = 90 - 2.5 = 87.5 degrees for the lower beam,
θ_o = 90 - 11.1 = 78.9 degrees for the center beam and θ_o = 90 -24.1 =
65.9 degrees for the upper beam.

4.1.3.2 <u>Beam Coupling Loss</u>. The vertical plane pattern characteristics for
the cylindrical array are determined by the column network which provides
three independent beam channels. The non-orthogonal beam selection for the
baseline antenna requires a column network loss which is dependent upon beam
coupling. In general, the loss can be distributed between the three channels
in a variety of combinations. For minimum transmit power, the beam coupling
losses for the baseline antenna are 0.3 dB for the lower beam, 1.2 dB for the
center beam, and 0.5 dB for the upper beam.

The vertical column network for the baseline antenna is 12 feet in height
and contains 24 radiating elements. This aperture size exceeds the minimum
required for each of the three beams, thereby providing some flexibility to
minimize the aperture coupling factor and, as a result, minimize the network
loss. The selected design assigns elements 1 through 16 to the lower beam,
11 through 24 to the center beam, and 1 through 8 to the upper beam. This
arrangement results in coupling factors of S_{12} = 0.13, S_{13} = 0.035, and
S_{23} = 0.0, where the aperture coupling factor is defined as

$$S_{jk} = \sum_{i=1}^{N} V_{ji} V_{ki}*$$

with the aperture voltages normalized so that

$$\sum_{i=1}^{N} (V_{ji})^2 = \sum_{i=1}^{N} (V_{ki})^2 = 1$$

Coupling loss for a network can be derived in terms of the coupling fac-
tor. With a two-channel network, as an example, the resulting minimum loss

- - - - - - -

*conjugate

63

in each of the two channels is shown in figure 18 with coupling factor as a parameter. With equal loss in each channel, the db value is given by

$$L = 10 \log [1/(1 + S)]$$

For orthogonal beams, S = 0, and the network can be lossless. For S ≠ 0, the loss can be apportioned between the channels in various ratios. For zero loss in either channel, the loss in the other channel must become infinite. For S - 0.13 as an example, the loss from figure 18 can be selected as 0.25 dB for the primary channel and 1.1 dB for the secondary channel. Equal loss for both channels would result in a value of 0.53 dB.

Coupling loss for the baseline three-channel network has been programmed for computer solution. The program uses an iterative procedure to apportion the losses for minimum transmitter drive power.

4.1.3.3 Gain and Loss Budget. The gain and losses for the baseline antenna are itemized in table 9. The antenna directivity is based upon an azimuth beamwidth of 3 degrees and elevation beamwidths of 6.75, 8.0, and 14.5 degrees for the low, mid, and high beams, respectively. The column network is a three-channel series stripline network with dipole radiators and has a loss of 0.8 dB. Due to non-orthogonality of the elevation beams, there is an additional column network coupling loss of 0.3, 1.2, and 0.5 dB for the low, mid and high beams, respectively. The loss for 15 feet of coaxial cable from the column networks is 0.7 dB, and the loss of the SP4T switch is 0.5 dB. The azimuth switching network, consisting of diode phase shifters and an amplitude commutator, has a loss of 1.8 dB. The total dissipative loss, as indicated in table 9, is 5.1, 5.8, and 5.1 dB.

Table 9. Antenna Gain and Loss Budget

	High Beam	Mid Beam	Low Beam
Antenna Directivity (dBi)	29.5	32.1	32.8
Dissipative Losses (dB)			
Column Network	0.8	0.8	0.8
Orthogonality Loss	0.5	1.2	0.3
Transmission Line Cable	0.7	0.7	0.7
SP4T Switch	0.5	0.5	0.5
Circulator	-	-	0.7
Azimuth Switching Network	1.8	1.8	1.8
Interconnecting Cables	0.3	0.3	0.3
Duplexer	0.5	0.5	-
Total Losses (dB)	5.1	5.8	5.1
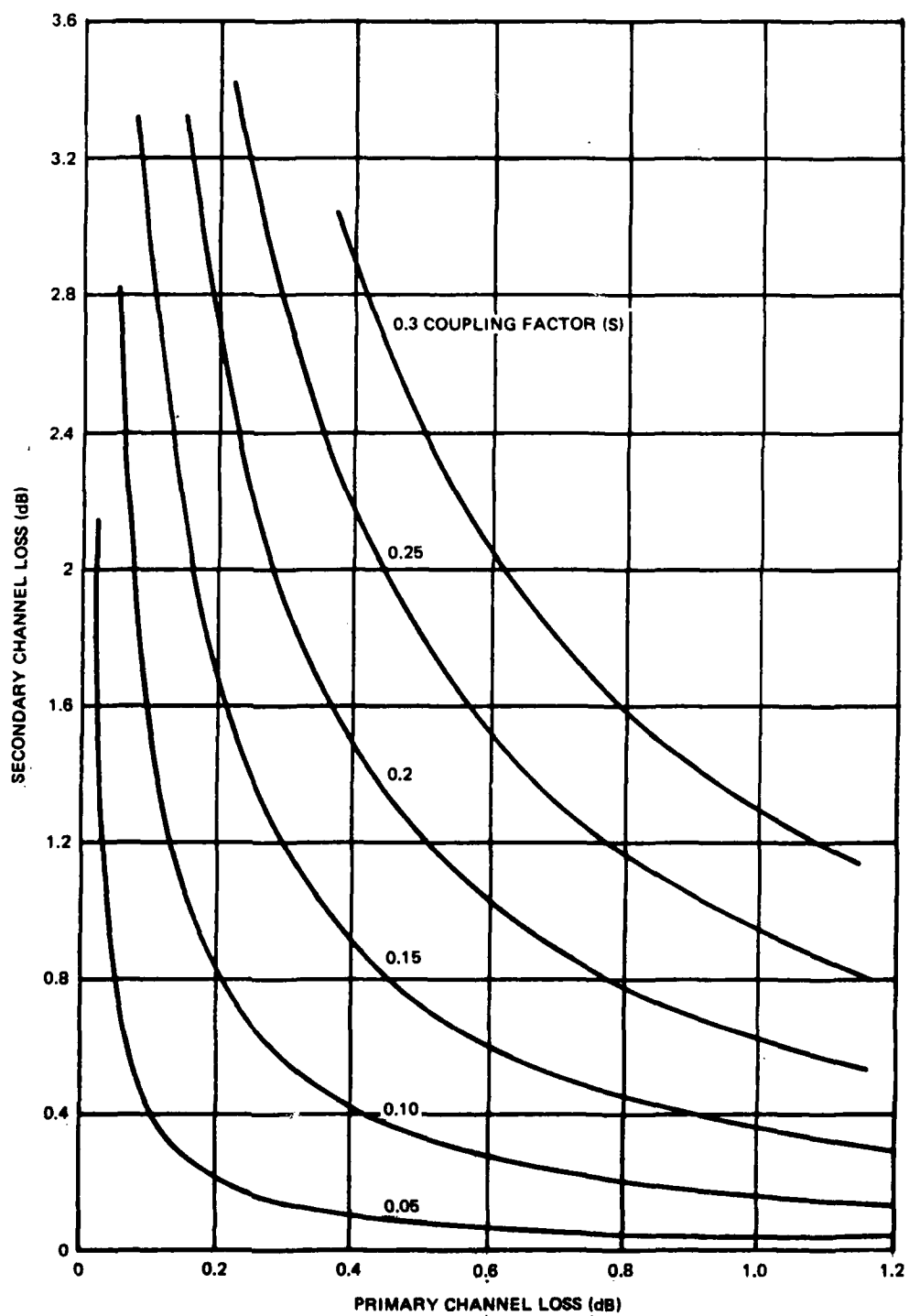
Figure 18. Dual Channel Network Coupling Loss for Non-Orthogonal Beams

4.1.4 BEAM STEERING SYSTEM

The beam steering computer (BSC) for the baseline antenna of figure 14 consists of the electronic circuitry and diode drivers required to establish the azimuth beam positions. To form a selected beam, it performs five functions:

- Provides logic inputs to the quadrant switch drivers to determine which quadrant of column networks is to be active for a particular beam.

- Provides phase information to perform beam collimation and fine steering.

- Provides the amplitude commutation network switching data.

- Provides switching information to the solid state transmitter amplifiers.

- Provides automatic fault detection and status monitoring.

The low data rate required to form thirty beams per second, and the sharing of phase computation resulting from the even steering function, permit the use of low power and high reliability CMOS circuitry.

The baseline antenna uses a combination of electronic network switching and phasing to collimate and steer the beam. Azimuth steering is provided by electronically commutating the azimuth beam-forming network to interconnect with the selected column networks, and then setting the azimuth phase function to fine-steer and collimate the beam.

The baseline system provides beams at 3-degree azimuth increments, but the design is sufficiently flexible for implementing other steering requirements. The phase computed for the azimuth beam steering is:

$$\psi_1 = \frac{-2 \pi R_o}{\lambda} \sin \theta_o \cos (a_1 - a_o)$$

where: R_o = cylinder radius

λ = wavelength

θ_o = polar elevation angle measured from zenith

a_1 = azimuth of the ith elevation column in the sector

a_o = steered azimuth angle.

This function, which both steers the beam in azimuth and compensates for azimuthal defocussing of the beam as a function of elevation, is computed in the mathematical unit and sent to the azimuthal phase shifter drivers. The sine and cosine functions in the phase expressions are stored in ROM's.

66

The number of stored sine values is dependent upon the number of elevation beams. The number of stored cosine values is a function of the azimuth beam stepping granularity, but since the value of the function $\cos(a_1 - a_0)$ is repeated in each sector, and is an even function, values for only half the number of beams in a sector need be stored. For any beam step granularity consistent with the phase shifter LSB, storage is consistent with reasonable hardware implementation. The mathematical unit calculates the value of $[2\pi R/\lambda]$ $[\cos(a_1 - a_0)]$, and then sequences through the sine table to calculate the proper phase value which is distributed by the phase demultiplexer to the proper phase shifter driver(s).

The block diagram of the beam steering is illustrated in figure 19 which shows the interconnections of the beam steering computer with the switch
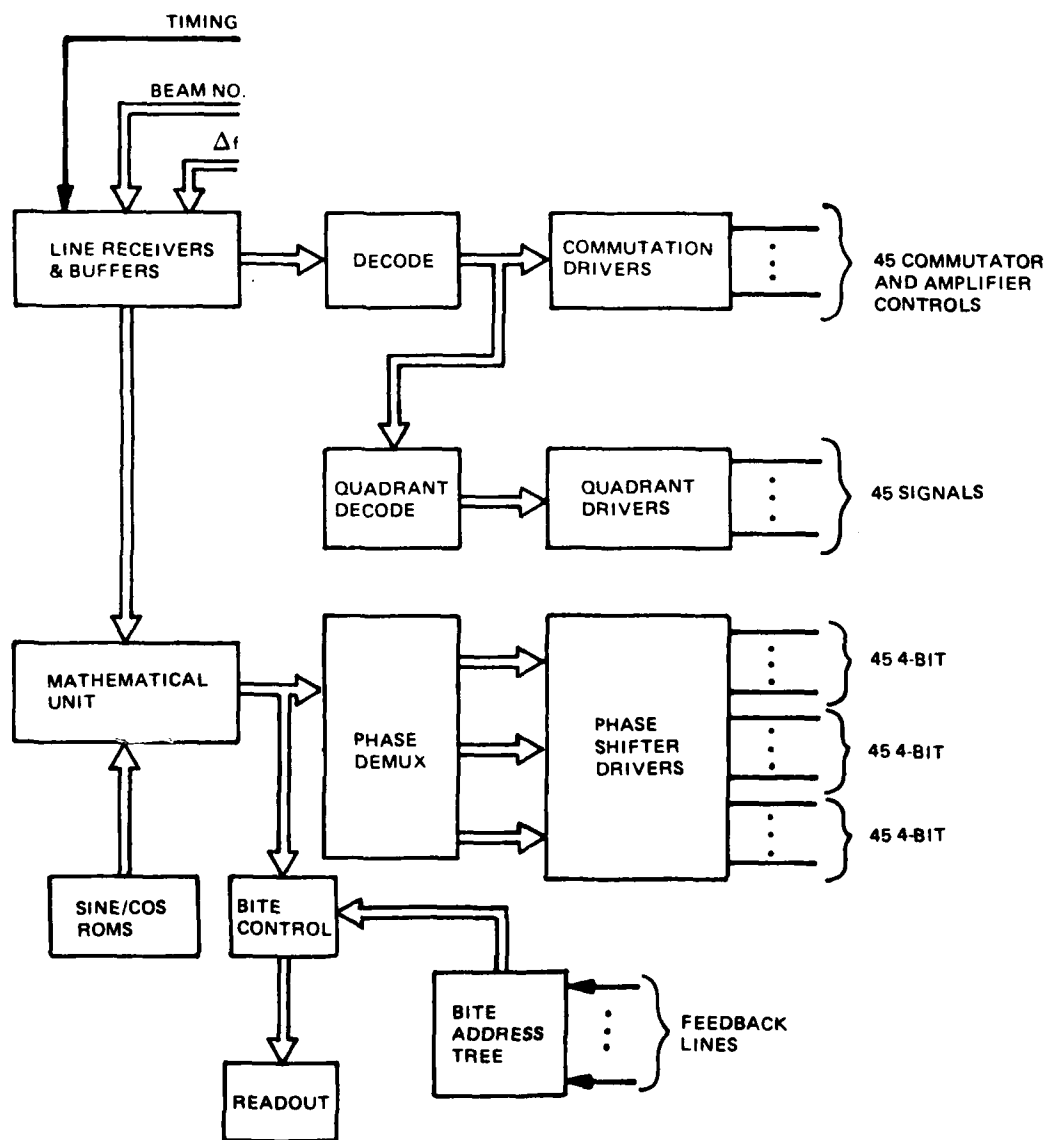
Figure 19. Beam Steering Computer, Block Diagram

67
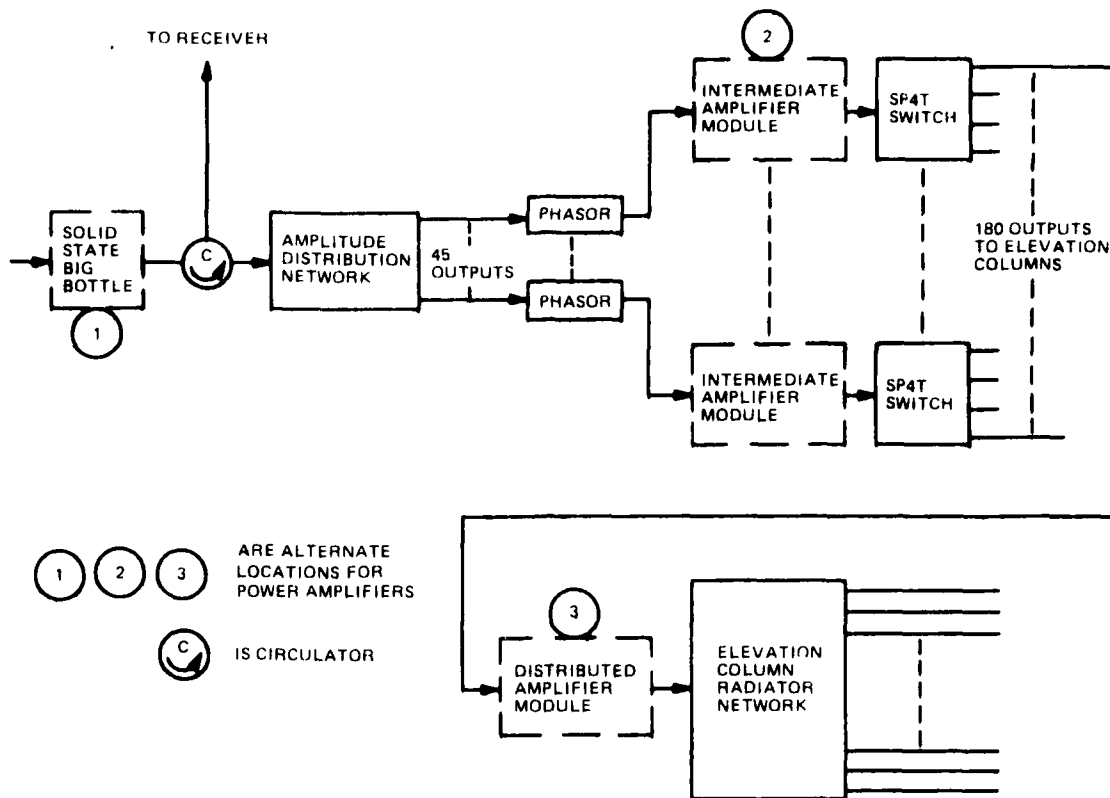
Figure 20.   RF System Block Diagram Showing Alternative Locations
for Power Amplifiers

drivers, phase shifter drivers, and BITE circuitry. This type of circuitry
is easy to obtain with current technology, and has been implemented by Sperry
on designs such as the TPQ-37 Radar and the Hemispheric Coverage Antenna.
The beam setup time is 40 microseconds from receipt of steering data until
the PIN diode phase shifters are set.

4.2   SOLID STATE BOTTLE TRANSMITTER/ANTENNA MODULE

A number of RF configurations were evaluated in detail for the solid
state transmitter system. The major objectives were to select the most cost-
effective system that would provide low power consumption and high reliabi-
lity. The configurations studied consisted of locating the major amplifiers
at three different extreme locations in the RF system. As indicated in
figure 20, these positions include the following:

● Solid State Big Bottle – The required transmit RF power is obtained
   from a big bottle solid state amplifier assembly located at the
   input to the azimuth and elevation RF distribution system.

- **Intermediate Amplifier Modules** - Forty-five separate amplifier modules located at each output of the azimuth distribution network prior to the SP4T sector switches.

- **Distributed Amplifier Modules** - One hundred eighty separate amplifier modules located at the input to each column network.

The trade-off study was performed for two different radiated RF power conditions: 2.5 kilowatts P_k at 10 percent duty cycle and 5.0 kilowatts P_k at 7 percent duty cycle. Both power levels were for 100-microsecond pulsewidths. A comparison was also performed using low noise receive amplification. All of the studies included the following considerations:

- Effects of amplitude tapering for the power amplifiers

- Alternate azimuth distribution networks required

- Prime power and power supply costs

- Alternate combining techniques

- Production.

One of the most important considerations for the trade-off study was the selection of the high power transistor to be used as the basic building block for the power amplifiers. After extensive study, Sperry selected the TRW-296 transistor. Its typical performance is illustrated in figure 21, and it is the basic building block for the three-configuration trade-off. The results of the trade-off investigation are summarized in table 10. As the RF amplifiers are located closer to the radiating elements, the transmitter system becomes more efficient. However, amplification at the elements in a commutating cylindrical array is more costly since it requires more transistors and modules. Consequently, the optimum approach is a compromise between prime power consumption and costs.

As a result of the above trade-off investigation, the proposed solid state transmitter configuration for the RRAS baseline system is a combination of a medium power bottle (solid state transmitter) and
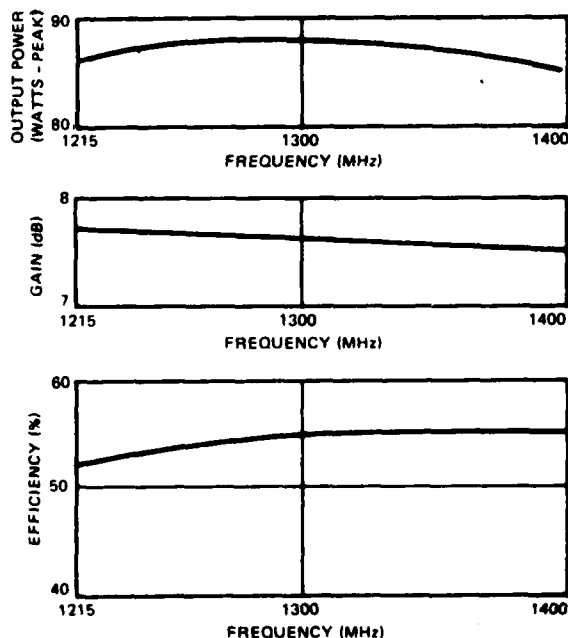
Figure 21. Test Data For TRW MRA-296 Transistor

intermediate transmit amplifier modules. The solid state transmitter will provide the transmit power for the two upper beams and the drive signals for the transmit amplifier modules. The final amplification for the low beam transmit signal is provided by the transmit amplifier modules located in each output of the azimuth distribution network.

Table 10. Solid State Transmitter Comparison Results

	2.5 kw Transmit Power		5.0 kw Transmit Power	
Configuration	Relative Cost/System	Prime Power Watts/System	Relative Cost/System	Prime Power Watts/System
Solid State Big Bottle	1.0	860	1.7	1200
Intermediate Module				
● W-LNA	1.9	370	3.0	550
● W/O-LNA	1.6	600	2.5	740
Distributed Module				
● W-LNA	4.0	250	-	-
● W/O-LNA	3.6	430	-	-

Note: LNA denotes low-noise amplification.

The anticipated performance and parameters for the solid state transmitter and transmit amplifier modules are listed below:

	Solid State Transmitter	Transmit Amplifier Modules (45)
Output Power (peak watts)	540	2450 (total)*
Gain (dB)	25.6	18.0
Efficiency	37%	42%
Vcc (volts)	32	32
Prime Power (average watts) (10% DC)	145	590
MTTR (replace spare module)	1/2 hr	1/2 hr
Size (inches)	12x8x6	60x12x6
Weight (lbs)	10	80

- - - - - - -

*Includes amplitude tapering effect.

70
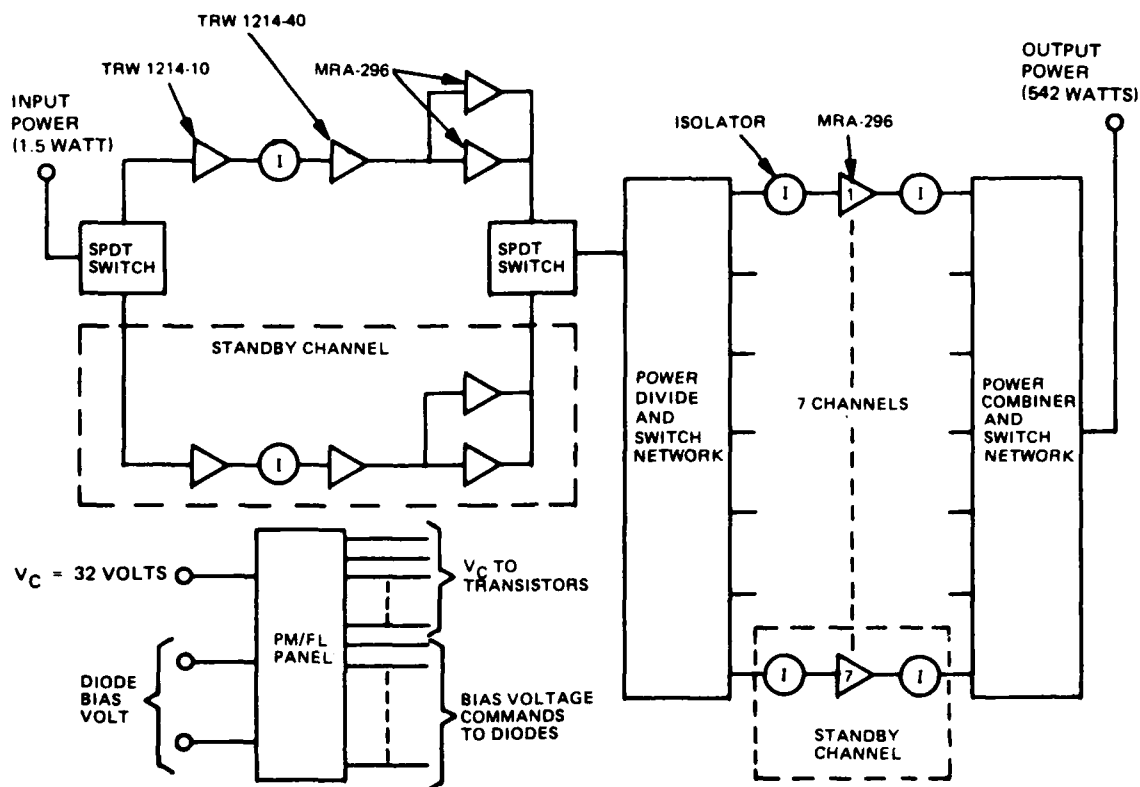
Figure 22. Solid State Transmitter, Block Diagram

A block diagram for the proposed solid state transmitter is presented in figure 22. It consists of a driver module with two identical 3-stage amplifier channels connected at their input and output by a SPDT diode switch. One of the channels is a stand-by unit that is automatically switched into the circuit when there is failure to the operating channel. The output from the driver module is distributed equally to six of the seven paralleled output stage transistors through a 1P6T power divider/switch network. The seventh output transistor amplifier is a stand-by unit that is automatically switched into the circuit when there is a failure in any of the six operating amplifiers. The output power from the six operating transistors is efficiently combined in an identical 1P6T power combiner/switch network. These networks are stripline, center fed, reactive power dividers with shunt-mounted diodes in each of the seven output arms located a quarter wavelength from the center junction. The input signal can be distributed equally to any six of the seven outputs with the proper biasing of the diodes. With 1.5 watts peak RF input power, the solid state transmitter will provide 542 watts peak output power at a collector voltage of 32 volts. About 475 watts will be used for the two upper beams and the remainder (67 watts) will be used to drive the 45 transmit amplifier modules for the low beam.

71

The concept of self healing, using stand-by amplifiers that auto-
matically replace failed units, has been demonstrated by Sperry during the
acceptance tests of the 2.5-kilowatt solid state, L-band transmitter
developed for RADC. Reliability calculations for the RADC program indicated
two orders of magnitude improvement in reliability with the use of one
stand-by module. Consequently, this technique of self-healing is a
practical, cost-effective approach for obtaining significant improvement in
reliability.

A performance monitoring and fault locating (PM/FL) panel will be used to
provide the sensing, logic, and switching circuits to monitor the transistor
collector curents and automatically replace a failed amplifier with a stand-
by unit.

A block diagram of the 45 transmit amplifier modules used for the low
beam signal is presented in figure 23. Each of the 45 identical amplifier
channels contain three stages of amplification and a duplexer to separate the
transmit and receive signals. The duplexer consists of a circulator and a
SPDT diode switch arrangement. This configuration efficiently separates the
transmit and receive signals, and it also converts the circulator at the
output of the module to an isolator during the transmit mode. This protects
the output stage from antenna load variations.
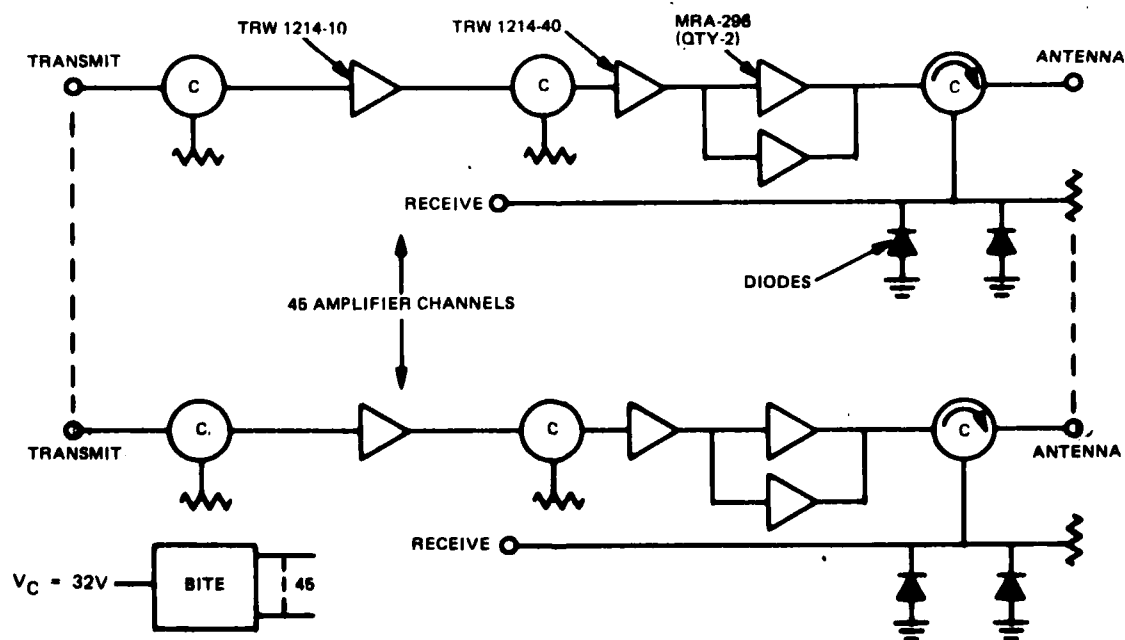
Figure 23. Transmit Amplifier Modules, Block Diagram

72
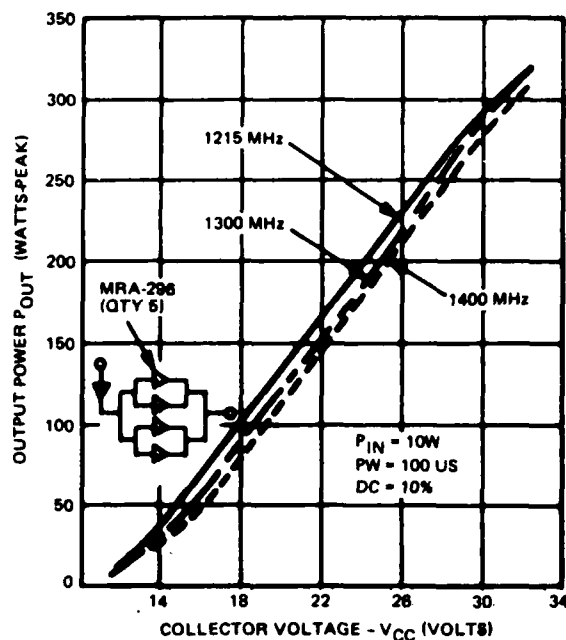
Figure 24. Breadboard Module
Test Data

The maximum RF transmit output power from any one of the 45 amplifier modules is about 110 watts peak with 0.85 watt RF input. This RF output power must be reduced from the maximum value for a range of about 13 dB to provide the desired azimuth illumination taper for sidelobe control. This will be accomplished by reducing the collector supply voltages where necessary. A typical amplifier response for the output power variation as a function of the collector voltage is presented in figure 24. The test data are for a two-stage amplifier module, using the MRA-296 transistors, developed for the 2.5-kilowatt L-band amplifier for RADC. As indicated, there is a fairly linear, 13 dB reduction of output power as the collector voltage is reduced from 32 volts to 12 volts. Since the proposed transmit amplifier modules contain three stages of amplification, a smaller voltage reduction will be required for the 13 dB output power reduction.

The concept of graceful degradation can be applied for the 45 separate transmit amplifier modules. When one of the transistors fail, the loss of that channel will not seriously affect the array performance. As a result, it is not necessary to use stand-by amplifiers to achieve the required reliability.

4.3 FREQUENCY SYNTHESIZER

The frequency synthesizer provides all the RF signals for the system, i.e., receiver local oscillator and coherent oscillator (COHO), as well as modulated transmitter excitation. Frequency agility (25 transmitter and local oscillator frequencies) is provided with quartz crystal stability, low phase noise, and low power consumption. Direct frequency synthesis is employed to permit fast frequency switching. No phase-lock circuits are employed, resulting in enhanced reliability and switching times of one microsecond or less.

A block diagram of the frequency synthesizer is shown in figure 25. Generation of the frequency agile local oscillator signal is accomplished by mixing the outputs from the crystal oscillator assembly, one of which is frequency multiplied by a factor of five. The five crystal oscillators are operating continuously for stability and to permit fast frequency selection. Isolation between oscillators (through filtering and shielding) prevents any
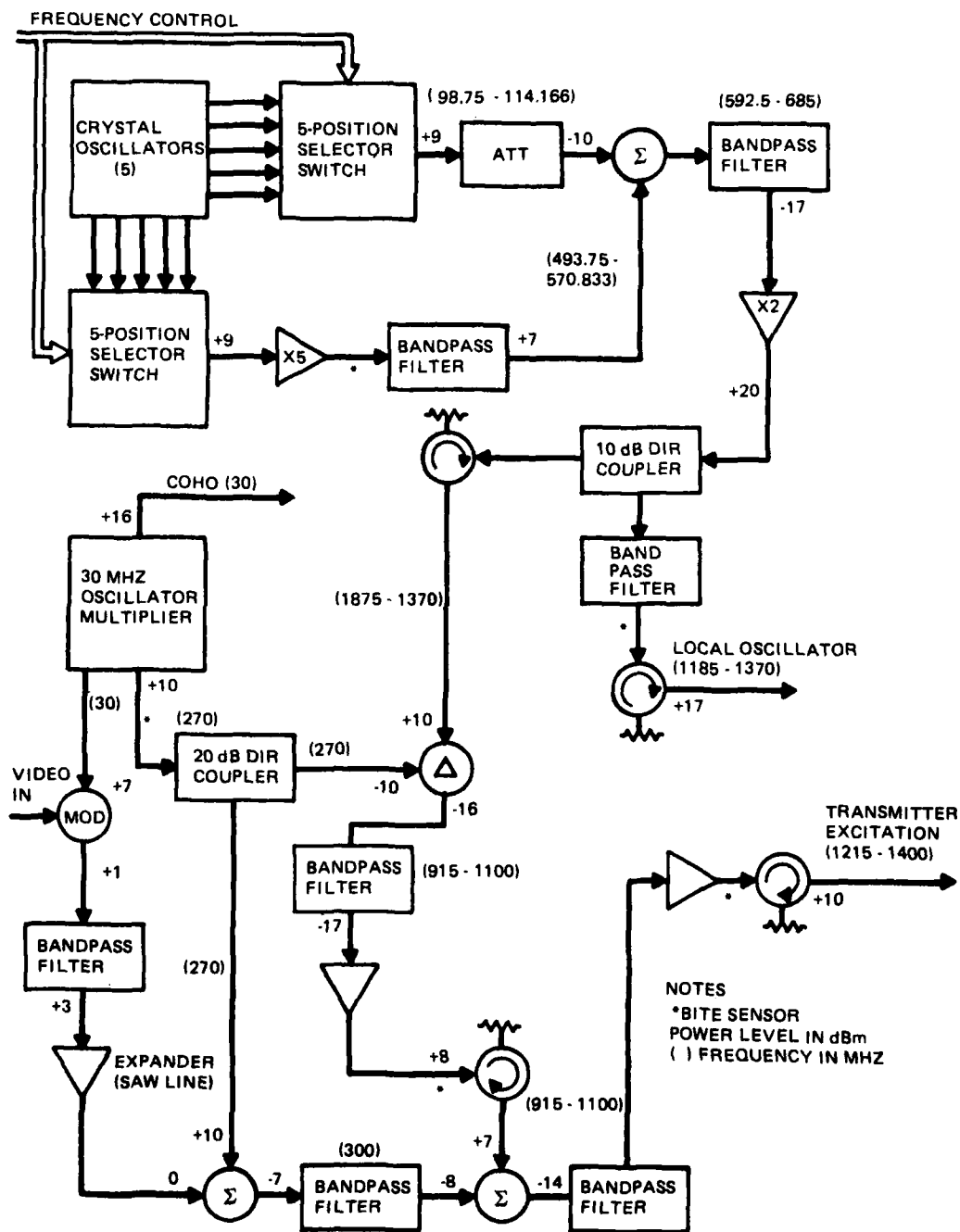
Figure 25. Frequency Synthesizer, Block Diagram

measurable crosstalk. The five-position selector switches also must provide isolation of over 100 dB to prevent spurious signals. The crystal oscillators are of low phase noise design and operate at fairly high level to enhance the signal-to-noise ratio. The frequencies of the oscillators and the multiplication factor of five were chosen to provide equal spacing between the twenty-five frequencies, approximately 7.7 MHz at the L.O. output. A bandpass filter at the mixer output passes the upper sideband, rejecting the carrier and lower sideband. Carrier rejection (60 dB) is also provided by the excellent isolation of the double-balanced mixer. This type of mixer is used throughout the synthesizer because of its inherent suppression of harmonic intermodulation products. An active frequency doubler followed by a directional coupler, bandpass filter, and isolator complete the local oscillator channel. The 30-MHz oscillator multiplier supplies the COHO signal for the receiver system and another 30 MHz signal for the pulse modulator. In addition, an integral multiplier develops the ninth harmonic of 30 MHz which is used in translating the local oscillator to the transmitter frequency. The 270-MHz signal is mixed with the 30-MHz expanded pulse and the upper sideband, centered at 300 MHz, is filtered and applied to the final mixer in the transmitter exciter chain. The other input is the difference frequency obtained by mixing 270 MHz and the local oscillator signal. Suitable amplifiers in the exciter chain recover the losses of filters and the mixing processes. The transmitter frequency thus tracks the L.O. at 30 MHz above the L.O.

4.3.1 Synthesizer Parameters and Characteristics

- Local Oscillator

    - 25 frequencies spaced 7.7 MHz from 1185 to 1370 MHz, 30 MHz below transmitter frequency at a power level of +17 dBm $\pm$1.5 dB.

    - Spurious output: -80 dBc in band; -120 dBc in either 1-MHz band $\pm$30 MHz from the carrier.

    - Spectral density of phase noise: In a 1.0-Hz bandwidth, noise power at 60 Hz from the carrier shall be -82 dBc and decrease at a rate of 9 dB/octave (or more) from 60 Hz to 3 kHz from the carrier. From 2 kHz to 500 kHz, a decrease in rate is permissible, provided the signal-to-noise ratio from 10 kHz to 500 kHz exceeds -138 dBc.

- COHO: 30 MHz tolerance $\pm$5 x 10^{-5} at +16 dBm into 50-ohm load. Sinusoidal waveform.

- Transmitter Excitation: 1215 to 1400 MHz, + 10 dBm $\pm$1.5 dB peak FM pulse. Spurious output: -40 dBc in band; -60 dBc out-of-band.

- BITE: Five sensors producing an analog voltage proportional to power will be provided. The following points will be monitored:

    - Output of X5 multiplier, band selection frequencies

    - Local oscillator

- Transmitter excitation

- Exciter translation frequency 270 MHz

- Exciter intermediate frequency 915-1100 MHz.

4.3.2 Input Requirements

- Frequency Selection: Two 5-line inputs TTL level

- Video Input: Positive 40 ma pulse, dimension TBA

- DC Input:

  - +5 volts at 0.6 ampere   - 3.0 watts
  - -5 volts at 0.6 ampere   - 3.0 watts
  - +28 volts at 0.85 ampere   - 23.8 watts
  - +15 volts at 0.2 ampere   - 3.0 watts
  - -15 volts at 0.1 ampere   - 1.5 watts
  - Total power input   34.3 watts

4.3.3 Physical Characteristics

- Weight: Estimated 60 pounds, not including power supply

- Volume: 2 cubic feet

4.4 DIGITAL SIGNAL PROCESSOR

The baseline signal processor is implemented as an all-digital, special purpose device in three parallel channels. Each channel is functionally identical. Two are active, processing data from the three elevation beams, and the third is provided for redundancy. The lowest elevation beam has an active channel which it does not share; the two upper beams, which are shorter range, share the other active channel. When the on-line, built-in test equipment (BITE) senses a failure in a portion of an active channel, the clocks in that failed portion are stopped, and the corresponding portion of the redundant channel is activated. Since the hardware is implemented using CMOS logic, unclocked hardware dissipates negligible power, and it is not required that the supply voltage be disconnected from that channel.

The primary subsystems of the signal processor are the 3-pulse MTI, 8-filter doppler filter bank, pulse compression network and CFAR, and clutter map. Table 11 lists the signal processor parameters.

The waveform described in table 11 is a 9-pulse burst, of which eight are processed in the doppler filter bank. The ninth pulse serves to give full cancellation on second-time-around clutter. An interesting option that can be implemented is the use of the ninth pulse only for azimuths where second-time-around clutter is prevalent.

76

Table 11. Signal Processor Parameters

Waveform	Pulse burst of nine uniformly spaced pulses
Pulse Compression	32:1, 64 microseconds to 2.0 microseconds using linear FM
prf	1239, 1231, 982, 976 Hz
Doppler Filtration	Eight filters, including zero-doppler filter, processing eight pulses
A/D Converter	10 bits, I and Q
Sampling Rate	1.0 microsecond between samples; two samples per compressed pulsewidth
SCI Limitation	>60 dB on ground clutter; >35 dB on sea clutter
CFAR	Hard limiting before 32:1 pulse compression for filters 1-7. Variable threshold based on clutter map for filter 0.
Clutter Map	32 dB dynamic range, exponentially smoothed using 7/8ths loop gain

The functional block diagram for the signal processor, figure 26, shows the major functions performed in any one of the three parallel signal processing channels. I and Q video from synchronous detectors are converted to numerical form by 10-bit A/D converters located in the receiver. These are strobed every microsecond, or twice per compressed pulsewidth. Double sampling saves about one dB in losses over single sampling.

Automatic adjustment circuitry is implemented to compensate for drifts and tolerances in the receiver and A/D converter. No manual field adjustments are included anywhere in the signal processor. The automatic noise level adjustment circuitry is implemented to maintain the receiver noise at the proper level into the A/D converter. This level is not critical since CFAR circuitry following the doppler filters fixes the false alarm rate, but it is required to preserve the balance between quantization loss and dynamic range in the A/D converters. The noise level is measured in dead time by summing noise samples from 128 independent range cells prior to burst transmission to estimate noise level. Every other range cell is phase reversed so as to cancel DC levels from the measurement.

DC offset measuring circuitry is provided to compensate for DC level drifts in the A/D converters and the synchronous detectors. This is implemented only in the zero-doppler filter line, since the MTI cancellers in the other line block DC. The measurement is taken independently on the I and Q lines during the same dead time as the noise level measurement so that large signals do not bias it. Compensation is done digitally by subtracting

77

the measured DC offset from the output of filter zero, scaling by the filter DC gain. This is the most appropriate point for compensation since it has the highest DC sensitivity, e.g., a 1/4-bit measured average DC offset corresponds to two bits at this point. In the pulse compression network that follows, the DC gain is 3 dB less than the noise gain.

Data from the A/D converters proceeds into a buffer memory. From the buffer memory, the data are split into two parallel paths - one for the zero-doppler filter which is implemented to catch near tangential targets and the other for filters 1 through 7 which provide signal-to-clutter improvement for targets with radial velocity. All signals in the non-zero doppler channel proceed through a 3-pulse MTI which is implemented as a cascade of two 2-pulse cancellers. The 3-pulse MTI contributes two zeros of transmissions at zero velocity to the overall filter responses of the non-zero-doppler filters which process a total of eight pulses.

To decrease the dynamic range of the signals that must be processed in the doppler filter bank, vector limiters are incorporated which reduce the number of parallel bits from 12 to 6 out of the MTI, and from 10 to 6 in the zero-doppler filter line. Clutter residues out of the MTI have been reduced to well under six bits at this point, so that no limiting on clutter, and thus no doppler spreading of clutter, occurs. Only very large signals are limited, corresponding to about 55 dB after doppler filtration and pulse compression. In the zero-doppler filter line, clutter greater than 55 dB is limited, but no clutter cancellation is attempted here, and doppler spreading is of no consequence. Hardware is thereby saved and no detectability is lost since only unrealistically large targets could be seen in this level of clutter.

The vector limiter emulates an IF limiter; the phase relationships at the output are the same as those at the input. Signals below the limit level are passed unchanged, while signals above the limit level maintain the same ratio of I and Q, but each is reduced by the same factor to bring the envelope to the limit level. This is implemented by taking logarithms of the absolute values of I and Q in a log ROM, and subtracting them. The resulting number, along with the sign bits for I and Q, are used to address another ROM which outputs the new values of I and Q limited to six bits. This implementation was used as a hardware saving measure on the AN/TPQ-37 signal processor and on other Sperry programs. Signals from the vector limiter proceed to the doppler filter bank. Figure 27 shows the implementation of this filter bank.

At the output of the doppler filter bank, the filter outputs from filters 1 through 7 are time sequenced onto one pair of I and Q lines. The entire contents in range of one filter are read out of memory to the output, while the contents of the other filters are held until they too are sequenced out. The six bits at the input to the doppler filters have grown to nine bits. These are vector hard limited to three bits, prior to pulse compression processing, to effect a CFAR implementation. The vector hard limiter differs from the vector limiter discussed before in that signals below the limit level are brought up to the limit level while maintaining their original phase relationship. A phase-only signal with no amplitude information results. The implementation is almost identical to the vector limiter discussed previously.

78

VIDEO FROM
SYNCHRONOUS
DETECTORS

10-BIT A/D CONVERTER — BUFFER MEMORY — 10 — 3-PULSE MTI — 12 — VECTOR LIMITER — 6 — DOPPLER FILTER BANK FILTERS 1-7 — 9 — VECTOR HARD LIMITER — 3

10-BIT A/D CONVERTER — BUFFER MEMORY — 10 — 3-PULSE MTI — 12

VECTOR LIMITER — FILTER 8 — Σ — BIT SLICE SEQUEL

Σ

DC OFFSET MEAS.

DC OFFSET MEAS.

NOISE LEVEL MEAS.

TO RECEIVER AGC

A/D STROBES   CLOCK PULSES   GATES + TIMING PULSES

CLOCK GENERATOR — PRF AND TIMING GENERATOR — PRF PULSES

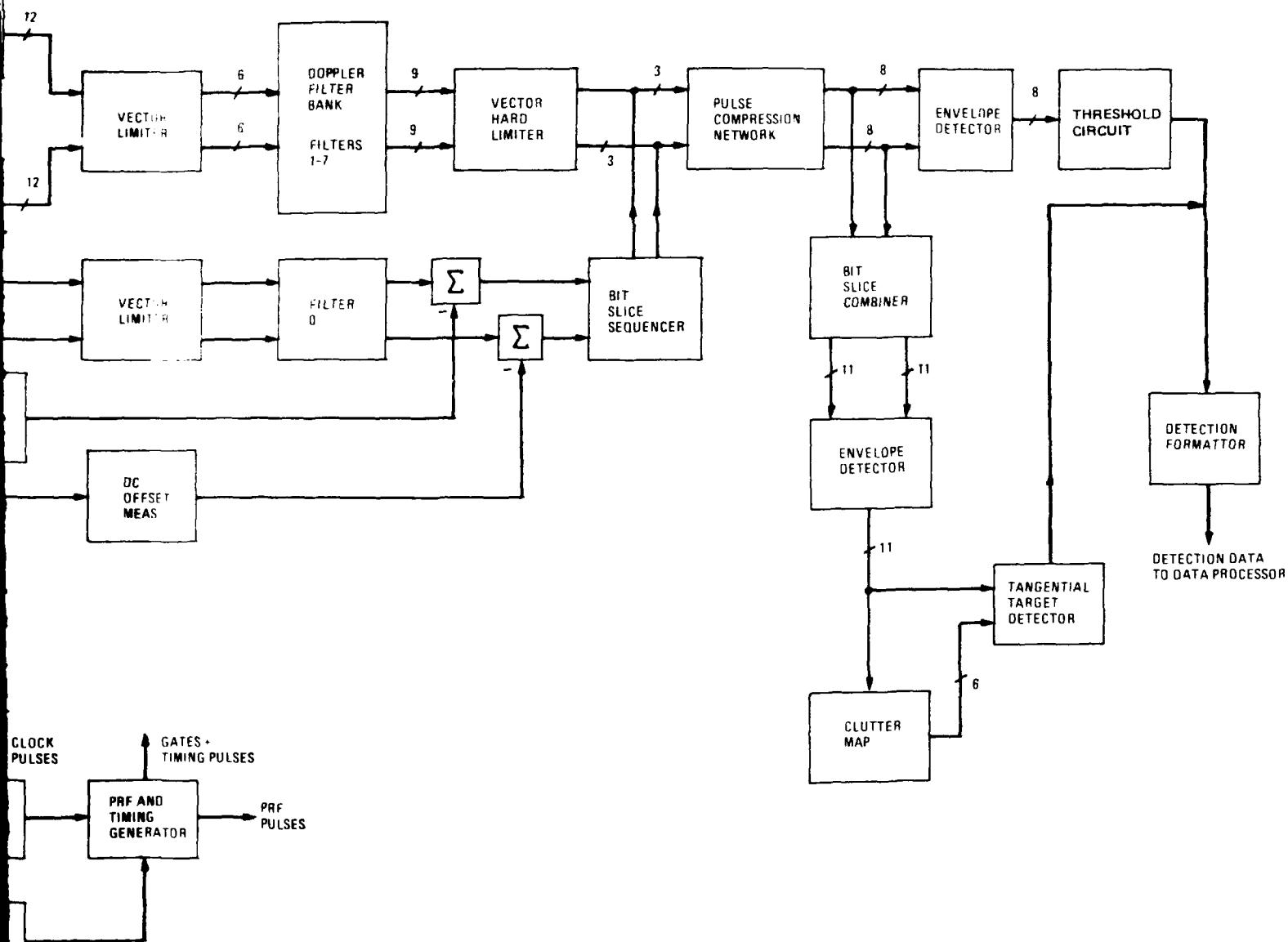DATA PROCESSOR COMMANDS — COMPUTER INTERFACE

1

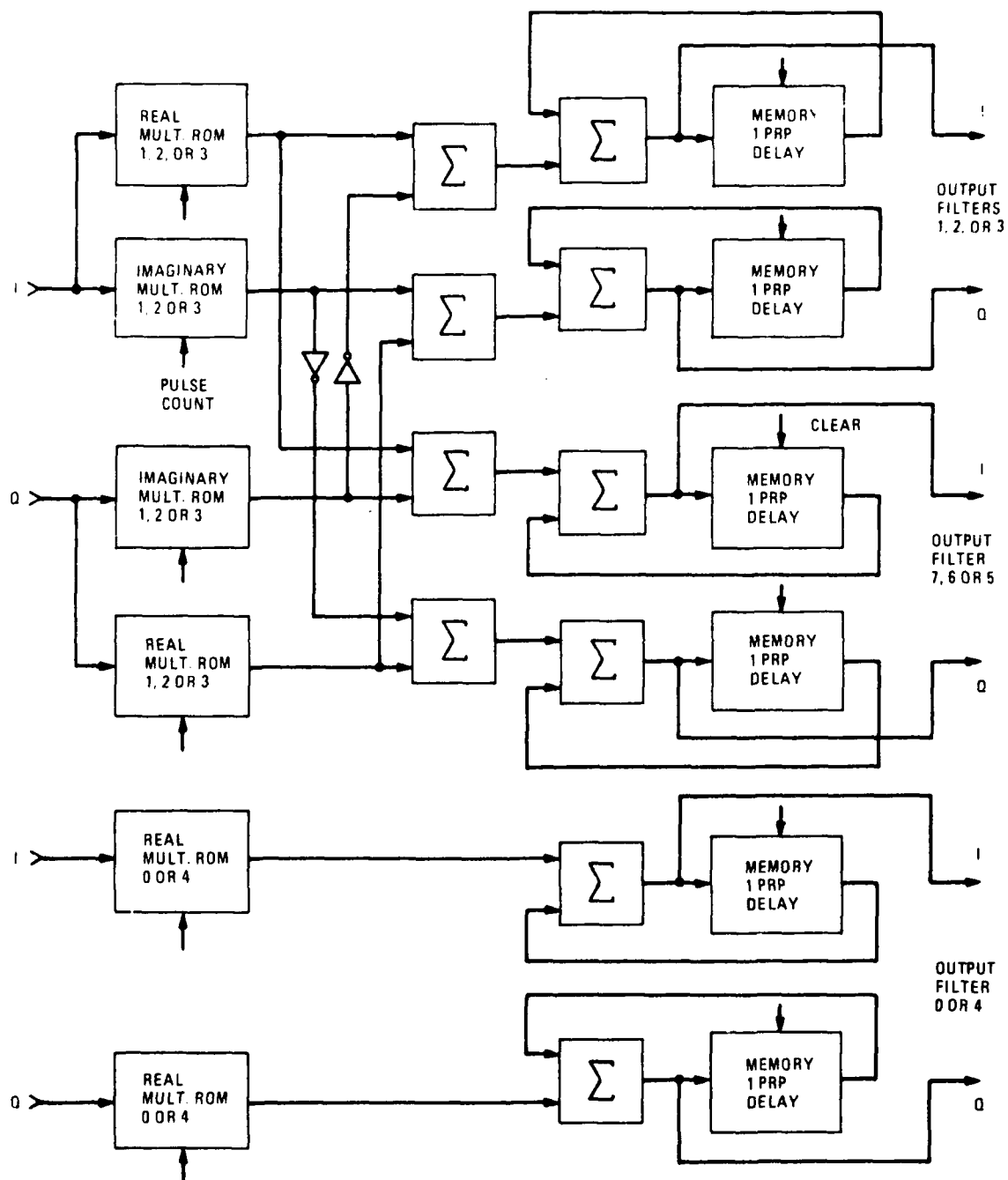Figure 26. Signal Processor, Functional Block Diagram

79

Figure 27. Doppler Filter Implementation

The pulse compression network is implemented as a finite impulse response digital filter operating on complex (real and imaginary parts) signal samples. The impulse response of the filter is designed to be the complex conjugate of the signal at the sample points. The signal modulation is a linear FM chirp, which corresponds to a parabolic phase modulation at the center frequency. Therefore, the impulse response of the filter has a constant amplitude over the duration of the uncompressed pulse, and a parabolic phase characteristic at the sample points. The time-bandwidth product of the waveform is 32 - hence, 32 complex signal samples are processed together in the pulse compression. This corresponds to the Nyquist sample rate. The parabolic phase characteristic at the 32 sample points is given by:

$$\emptyset_i = [i(i-1)/2] \ [2\pi/32] \ \text{modulo} \ 2\pi, \ -15 \leq i \leq 16$$

This function tracks the linear FM phase function if the samples are taken symmetrically across the pulse (optimum time of arrival).

Built-in test equipment (BITE) circuitry is essential for the unattended radar operation since it not only has the function of monitoring and locating faults, but it also corrects them by switching-in redundant units. The BITE will be implemented primarily by means of CMOS ROM's which generate and inject digital test words and monitors them by comparison with the correct test patterns at various points in the system. This implementation was used on the AN/TPQ-37 signal processor, and will be expanded upon here.

Since the BITE itself is subject to failure, redundant BITE circuitry will be incorporated. BITE circuitry failure is tested in two ways. First, incorrect patterns are circulated to determine if the BITE circuitry is capable of detecting faults. Second, when BITE detects a fault in normal operation, the same test will be performed on the parallel and redundant channels. If the BITE continues to find fault with these other channels, it will be deemed that the BITE itself is at fault, and it will be switched out. The redundant BITE will then be energized. Switching simply involves energizing the clocks for the BITE, which, because of its CMOS construction, dissipates very little power in the quiescent mode.

4.5 ZERO-DOPPLER FILTER CLUTTER MAP THRESHOLD

The threshold map provides the reference signals used for setting threshold levels which are used to detect zero-doppler filter signals. The map has a relatively high resolution of one azimuth beam by one elevation beam by a 600-meter range to minimize the visibility loss caused by ground clutter. The data within each cell of the map is a temporal average of the signal returns from that map resolution cell, and is contained in a quasi-logarithmic format to conserve map memory.

The map is initialized at system turn-on, and is regularly updated thereafter. As shown in the block diagram, figure 28, exponential smoothing is used with an 8-sample time constant and an update rate of once per four scans. The time constant and update rate are selected to minimize the effect of targets passing through the resolution cell raising the threshold level, but are responsive enough to follow changing clutter conditions. Map initialization can be speeded by sampling every scan.

82
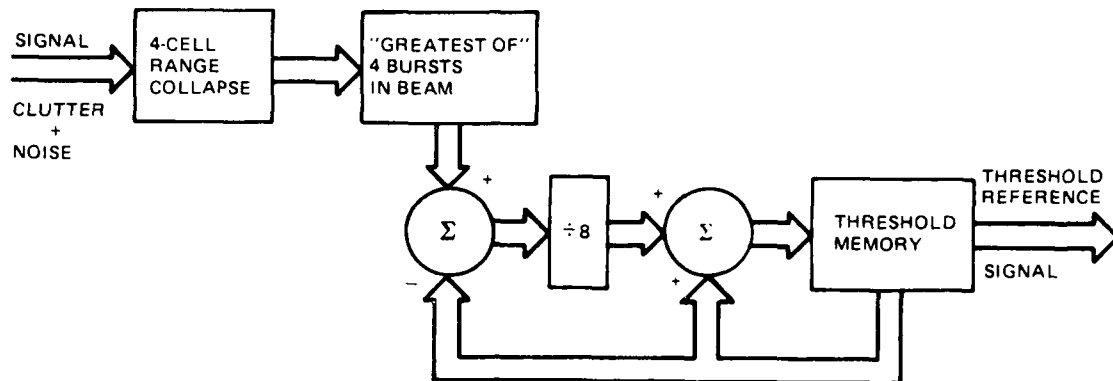
Figure 28. Clutter Threshold Map

The threshold map is the primary means of controlling false alarms from ground clutter returns, while still prividing intra- and supra-clutter visibility. The map is also expected to be of assistance in controlling distributed bird or angel clutter, and weather clutter false alarms. A dynamic range of about 40 dB is adequate to permit detection of the largest expected targets. Clutter exceeding the maximum dynamic range causes the map to censor signals within the covered resolution cell.

4.6 RECEIVER

Three separate receiver channels are used for the three elevation beams. Each channel has an RF preamplifier followed by a redundant receive module which processes the signal to a digital I and Q output. The receiver uses low signal levels throughout to permit the use of monolitic amplifier circuits for low power usage and high reliability.

The first unit in each receive channel is the STC attenuator followed by a low noise (2 dB) preamplifier. The remainder of the receiver consists of the frequency conversion, amplification and filtering, synchronous detector, and A/D converter which provide digital I and Q data to the signal processor. The receiver parameters are listed in table 12.

The STC attenuator is placed at the receiver input to reduce the dynamic range required in the receiver. Additionally, low signal levels, approximately 0 dBm peak, are used in the synchronous detector to lower the required peak IF power level. The voltage into the A/D converters is a 0.1-volt bipolar video which provides a 10-bit output at a 1-MHz rate. Two A/D converters are used to provide digital I and Q outputs.

83

Table 12. Receiver Parameters

Noise Figure	2.0 dB nominal
Bandwidth	1 MHz
Gain (no STC)	59 dB maximum
STC Attenuation Range	17 dB
Dynamic Range	54 dB + 17 dB STC
Image Rejection	30dB
Output	10-bit I, 1×10^6 samples/second
	10-bit Q, 1×10^6 samples/second

Closed loop feedback circuits using digital logic are used to compensate automatically for receiver gain changes and DC drift in the detector, thus maximizing receiver dynamic range and allowing unattended operation for long periods. The low power LSI logic elements used for these circuits, as well as the STC function generator, perform the required function with low power and high reliability. Receiver built-in test circuits will be included in each assembly for on-line tests and receiver self-adjustment. Failure detection and replacement decision will be performed by a separate BITE controller, which will switch a stand-by redundant receiver unit into the circuit. To conserve resources and increase reliability, the stand-by units are not powered.

The use of CMOS for the logic circuitry was considered, but at the operating rates required in the receiver control logic, low-power T^2L logic consumed less power. Additionally, since the other receiver circuits require that the receiver be switched off while in stand-by, the low static power drain of CMOS was not an advantage.

The receiver for one of the elevation beams is illustrated in the radar block diagram, figure 2. The figure shows the receiver assembly circuitry and interconnections with the BITE controller, and the standby switching circuits. Since the baseline radar has three elevation receive beams, the complete receiver group will consist of three linear receiver channels, each with its own standby unit.

The three redundant receiver channels, with the necessary auxiliary BITE and RF preamplifiers, are estimated to be able to fit into a 3 x 6 x 24-inch rack space. The total weight is estimated as 43 pounds, including structure. Total power usage of the receivers is estimated at 28 watts, at current technology, with a reasonable chance of being reduced 11 watts with technology advancement.

4.7 DATA PROCESSOR

The following analysis of requirements further defines the data processor system configuration and the modules within the system. The analysis considered both hardware and software requirements. Results of the analysis showed that a number of processors are available (now on the drawing board), and more will become available as VSLI technology is used. The specific processor need not, and should not, be selected at this time because the multi-processor configuration can be expanded to meet the processing load, and software which is not constrained by the processor selection can be specified.

4.7.1 Analysis of Processing Load

Analysis of the simulation program has resulted in a further refinement of the functions of the baseline radar as originally described in the proposal. These functions are similar to those for the Artillery Locating Radar (ALR), but differ in two respects. First, detection correlation is more involved (more bursts, elevation scan) and, second, tracking is less involved (no ballistics). The ALR program, which used about 40 KOPS and 48K (16-bit words) memory, provides a useful basis from which to approximate the processing requirements for the radar.

The processing load will increase as environment simulation is added and modified to improve the baseline radar.

To save power, the data processor configuration will be polymorphic by accommodating variation in detection load. This characteristic permits postponing selection of specific data processor modules until requirements can be defined in more detail, and can be quantified into units of operations per second and memory size.

At this time, power consumption and reliability are more critical than program size and execution speed. Memory and processing modules can be added to meet these requirements, up to the limit of power and reliability. Reliability can be improved, without increasing power consumption, by adding more processing modules which are not energized until needed as substitutes for failed modules. The tendency for processing modules is toward less power consumption as the scale of circuit integration increases (LSI ——> VLSI).

4.7.2 Analysis of Processing Characteristics

The data processor must (1) accept data from many detections, (2) correlate detection data to combine multiple detections on same targets, and (3) associate new data with current target tracks, extract target parameters from target tracks, and output target data to the communication channel. The types of operations being performed are not sophisticated. The number of detection data sets and target data sets that must be processed and correlated with each other require a processor which can sequence through the same functions for various combinations of data sets. Another processing characteristic is that, as the data are processed, they move from one data file

to another in a fixed sequence. This characteristic is illustrated in figure 29. As shown in this figure, these characteristics lead to a processing sequence which can be segmented into the processing required to move data from one file to the next. Data files are arranged so that the first input to the next file can be processed independent of following data. Processing can thus be allocated to processing modules which operate in parallel to increase throughput of processor configuration.

4.7.3 Other Processor Requirements

In addition to the requirements for processing speed and memory capacity, there are other requirements which are of equal importance. The requirements for high reliability and low power consumption have been discussed above. The data processor must also be adaptable to changes in processing load (variation in number of targets detected/tracked) and to changes in processing ability (availability of data processing resources). To meet this requirement, the modules of data processing resource must be small enough in capacity and power consumption and have high reliability in order to make a multi-processor configuration practical. A data processor configuration which meets the above requirements will have modules which can be de-energized when not needed, will be able to re-configure its modules to accommodate module or software faults, and will have the capacity for increased software reliability by use of a voting policy among multiple processors. The data processor will also be expandable, to the power consumption limit, to meet new processing loads as the radar is optimized.

4.7.4 Special Purpose Processing

Data processing hardware which performs special functions imposed by the radar will be used to increase processing speed and decrease program development time. Examples of this type of function are:

- A high speed correlation processor which can search data files for items which meet multiple criteria such as range + window, elevation + window, bearing + window. This type of processor has been built and tested, and decreases processing time by orders of magnitude.

- Special purpose macro instructions in the processing modules which perform functions which are repeated many times in the processing cycle. Track window size and location computations as well as matrix operations and other processing for the Kalman track filter are other viable applications of this type of processing. The use of VLSI technology should broaden the possibilities for special purpose processing units.

4.7.5 General Purpose Computing Requirements

The data processor will also be required to meet the following requirements:

- High level programming language compatability.
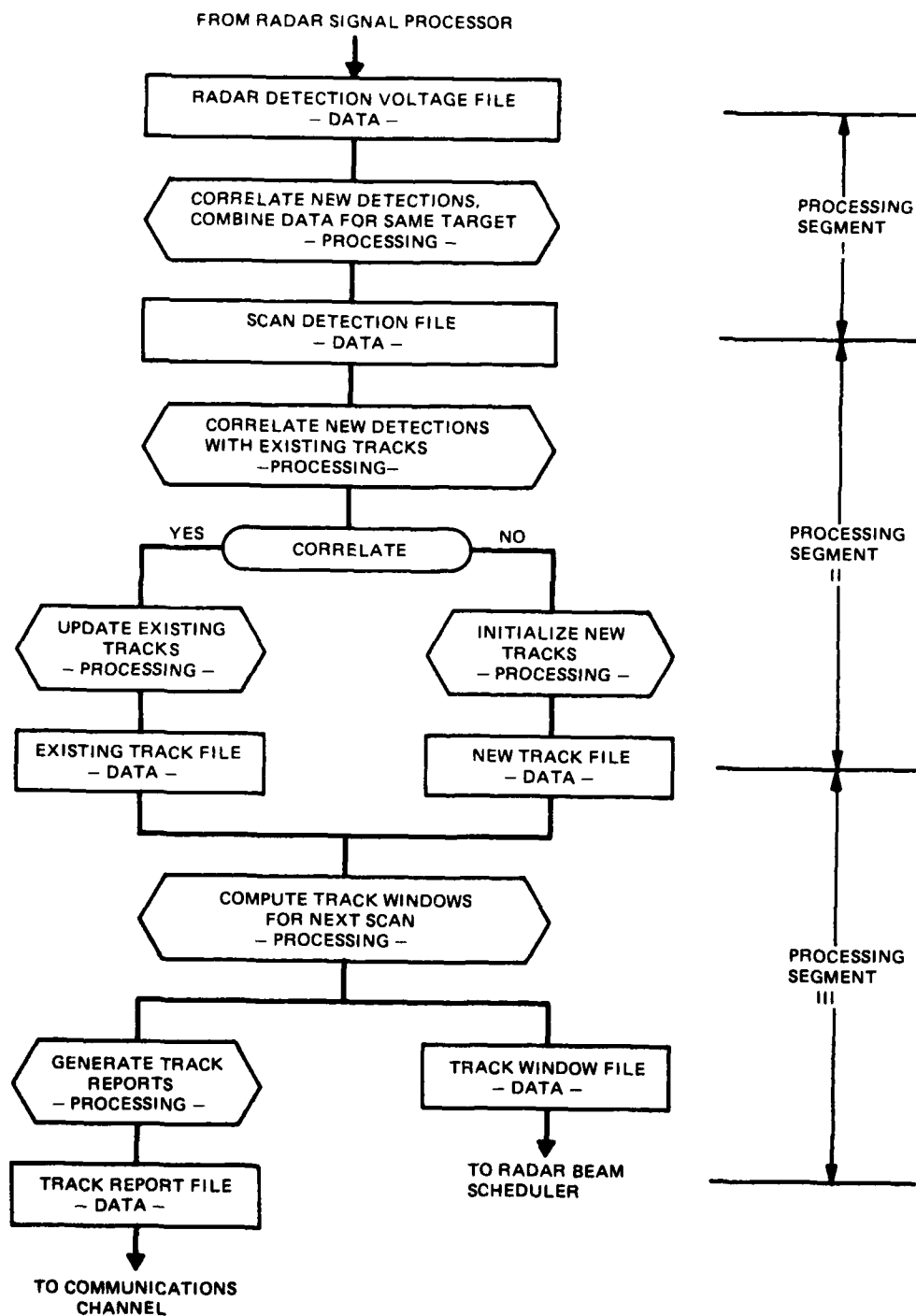
Figure 29.   Data Processing Functional Sequence

87

● Shared memory capability so that functions may be stored in memory which can be accessed and processed by any processing module. This capability also reduces time and power consuming I/O hardware in the module interface.

● Self test/fault detection/fault isolation capability. The availability of this is crucial to a configuration which can be adapted to faults within the data processor.

4.7.6 Candidate Data Processor Configuration and Architectures

The following is a list of multi-processor systems with characteristics and attributes pertinent to the data processor of the baseline radar. Those items of particular interest are labelled with an asterisk. A bibliography of the references reviewed as source material is included. Hardware is under development by Sperry Gyroscope which could be applicable to the data processor for the baseline radar. The primary application of this hardware is for missile use. However, the requirements for high reliability and low power consumption make these developments attractive. The hardware under development will use CMOS/SOS, LSI, and hybrid technologies.

● Cm*, Extensible Multi-processor

    A. Developer and Time Frame

        1. Carnegie-Mellon University
        2. In development for 3 years.

    B. Type of Application Designed for

        1. Experimental
        2. General purpose.

    C. Major Design Objectives

        1. Close cooperation between large numbers of concurrently executing processes.*
        2. Shared memory for data communication
        3. Switching structure which provides efficient, expandable access to memory.

    D. Type of Structure

        1. Hierarchical*
        2. Extensible
        3. Large number of processors
        4. Not oriented to specific application.

    E. Scale of System

        1. Pilot System − 10 processors
        2. Next stage − 50 processors
        3. Full scale − up to 10,000 processors.

F.   Special Support Software - Hydra, Special Operating System

G.   Processor Type/Manufacturer

    1.   LSI-11 processor (16-bit)
    2.   Digital Equipment Corporation
    3.   140 KOPS.

● Fault-Tolerant Building-Block Computer

A.   Developer and Time Frame

    1.   Jet Propulsion Lab. for Naval Ocean Systems Center
    2.   Probably within last year.

B.   Type of Application Designed for

    1.   General data processors, variety of applications
    2.   High reliability, complex military system*.

C.   Major Design Objectives*

    1.   Systems which are sufficiently reliable that they do not require technician or logistic support for the life of their mission.

    2.   A highly reliable core computer which can significantly aid in the diagnosis and maintenance of an entire system.

D.   Type of Structure

    1.   Self-Checking Computer Module (SCCM) consisting of:

        a.   An error detecting (and correcting) memory interface
        b.   A programmable bus interface
        c.   A core building block
        d.   An I/O building block
        e.   Two commerical microprocessors and commercial memory.

    2.   SCCMs connected to each other by way of Mil Std 1553A bus.

E.   Scale of System

    1.   Single computer applications with standby redundancy
    2.   Distributed computer networks*.

F.   Special Support Software

Not considered.

G.   Processor Type/Manufacturer

Not selected.

- **A Fault Tolerant Multi-processor Architecture for Aircraft**

    A. Developer and Time Frame

    Draper Lab 1975/76

    B. Type of Application Designed for

    Commerical aircraft, 10-hour flight durations.

    C. Major Design Objectives

    Failure rate of 10^{-10} failures per hour.

    D. Type of Structure

        1. Parallel-hybrid redundant
        2. Buses for memory and interface access are redundant
        3. Triad grouping of modules and buses*.

    E. Scale of System*

        1. 10 to 20 processors
        2. Memory 16K to 64K words
        3. Throughput 1.1 to 3.1 MOPS.

    F. Special Support Software

    Multi-processor executive, compiler.

    G. Processor Type/Manufacturer

    National Semiconductor IMP-16.

- **Computing With Multiple Microprocessor**

    A. Developer and Time Frame

    Stanford University, SLAC/1973.

    B. Type of Application

    Study of asynchronous processors.

    C. Major Design Objectives

    Develop model for tradeoff at cost versus throughput.

    D. Type of Structure

    Common data bus connects processor with each other.

E.   Scale of System

Small - sort and matrix multiply only routines coded.

F.   Special Support Software

None - simulation only.

G.   Processor Type/Manufacturer

None - simulation only.

● <u>Bibliography</u>

1.   J.V. Levy, "Computing With Multiple Microprocessor", Ph. D. Dissertation, Stanford Univeristy, April 1973 (NTIS SLAC-161).

2.   D.A. Rennels, "Fault-Tolerant Building-Block Computer Study", JPL Publication, Jet Propulsion Laboratory, July 1978 (NTIS N78-30835).

3.   W.A. Wulf and S.P. Harbison, "Reflections in a Pool of Processors", Carnegie-Mellon University, February 1978 (NTIS AD A055935).

4.   L. Raskin, "Performance Evaluation of Multiple Processor Systems", Carnegie-Mellon University, August 1978 (NTIS AD A060495).

5.   R.J. Swan, "The Switching Structure and Addressing Architecture of an Extensible Multiprocessor: Cm*", Carnegie-Mellon University, August 1978 (NTIS AD A060494).

6.   G.W. Brezina, "Fourth Generation Computer Architectures", Air Force Weapons Laboratory Final Report, January 1978 (NTIS AD A060670).

7.   F.G. Thourot, "Design of the Processor for Software Compatible Avionics Computer Family" M.S. Thesis, Air Force Inst. of Technology, December 1977 (NTIS AD A053345).

8.   Aerospace Corporation, "Fault-Tolerant Software Study", NASA Final Report, February 1978 (NTIS N78-18797).

4.7.7 <u>Candidate Processor Modules</u>

Table 13 indicates the type of processor modules that are available, or are in the process of hardware development. The purpose of the table is to show the spread of characteristics available. The data processor for the baseline radar could be composed of modules of one type or a combination thereof.

Table 13. Characteristics of Available Processor Modules

Processor Type	Power Dissipated	MTBF	Macro Available	Shared Memory	Self-Test	Capacity (KOPS)	Development Status
UYK-502	300	—	Yes	Yes	Yes	250	Production
SP2000	130	—	Yes	Yes	Yes	500	Prototype
U1621S	25	—	Yes	Yes	Yes	500	Design

4.7.8 Software Configuration Alternatives

The data processor program architecture should take advantage of the pre-
viously described characteristics. In addition, the architecture should be
adaptable for growth and changes in function as the radar advances from its
baseline configuration. The combination of hardware and software architec-
tures should provide a data processor which can increase/decrease its comput-
ing capacity as a function of the processing load. They should also provide
for re-assignment of module functions as faults occur within the modules. As
shown in figure 30, the manner in which the processing load is distributed
and segmented between multiple processors provides increased adaptability and
reduces required processor capacity.

4.8 POWER SUPPLY

Table 14 lists the different voltage levels and load currents required
for the major subsystems of the radar. The DC output regulation will be ± 1
percent, and the output ripple will vary with the particular subsystem, i.e.,
a variation of 1 mv p-p for part of the synthesizer to 100 mv p-p for the
transmitter.

To obtain high efficiency with a minimum size, it will be necessary to
utilize a single input transformer with multiple secondaries. This will re-
duce the total magnetizing current drawn from the input lines, because one
large core will be magnetized as compared to many smaller units. Also, the
efficiency of one large transformer is greater than many smaller units. In-
cluded with the transformer will be the required rectifiers and filters which
will make up the transformer rectifier assembly. Using this approach allows
the DC-to-DC regulators to be located in each major unit. This approach is
advisable to reduce voltage line drops resulting from distribution of high
current loads to some subsystems. Another advantage of the central trans-
former-rectifier assembly is that the output filtering can be sized in ac-
cordance with each individual subsystem requirement.

Referring to table 14, the signal processor, data processor, beam steer-
ing unit, and transmitter are the units that require high DC power. There-
fore, they will be switching-type regulators making use of the higher

92

● SEQUENTIAL PROCESSING IN SINGLE PROCESSOR

	SIGNAL PROCESSING OF BEAM N	INPUT TO DP	OUTPUT TO DP	SIGNAL PROCESSING OF BEAM N + 1	

SEGMENT I	SEGMENT II	SEGMENT III	SEGMENT I	SEGMENT II	
DATA PROCESSING OF BEAM N -1			DATA PROCESSING OF BEAM N		

|← T →|
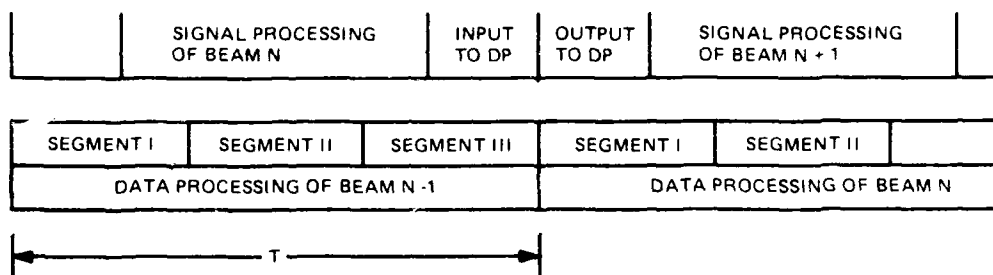
SINGLE DATA PROCESSOR MUST PERFORM ALL OF SEGMENT I, II, AND III PROCESSING IN TIME T BEFORE NEXT DATA FROM SIGNAL PROCESSOR IS INPUT. DATA PROCESSOR MUST BE FAST ENOUGH TO HANDLE WORST CASE LOAD IN TIME T.

● SEQUENTIAL PROCESSING IN 3 PROCESSORS

	SIGNAL PROCESSING OF BEAM N	INPUT TO DP	OUTPUT TO DP	SIGNAL PROCESSING OF BEAM N + 1	

DP 1 | SEGMENT I | | SEGMENT I |

DP 2 | SEGMENT II | | SEGMENT II |

DP 3 | SEGMENT III | | SEGMENT III |
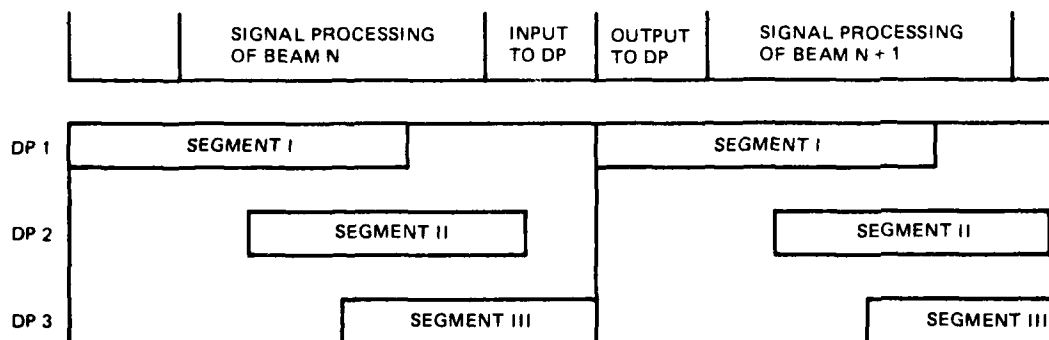
ADVANTAGES

● MORE TIME TO PERFORM EACH TASK, LESS CAPACITY REQUIRED IN EACH DATA PROCESSOR.

● PROCESSING OF EACH SEGMENT CAN BE SPREAD OVER SEVERAL T INTERVALS TO MAKE BETTER DECISIONS (CORRELATIONS) BASED ON DATA FROM SEVERAL BEAMS.

● EACH PROCESSOR HAS IDLE TIME FOR OTHER PROCESSING OR FOR EXPANDED PROCESSING OF DETECTION DATA.

● GREATER POTENTIAL FOR ADAPTING PROCESSING TO CHANGES IN OPERATION OF RADAR. FOR EXAMPLE, EACH PROCESSOR COULD PERFORM PARTS OF SEGMENT I PROCESSING FOR DIFFERENT ELEVATION SCANS. OUTPUTS WOULD THEN BE CORRELATED IN BEARING & RANGE.

Figure 30.   Data Processing Timing Sequence

93

Table 14. Power Supply Voltages vs Load Current (in Amperes)

Power Supply Voltage (Volts)	-13	+5	-5	+8	+15	-15	+28	-10	+100
Signal Processor		6		12					
Beam Steering Unit	50			0.125					0.02
Receiver				0.6	2				
Synthesizer		0.6	0.6		0.2	0.1	0.85		
Transmitter							23		
BITE/FLOC		2							
I/O		5							
Data Processor		13			1			5	

efficiencies of switching units. The low ripple requirements occur in the frequency synthesizer and the receiver. For these units, linear-type regulators will be employed. The advantage of using linear regulators for low ripple output is that the regulator loop can be utilized in ripple reduction, thereby reducing the size of the rectifier-filter.

The difference in efficiency between linear and switching type regulators, up to output voltages of 15 volts, is in the range of 15-20 percent. The +5-volt and -5-volt supplies for the synthesizer must each supply 0.6 ampere, or 3 watts each. The +3-volt supply for the beam steering unit must supply 50 amperes, or 150 watts. Saving 20 percent in efficiency for the beam steering unit will yield 30 watts, whereas a 20 percent saving in the synthesizer will yield only 1.2 watts (0.6 watt per supply). The use of the lower efficiency linear regulator is therefore reasonable for the low power, low ripple applications.

The low power linear power supplies will be integrated regulator chips (typically, Motorola LM series). These units will be "off-the-shelf", and will be very cost-effective. The 10-watt unit will be in a TO-3 case size and, for redundancy, two units will operate in parallel, with either unit able to supply full load current.

The high power units will be of the switching regulator type and will have to be new designs. There will be an allowance made in the design for redundant master/slave operation, with each unit having the capability of supplying full load. The total input power required for the power supplies is 2200 va. This is based on a worst case power factor of 0.8 lead or lag.

Section 5

COMPUTER SIMULATION

5.1 INTRODUCTION

Two radar simulation programs have been prepared to model the baseline radar. The first program is a detailed pulse-by-pulse simulation of the radar, and is used to evalute the operating characteristics of the radar. Due to the computational burden required for this model, this program is used for relatively short radar simulations, generally less than a sector of a scan, or for specific functional evaluation of radar detection parameters.

The second program incorporates a functional simulation of the radar and is used for testing and evaluating the radar algorithms. The radar functional relationships used in this program are obtained by exercising the first program. The second program is designed for simulations of engagements that require modeling over a large number of scans such as evaluation of tracking and reporting algorithms.

Both programs are presently operational for a clear environment using homogeneous ground clutter and precipitation.

5.2 PULSE-TO-PULSE MODEL

5.2.1 Model Overview

This program is designed to generate and sum vectorially, on a pulse-to-pulse basis, the radar responses due to target, clutter, and receiver noise. The radar model uses a step scan phased array in the azimuthal plane and three separate elevation beams. The individual pulses are modeled with a linear FM chirp waveform, and are transmitted in groups for doppler filter processing. The synthesized received signal is processed by an STC circuit, doppler filter bank, pulse compression filter, and detector circuit. All radar parameters, such as operating frequencies, PRF, antenna elevation pointing angles, beamwidths, and waveforms are programmable.

The simulation is event driven. The main routine steps from each detection event to the next detection event with proper allowance for the pulse compression waveform. The detection events are determined by the intercept time of the radar scan with the target or clutter sources. The main program may also be stepped from range cell to range cell on each azimuth beam position to update the clutter maps. In addition, multi-iterations at fixed beam positions are obtainable for Monte Carlo simulation of detection statistics.

5.2.2 Model Implementation

The pulse-to-pulse simulation model is implemented using a main routine which may be divided into two general sections - namely, initialization and calculations. During initialization, the program calculates the values for a number of tables which are stored in arrays for future reference during execution of the calculations. In the calculation section, the main program controls the sequence of the calculations and performs the required calculations. Interpolation from the precalculated tables are used, where possible, thus avoiding many redundant calculations, and improving the operational running time.

The following discussion will highlight some of the major features of the program.

5.2.2.1 Initialization. During initialization, the main program executes the following functions:

o Reads input data

o Initializes program constants

o Calculates receiver noise voltages

o Calculates antenna gain arrays

o Evaluates power spectral densities

o Convolves ground clutter with antenna patterns

o Computes pulse compression filter weights

o Initializes the clutter map

o Initializes the target state vector

o Calculates initial intercept times.

Coordinates - The origin of the coordinate system in the simulation program is located at the antenna. The X and Y axis are in the horizontal plane, and azimuthal angles are measured counterclockwise from the X axis. Elevation angles are measured from the X-Y plane. The azimuth coverage, subdivided into 120 steps corresponding to the steps of scanned array, is illustrated in figure 31. The elevation angle is quantized into 100 steps from -0.10 radian to +0.90 radian in 10 milliradian steps, and is illustrated in figure 32.

Antenna Gain - Antenna gain is modeled as the product of an azimuth pattern and an elevation pattern for the two-way gain. The azimuth pattern is normalized to peak gain, while the elevation pattern is the actual gain in the direction of the azimuth peak. The azimuth pattern gain is precalculated during initialization using 1/8 the step size of the scanned array. There
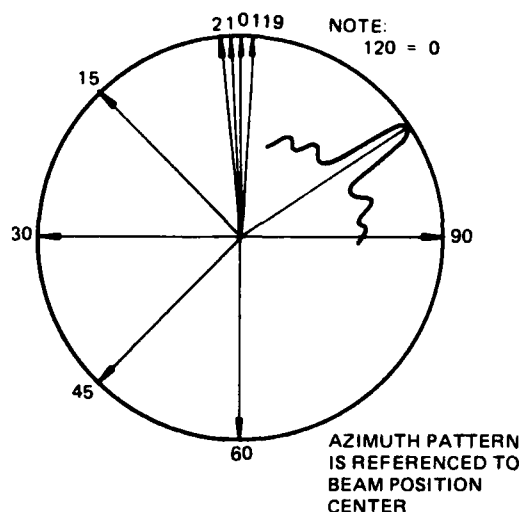
96

Figure 31. Azimuth Beam
Positions
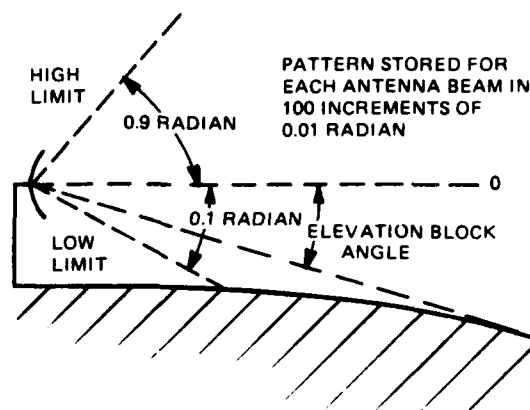
Figure 32. Elevation Pattern
Geometry

are approximately 8 data points across the 3 dB beamwidth of the azimuth pattern which allows use of a simple interpolation formula to find the azimuth gain appropriate at any angle within the pattern. The azimuth array extends over 32 points on either side of the peak to account for the first four sidelobes of the antenna pattern. A modified sin (x)/x model* was used to calculate the points for the pattern arrays, with the peak sidelobe level being selectable. A peak sidelobe level of 25 dB was used for the simulations. An azimuth antenna pattern obtained from the simulation is shown in figure 33.
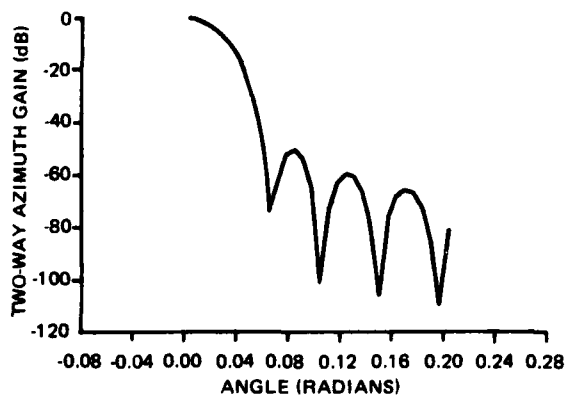
Figure 33. Azimuth Two-way Gain

The elevation pattern is likewise precalculated and stored in arrays, one for each beam. The limits of simulation and increment sizes is indicated in figure 32. Since the radar transmits on all three beams simultaneously, the composite transmit beam is distinctly different from the individual receive beams. The transmit pattern is calculated by summing the contributions from each of the elevation beams, taking into account the relative beam power and the phasing of the excitation.

Terrain Characteristics - The simulation is designed to accommodate specific terrain data specified with X, Y coordinates, and to transform it

- - - - - - -

*Skolnick, Introduction to Radar Systems, 328.

97

into a radar oriented file in R and θ coordinates. The initial terrain input file may include terrain elevation, terrain type, cross sectional spectral density characteristics, and other useful features. The ultimate output of the initialization section is a terrain file containing a mean ground clutter cross section, an amplitude distribution type, and a power spectrum type for each azimuth-range cell of the radar.

The terrain subroutines are written to allow programming the units of the input file and output samples at submultiples of the beam spacing and range increments. The transformed data samples are available at 1/8 the azimuth beam spacing and 1/2 the range resolution. There are 960 azimuth increments and 750 range increments in the X, Y plane. The azimuthal increment spacing was selected to reduce the error due to sampling in the sidelobe region to a value less than 2 percent for possible use of the simulator to compare different antenna pattern sidelobe performances. The range increment spacing was selected to permit range spatial correlation. For example, the cross section for radar cell (m, n) denoted by $\sigma_{(m, n)}$, may be obtained by weight averaging the cross section values assigned to three map cells, the one preceding, the one following, and the one at the radar cell. The center of this coordinate system for the radar site may be programmed to any position within the X, Y plane, provided there is sufficient data in the input file to include the 60 nmi range of the radar.

The sampled height data file is transformed using an opposite area interpolation method, figure 34. Given the four closest data points in cartesian coordinates, the height values to be assigned to the point X in the R, θ system is obtained by

$$Z(R,\theta) = \sum_{n=1}^{4} W_n Z_n (X, Y)$$

where W_n is the fractional area of the opposite corner.
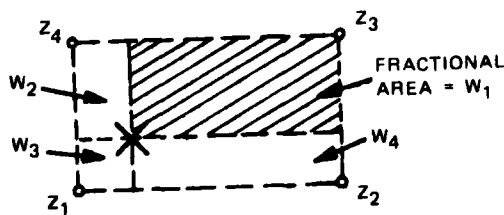
Figure 34. Opposite Area Interpolation Diagram

For discrete data, such as the type of terrain, a data point in R,θ is assigned the value of the nearest point in the X, Y system. The nearest point is obtained by comparing the fractional area weighting factors.

After transformation, each beam position is examined to define shadow points. An effective earth model is used to account for ray bending. The fractional model, normally taken as a 4/3 earth model, is programmable. The mean radar cross section per unit area for each data point is obtained

98

from a programmable data array. The entry point to this array is obtained from the type of terrain and the incident angle. Thus the radar cross section per unit area may be programmed for different terrain types and as a function of angle as obtained from the literature, e.g., Nathanson, etc. The outputs from these transformations may be stored on a file for future simulations using the same radar site.

At the present time, the ground clutter is simulated by assuming a uniform homogenous terrain for a 4/3 earth model. The convolution of the antenna pattern with the ground clutter is done during initilization to obtain the value of the mean radar cross section assigned to each radar range cell at each beam position. Using the homogeneous ground clutter model, the convolution process is only required for all range cells at a single azimuth beam. The stored values resulting from this convolution are used to specify the mean value of the clutter at each azimuth range cell.

The power spectral density and the amplitude distribution function for each clutter cell may be independently selected by the terrain data map. This selection is accomplished by the assignment of pointers which designate the functional form of the spectral density and the type of amplitude distribution. For example, a point value of 3 for the amplitude distribution would designate a Weibull distribution when evaluating the amplitude of the response. Similarly, a spectral density pointer is used to select the appropriate equation when evaluating the sample values of the spectral density function. Since evaluation of the spectral density function may be required for each clutter cell, this evaluation is performed once during initialization for each type of clutter and stored in an array. During execution of the calculation, the pointer serves as an index to the spectral density array.

Target Characteristics - The simulation program has been designed to input from 1 to 30 threat targets. Identification of the targets is established by the order of entry during initialization. Each target entry includes a radar cross section scale, cross section fluctuation type, and a type identification pointer which designates the type of target - for example, a sphere, bomber, or missile. The type pointer is used during response evaluation to select the table of normalized radar cross section versus aspect angle for that particular target. These tables are programmed in 10-degree steps from 0 to 180 degrees. Normalized mean cross section versus aspect currently programmed for the bomber is shown in figure 35.

The present simulation program contains built-in trajectory programs for constant altitude, constant velocity trajectories for both radial and offset courses relative to the radar. The initialization inputs required are the X,Y coordinates, altitude, velocity, and time of initialization. During initialization, a state vector containing position, velocity, and acceleration (in cartesian coordinates and time) is calculated for each target. Initialization is completed by rearranging the order of the target array in ascending order of intercept with the azimuth search pattern of the radar.

99
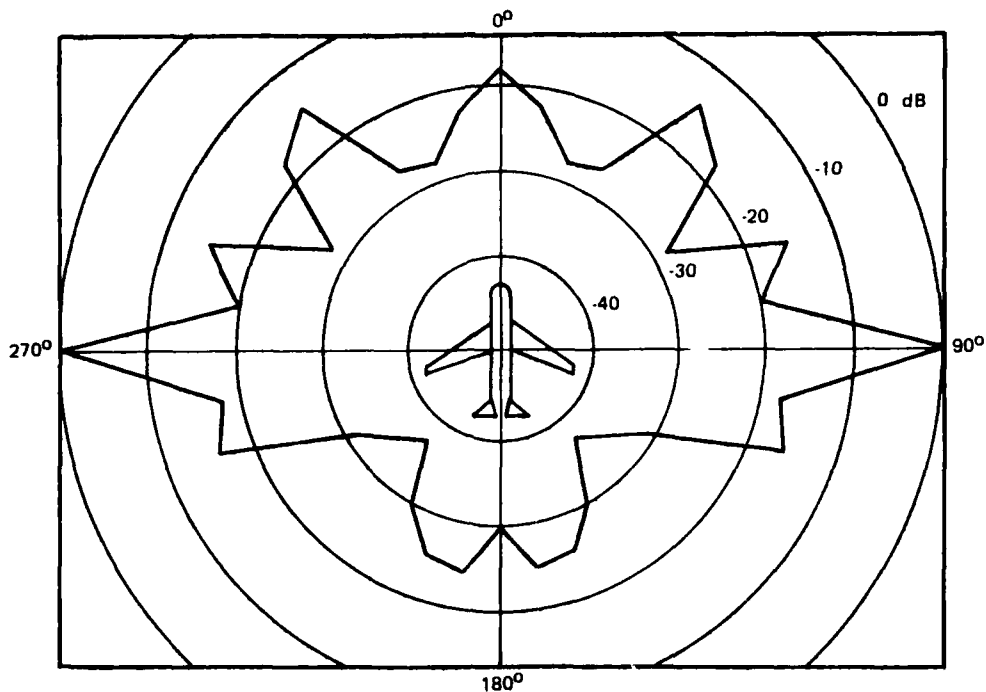
Figure 35. Normalized Radar Cross Section for Bomber

5.2.2.2 Calculations. The basic calculation sequence executed by the pulse-to-pulse simulation program is:

o Select first target intercept and update scan parameters

o Select first pulse burst

o Select first range cell for target calculations

o Select first antenna elevation beam

o Perform calculations for selected parameters

o Repeat calculations above for additional elevation beams

o Repeat calculations above for remaining range cells

o Select prf and frequency for next burst

o Repeat all calculations for each of 4 bursts

o Determine time of next beam intercept for this target

o Insert this target in time-ordered target array

o Repeat complete sequence for next target intercept.

100

The calculations performed for each selected set of parameters are:

- Calculate ground clutter signal voltage

- Add target signal voltage to clutter voltage

- Add weather clutter signal voltage

- Apply transmitter pulse compression coding and store resulting wave-form

- Apply STC control function

- Add receiver noise voltage

- Apply doppler filter processing

- Hard-limit non-zero doppler channel outputs

- Apply receiver pulse compression processing

- Compare output voltage of each doppler channel with correspoding threshold voltage.

Test of Simulation Clutter Models - The results of testing on the genera-tion of correlated Weibull clutter signals are given for three values of spread parameter (a) in figures 36, 37 and 38. Similar curves with other values of a are available. The ordinate of these graphs is the natural log of the reciprocal of probability of exceeding a threshold, and the abscissa is the normalized threshold. (See Appendix E for Weibull distribution.) The ideal cumulative distribution for Weibull clutter would plot as a straight line using these coordinates. Data points were obtained using 40 threshold bins and accumulating the first pulse of 2000 sample groups. As is evident in these figures, the generated distribution approaches the ideal Weibull distribution at large threshold values. The probability of exceeding a threshold of 0.707 for a equal to 1 is 37 percent from the ideal curve and 41 percent from the generated samples. Typical normalized threshold values should be greater than 3.5; hence, the deviation at these higher threshold value is not significant in the simulation. A simplified explanation of why the distribution follows the ideal distribution at higher values of threshold and not at lower values is as follows: The method being used to generate the correlated sample signals is the same as the method given by R. L. Mitchell in "Radar Signal Simulation", Chapter 8, page 114. The signal samples are ob-tained from the discrete Fourier transform of weighted samples of the square root of the power spectrum and is given by Mitchell as

$$x_k = \sum_{n=0}^{N_r-1} \hat{X}_n \exp(j2\pi kn/N_r) \qquad K=0...N_r-1$$
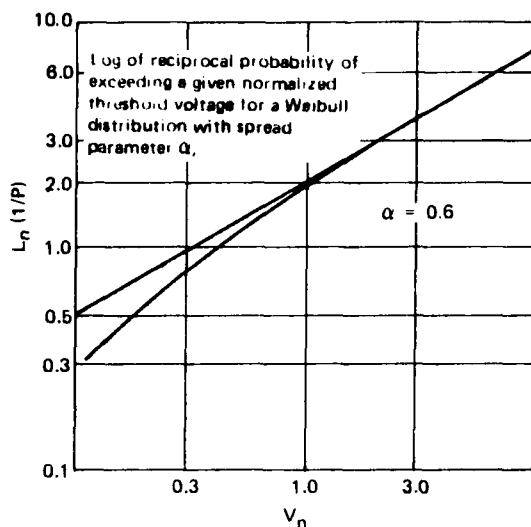
Figure 36. Test of Correlated Weibull Distribution, $a = 0.6$

where the $\hat{X}_n$ are the weighted samples of the spectrum. Since the power spectrum for the clutter is heavily weighted near zero frequency, the distribution is dominated by this sample. Thus, the generated signal consists of the sum of a large zero frequency signal and a number of smaller signals where all signals have the Weibull distribution. When the zero frequency signal is large, the amplitude of the composite signal x_k essentially follows the amplitude of the zero frequency signal which is Weibull distributed. When the amplitude of the zero frequency signal is small, the amplitude of the composite signal follows the distribution of the sum of nearly equal Weibull distributed variables which does not give a composite Weibull distribution.

Figure 37. Test of Correlated Weibull Distribution, $a = 1.0$
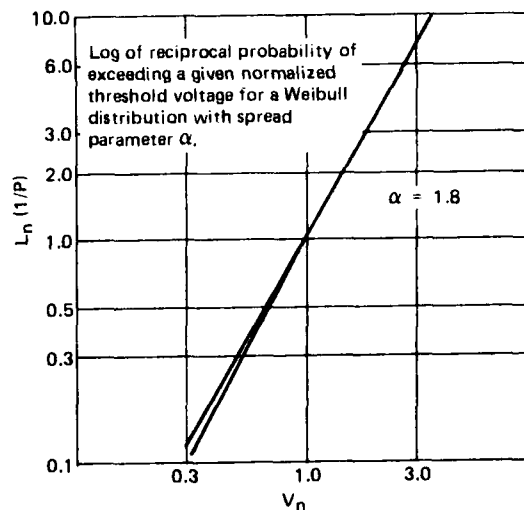
Figure 38. Test of Correlated Weibull Distrubution, $a = 1.8$

Verification of this rationale was tested by reducing the number of samples of the power spectrum from 7 to 3 and changing normalized power spectrum sample spacing to 0.75. This change places more power in the zero frequency sample and less in the remaining samples. A comparison of the distribution obtained is given in figure 39 for a equal to 1. The deviation from Weibull at a threshold level of 0.7 was reduced by a factor of approximately 2.
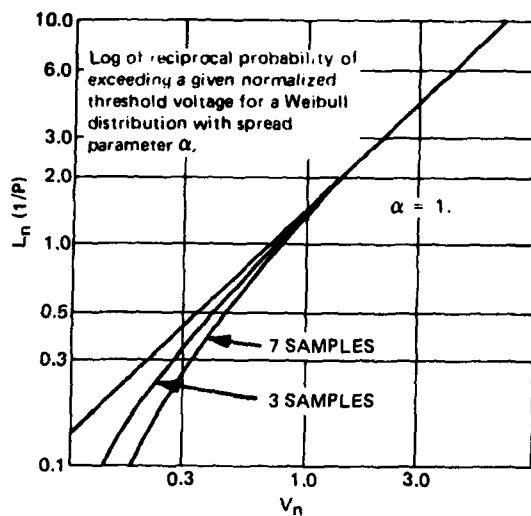
Figure 39. Comparison of 7 and 3
Spectrum Samples for Correlated
Weibull Distribution

Pulse Compression Simulation -
The pulse compression waveform
implemented in this simulation is done
in discrete phase steps since target
returns are processed only at discrete
range increments (as will the sig-
nal processor). To illustrate the
sidelobe levels, the ambiguity func-
tion for a discrete phase code using
the equivalent linear FM phase shifts
of the baseline radar was programmed.
A graph of the results for the first
quadrant is shown in figure 40. In
this diagram, each doppler slice is
offset by 50 Hz, and the total doppler
region is approximately 2.5 kHz. The
time displacement data were obtained
using 320 increments at 0.1 times the
bit time of 2 microseconds.
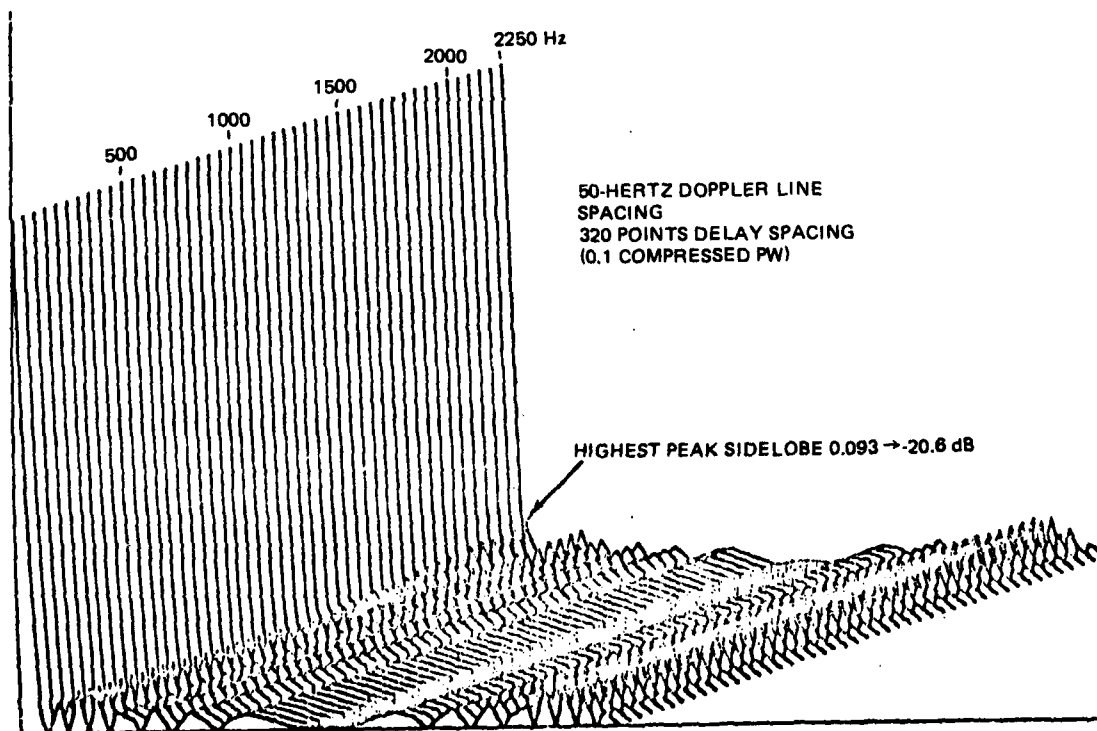
Figure 40. Ambiguity Diagram for Simulated PC Waveform

103

Clutter Map Simulation -Three clutter maps, one for each antenna beam, are updated using a 7/8 old plus 1/8 new data law. The range resolution of the clutter map is equal to twice the radar range resolution. Since these clutter maps are used to establish detection thresholds, they are initialized during the initialization segment of the program. Early in the simulation study, initialization was accomplished by repeating each range sweep 22 times. The repetition number was selected to bring the initial clutter map voltage from 0 to a value within 0.6 dB of the value it would attain if it repeated the updating procedure for an infinitely long period. The 0.6 dB level was chosen equal to the quantatization step size used in the baseline radar. This procedure required considerable computer time. Hence, the procedure was modified to reduce the operating time requirement. During initialization, the clutter maps are obtained by simply averaging 15 samples of the voltage response obtained at each range cell for the specified distribution at that cell.

5.3 RESULTS FROM PULSE-TO-PULSE SIMULATION PROGRAM

The computer storage and operating time required to exercise the pulse-to-pulse simulation prohibits the use of this radar model when evaluating tracking algorithms. Thus, the main purpose of this model is to obtain functional relationships which will accurately predict the output voltages of the radar as a function of the scenarios and target kinematics. The functional relationships obtained from this model are used to model the radar in the simulation program of the tracking algorithm. Some of the more important results are discussed below.

5.3.1 Threshold Crossings for Non-Zero-Doppler Channels

The simulation program was exercised to obtain 100 Monte Carlo runs at a single beam position with target absent. The output voltage for each doppler channel and each range cell was recorded for each pulse burst. Using 4 pulse bursts for each run gave 400 samples for each range cell. Histograms were prepared and processed to obtain an expression for the probability of threshold crossings. This probability for non-zero doppler channels is given by

$$P \ (V > V_t) = \exp \ (- V_t^2/32)$$

The individual range cells for all non-zero-doppler channels had excellent fit to the same curve. Hence, those range cells which included only receiver noise and no STC effects were combined to obtain a histogram using 53,000 samples to test the higher tails. Again, excellent agreement was obtained. A number of range cells containing both receiver noise and ground clutter were examined to determine if ground clutter affected the threshold distribution for non-zero-doppler channels. The presence of ground clutter could not be detected in the output data for these range cells. In particular, the range cell at 10.5 kilometers, which should contain close to the maximum value of ground clutter, did not show any departure from the probability of detection equation given above. It is therefore concluded that this equation could be used to determine the probability of false alarm versus threshold voltage (V_t) for all non-zero-doppler filter channels.

5.3.2 Thresholds for Zero-Doppler Channels

A similar procedure was performed for the zero-doppler channel. Histograms were generated for all range cells containing ground clutter (range cells 33 thru 75 in this simulation model). The ground clutter was generated from a Weibull distribution with a mean radar cross section of 9.73×10^{-3} and an a parameter for the voltage distribution of 1.22 which are typical values for a muskegs region.

The probability of threshold crossing was fitted to a function given by

$$P \ (V > V_t) = \exp \ [\ -(\rho V_t)^a \ ]$$

The value of a obtained from the histograms of the output voltages for each range cell is shown in figure 41. These a's were obtained using only 400 samples for each range cell. Although some dispersion is anticipated, the trend is clearly evident. Both an exponential and a linear line were mean square fit with only minor differences.

For range cell 33, the value of a obtained from the fitted line is 1.73; at range cell 75, the value is 1.42. This departure from the 1.22 value used to generate the clutter is believed to be due to the summation of the range sidelobe contributions with pulse compression. At the close-in range, for example range cell 33, contributions from range cell 3 through 32 add to the signal at cell 33 by the range sidelobe structure of the pulse compression waveforms thus modifying the shape of the distribution at the receiver output. This addition changes the a parameter closer to the value of 2 expected for the summation of many independent samples of comparable amplitude. At the other limit of range cell 75, the ratio of the amplitude of self-clutter due to range sidelobes to the clutter amplitude is less, and the departure from the value of 1.22 is less.
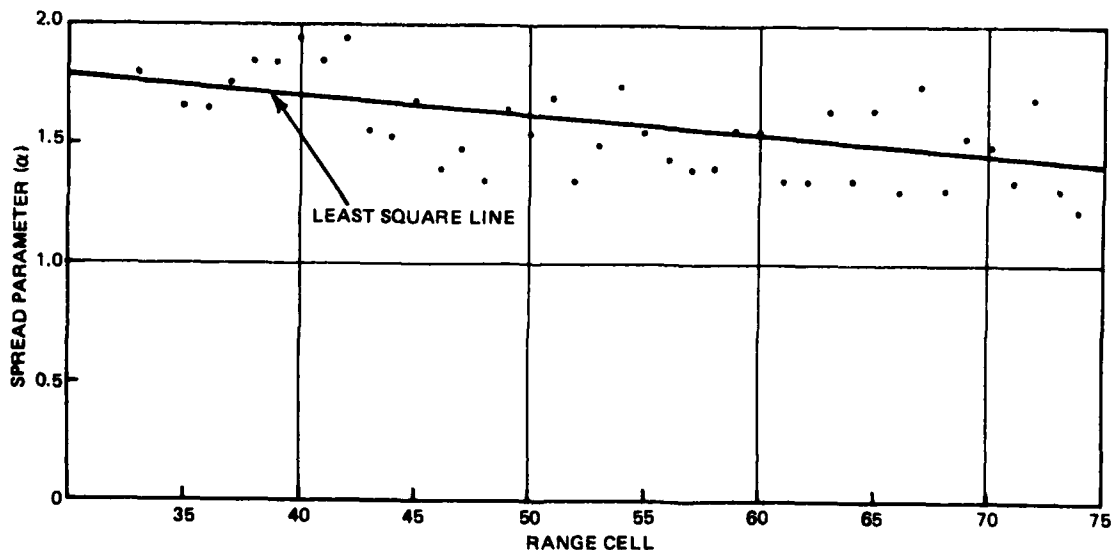
Figure 41. Variation of Weibull Spread Parameter (a) Versus Range Cell

105

To test this assumption further, a test was conducted using Weibull clutter and Rayleigh noise. The clutter signal was generated using a Weibull distributed amplitude and uniform phase distribution. The noise signal, which had a Rayleigh amplitude and uniform phase, was added to the clutter. The clutter-to-noise power ratio was set at 1.61 which corresponds to the ratio of clutter signal-to-clutter noise for a 20 dB range sidelobe level in uniform clutter. The a parameter of the input clutter signal was varied from 1.2 to 2.

Using Monte Carlo and least-square techniques, a Weibull distribution with parameters (a_s, P_s) was fitted to the voltage magnitude of the sum signal with correlation coefficients greater than 0.98. The a parameter of the output sum signal is given in figure 42 as a function of the input parameter.

The ambiguity function of the pulse compression waveform illustrated in figure 41 assumes uniform amplitude of the return signal. However, at extremely close ranges, the return varies as a function of range, and is not completely compensated by the STC action due to the length of the transmitted pulse. That is, the signal from the start of the received pulse is attenuated differently than the signal at the end of the pulse, although the source of the returned signal remains constant. This effect modifies the sidelobe structure of the pulse compression waveform as a function of range.

The results of these experiments indicate that the probability of threshold crossing in the zero-doppler channel for Weibull clutter may be obtained

Figure 42. Alpha Sum Versus Alpha Clutter

106

using a Weibull output voltage distribution function. The a parameter for the output voltage is obtained by compensating the input a parameter for range sidelobes and adding a correction factor as a function of range. When using a single type of clutter, the a parameter of the output is obtained directly from the pulse-to-pulse simulation results as given above.

5.3.3 Detection Probabilities for Non-Zero-Doppler Channels

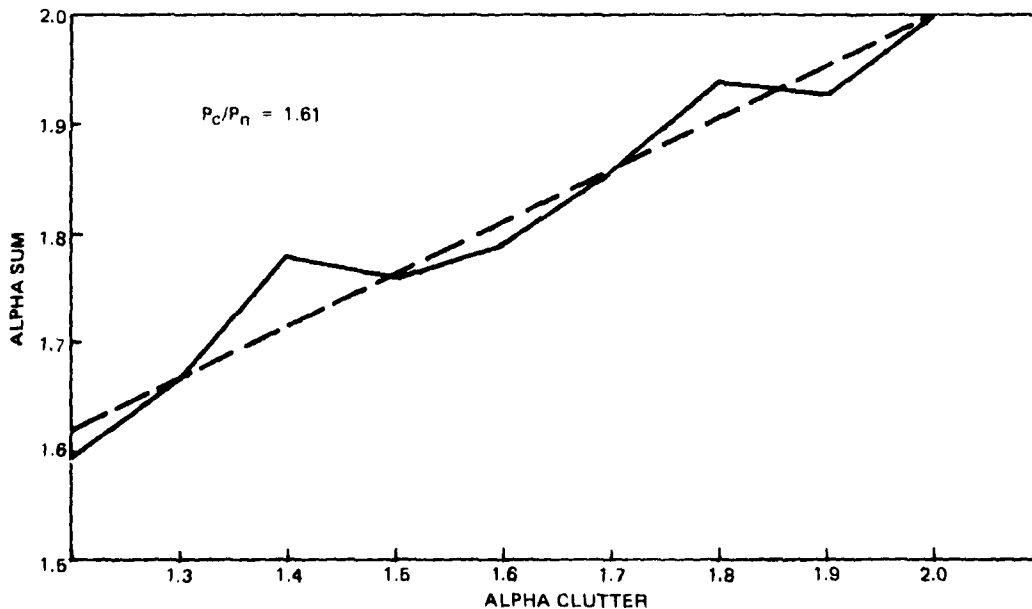The simulation program was run in a Monte Carlo mode for a target at selected fixed range cells using seven values for average signal-to-noise ratio. At each signal-to-noise ratio, 400 data samples were obtained to process a histogram of the output voltage. The histogram data at each ratio was fitted to a function given by

$$P (V > V_t) = exp [- (\rho V_t)^a]$$

The correlation coefficients for these fits were better than 0.988. The values for ρ and a as a function of signal-to-noise ratio (dB) are shown in figure 43. Values obtained from this graph are used to predict the probability of detection for a target with receiver noise as a function of threshold voltage and signal-to-noise ratio.

5.3.4 Detection Probabilities for Zero-Doppler Channel

The probability distribution of the voltage V_s received by the zero-doppler filter was also obtained using Monte Carlo and least squares techniques. The received signal V_s was the sum of target signal, clutter signal, and noise. The target signal had a constant amplitude with uniformly distributed phase. The clutter signal had a Weibull distributed amplitude (a,ρ) and a uniformly distributed phase. The noise was Rayleigh distributed amplitude and uniformly distributed phase. Weibull distributions with parameters (a_T, ρ_T) were fitted to V_s with correlation coefficients larger than 0.98. It was observed that for fixed values of a (input clutter a) the output a_T as a function of target-to-clutter power ratio was to a large extent independent of the clutter-to-noise ratio (see figures 44, 45, and 46). Furthermore, it was observed that a_T as a function of signal-to-clutter ratio was linearly correlated with correlation coefficients greater than 0.99. This being the case and holding a fixed, the value of a_T is given by

$$a_T = M[P_s/P_c] + b$$

It was further noticed that as functions of a, both M and b were correlated to a and a^2 with correlation coefficients greater than 0.98. Explicity,

$$M = 0.1389 a^2 - 0.4917 a + 0.635$$
$$b = -1.2778 a^2 + 4.8167 a - 2.52$$
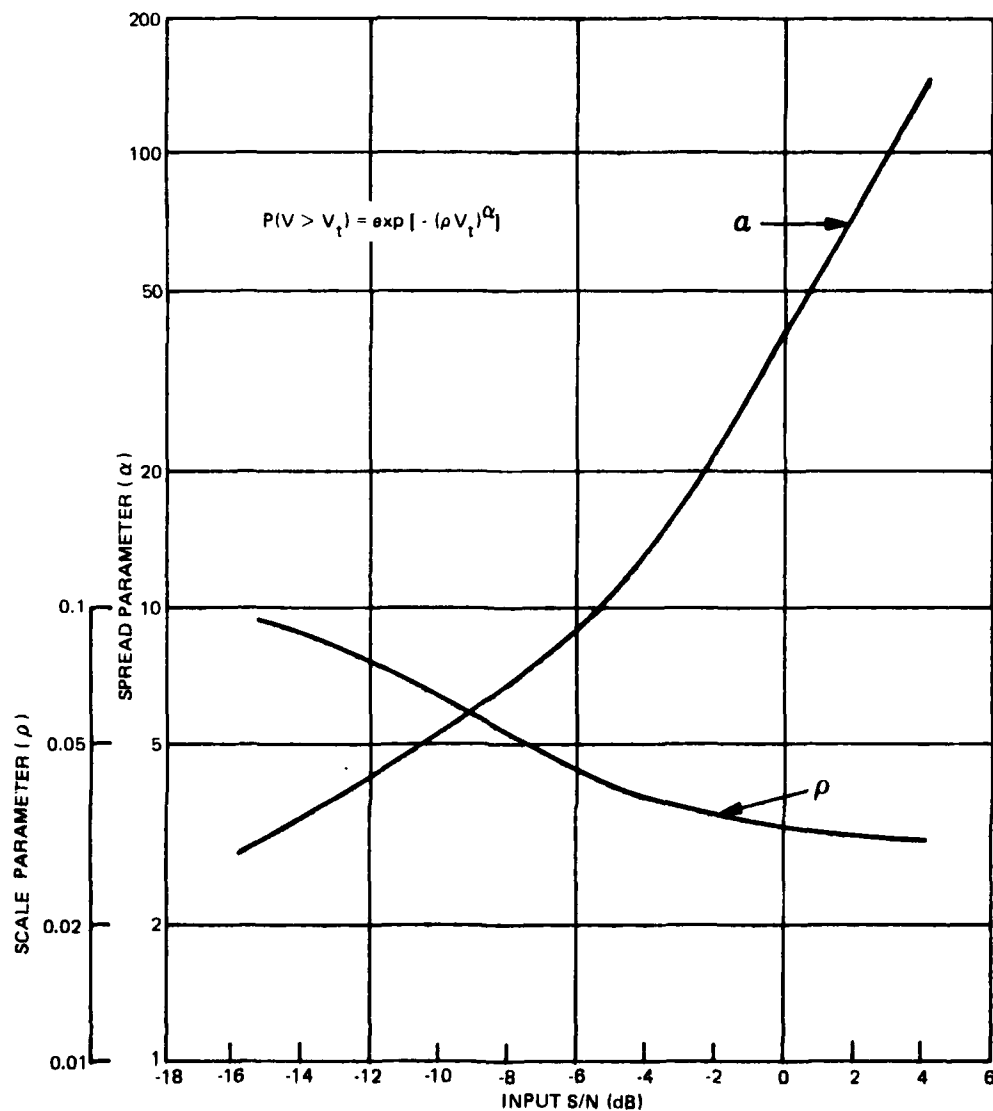
Figure 43. Parameters for Weibull Voltage Distribution Function
for Hard Limited Channels Versus Input SNR at Receiver

With this knowledge of a_T, together with the mean power P of V_s, the value
of ρ_T is determined by

$$\rho_T = \frac{1}{P}\left\{\Gamma[(2/a_T) + 1]\right\}^{1/2}$$

where $\Gamma(X)$ is the gamma function with argument X.
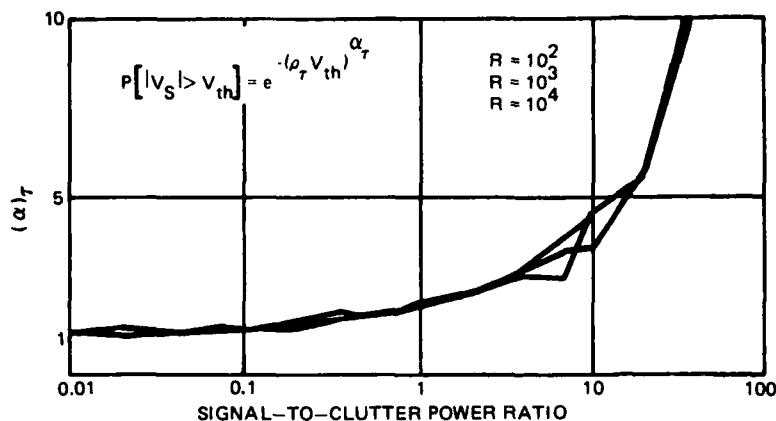
Figure 44.   Detected Voltage
Distribution Parameter, a = 1.2

$$V_s = S + C + N$$
S = Target signal with
constant amplitude
and uniformly dis-
tributed phase angle

C = Clutter with (a,ρ)-
Weibull distributed
amplitude and uni-
formly distributed
phase angle

N = Receiver noise with
Rayleigh distributed
amplitude and uni-
formly distributed
phase angle

$R = P_c/P_n$
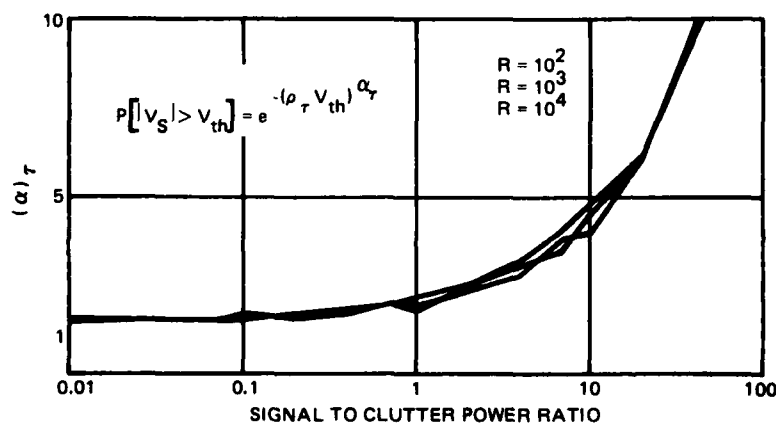
Figure 45.   Detected Voltage
Distribution Parameter, a = 1.5
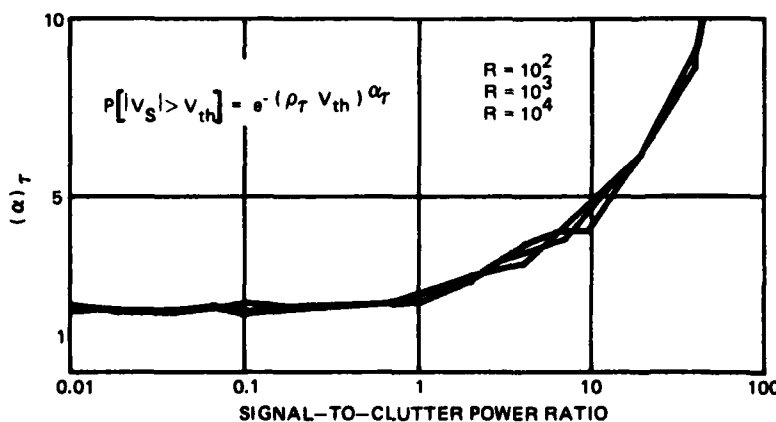
Figure 46. Detected Voltage
Distribution Parameter, a = 1.8

109

5.4 FUNCTIONAL SIMULATION MODEL

5.4.1 Model Overview

The simulation program is designed to permit analysis and evaluation of the radar tracking algorithms. To perform this function, the simulation program

o generates a target event file specifying target location and kinematics

o calculates the threshold and radar detection voltages for the specified events based on target, noise, and clutter input levels

o simulates the radar algorithms from target detection through target track reports

o processes data for performance analysis and evaluation.

As shown in the simplified functional flow diagram given in figure 47, the overall simulation program is divided into four main sections. This division was selected to facilitate changes in the subsections and to permit comparison of candidate algorithms under similiar conditions. The outputs from each section are recorded on file and may be recalled to supply the same inputs without rerunning the complete program.
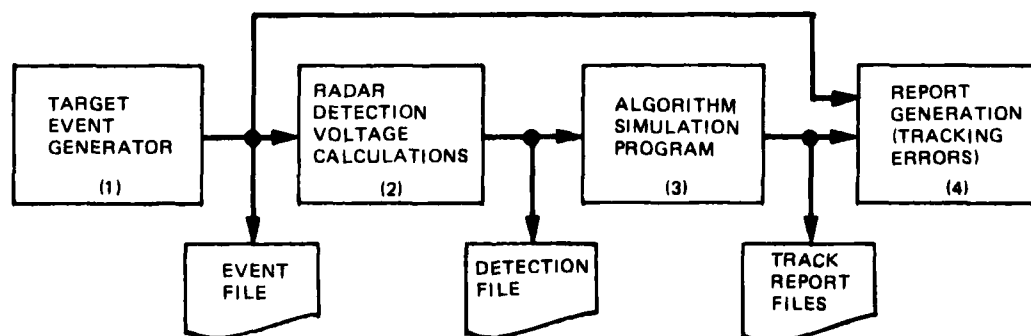
PURPOSE OF PROGRAMS

(1) GENERATES TARGET EVENT FILE SPECIFYING TARGET LOCATION AND KINEMATICS.

(2) CALCULATES THE RADAR DETECTION VOLTAGES FOR THE SPECIFIED EVENTS.

(3) SIMULATES ALGORITHMS FROM TARGET DETECTION THROUGH TARGET TRACK REPORTS.

(4) PROCESSES DATA FOR PERFORMANCE ANALYSIS AND EVALUATION.

Figure 47. Functional Simulation Programs

5.4.2 Target Event Generator

This simulation, similar to the pulse-to-pulse model, is event driven. The detection events are determined by the intercept of the radar scan with the target or clutter sources under investigation. The events are scheduled whenever the target is within a rotating azimuth scan sector centered at the azimuth beam pointing angle of the radar. The width of the sector is programmable to permit evaluation of the effects of sidelobe responses.

The event generator is sized to simulate 30 targets with independent trajectories. The trajectories may be either radial or offset.

The built-in trajectory generators will supply constant altitude, constant velocity targets. Each target is identified with a target identification number which is used in the subsequent subroutines for evaluation of the radar cross section. In addition, each event is tagged with an event number for use in the diagnostic and evaluation routines.

Whenever an event is scheduled, the target state vector, radar scan parameters, target aspect, and identification numbers are read into the event generator file. This file is used as an input for the radar detection voltage calculation section; it is also used for evaluation of the reported tracks.

5.4.3 Radar Detection Voltage Calculations

This section simulates the response of the radar processing using the functional relationship derived from the pulse-to-pulse simulation program. For each input on the event file, this subroutine calculates the response that would be obtained for each of four bursts and at each range interval containing the target. This subroutine determines the mean radar cross section of the target as a function of aspect angle and target type. It evaluates the mean clutter power and the receive noise at the receiver input, including the operations performed by the STC subroutine. The output of the doppler filter processing is obtained using the transfer function of all eight filters.

At this point, the previously obtained relationship between signal-to-noise and signal-to-clutter are used to obtain the output voltages for each doppler filter on each antenna beam. If any one of the detected output voltages exceeds the detection threshold voltage, all output voltages are written on the output file. In addition, the radar parameters which are used on that particular burst are recorded on the file using burst identification numbers.

5.4.4 Algorithm Simulation Program

The set of algorithms used in the initial simulation program contain the baseline algorithms outlined in Section 3. For the simulation program exercised, the algorithm program will

- read radar detection voltage file

- correlate detection data items over elevation, bursts,and azimuth beams

- form the scan detection list (SDL) for input to the tracking algorithms

- correlate SDL items with existing track windows

- resolve ambiguities and update associated tracks

- test for drop tracks

- process residual SDL items to form provisional (new) tracks

- initialize Kalman track for provisionals

- compute track windows for next scan

- output track reports.

Since the implementation of the tracking algorithm testing requires evaluation of the radar detection voltage on a burst-by-burst basis, this program is advanced from burst to burst. At each burst, the radar detected voltage file is examined to ascertain the presence of a signal. In addition, the false alarm subroutine is called to evaluate the false alarms. If neither a detected signal voltage nor a false alarm is present, a zero detection data item is entered, and the program proceeds in the usual manner. If either a detected voltage or a false alarm is present, the corresponding voltages are entered into the detection data file.

False alarms are generated using the functional relationship developed in the pulse-to-pulse simulation which are inverted to permit a direct calculation for the output voltages. At each beam position, three random draws from uniform distributions are used to determine the presence of a false alarm at that beam position, the range interval at which the false alarm occurs, and the filter output that contains the false alarms. This procedure is repeated for each of the three antenna beams.

Simplified flow diagram of the two major sections of this program are given in figures 48 and 49.

5.4.5 Report Generation Program

The report generation program is a diagnostic and evaluation program which formats the data from the tracking algorithm program for analysis and evaluation. This program accepts inputs from the track report file and the target event file to permit calculations of the errors and to supply diagnostic information on the algorithm performance. Typical outputs from this program include:

- heading and velocity errors

- target report file

- drop track file

- track status file.

Additional subroutines are available in this section for collection and segregation of errors, generation of histograms, and to format output diagnostic data.
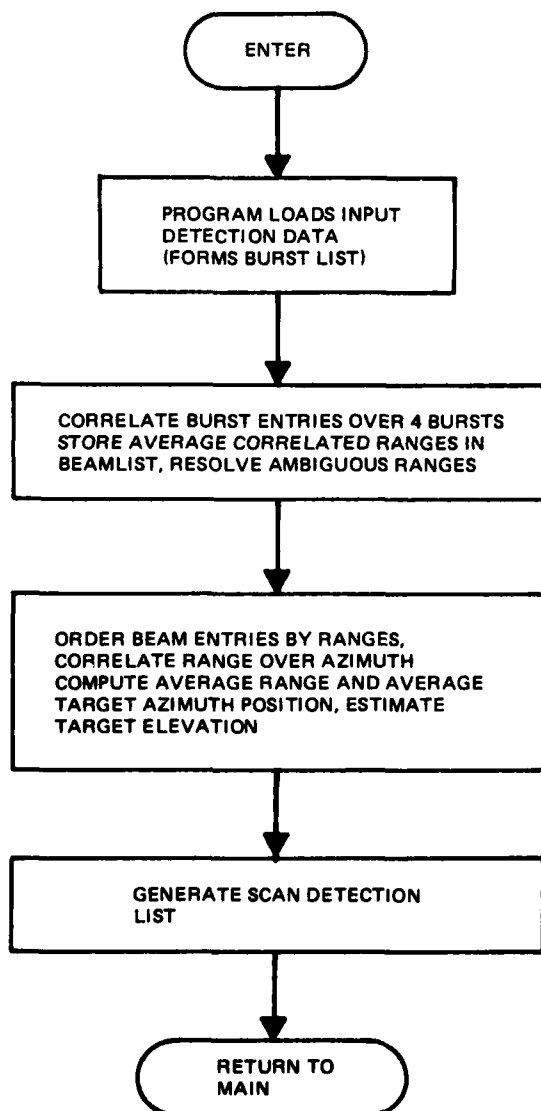
5.5 BASELINE RADAR PERFORMANCE EVALUATION

The functional simulation program for the baseline radar is being used to evaluate its performance in a minimally adverse arctic environment. The baseline radar is designed as being optimally sited, with ground clutter as the only adverse environmental factor. Simulation runs have been made to demonstrate performance in that environment, and the results are discussed below. A theoretical model of weather clutter has been generated and incorporated in the simulation. Some initial tracking results have been obtained with the weather model applied to the baseline radar. Because of the inherent MTI capability incorporated in the baseline for ground clutter, only a small degradation is noted. The structure for the Monte Carlo runs and the tracking results are presented below.

5.5.1 Speed and Heading Errors

This test was configured to test the speed and heading errors that would be obtained as a function of range for isolated target reports. To reduce the number of computer runs required, 10 targets were used on each run. The targets were spaced 10 kilometers on the same trajectory, all beyond the 100-kilometer range. The program was run until all targets were abreast of the radar.

Figure 48. Flow Diagram of Algorithm for Scan Detection List

113
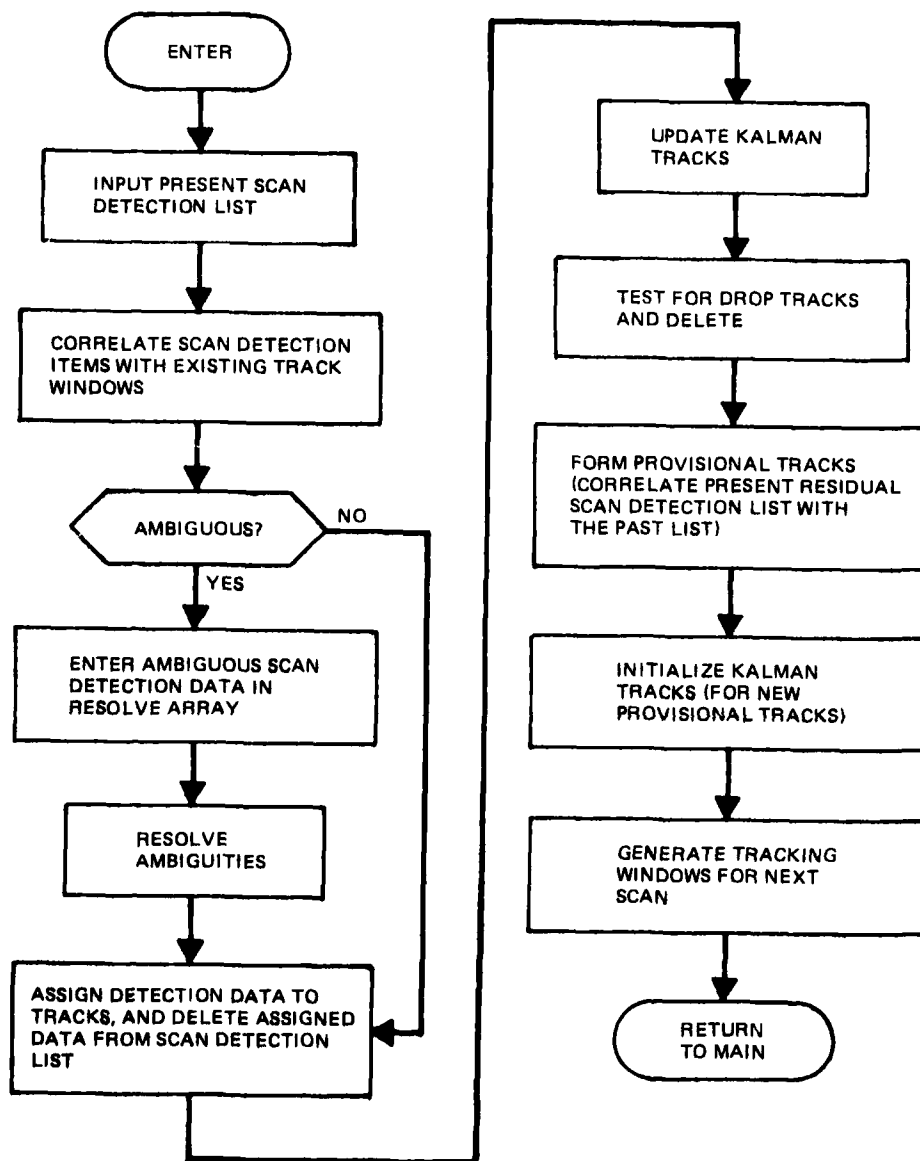
Figure 49. Flow Diagram for Tracking Algorithm

Output data were consolidated for analysis and evaluation by grouping all reports within 5 kilometers for each run. With 10 targets and approximately 4 scans per 5-kilometer window, 40 sample points were averaged to provide statistical rms and mean values. Range sampling at 300-meter intervals and azimuth quantization increments of 1.5 degrees were used.

114

The common parameters for these runs were:

Number of targets/run	10
Radar cross section	0.5 m^2
Target type	Constant cross section
Target trajectory	Constant altitude, constant velocity
Altitude	4.5 km ($\approx$ 15,000 ft)
Velocity	300 m/sec (1.2 km/scan)

Runs were made for both radial and offset target scenarios as illustrated in figure 50.

Performance in ground clutter of the above scenarios in terms of speed and heading error, are given in figures 51 through 54. The mean error curves for speed and heading are illustrated in figures 52 and 54, respectively. They represent one component of the rms errors and contribute less than 1/2 the acceptable error within the 55.6-kilometer (30 nmi) detection range. The total rms error plots in figures 51 and 53 indicate that, in almost all cases, the required accuracies of $\pm$10 percent speed (30 m/sec) and $\pm$2C degrees heading are achieved beyond the specified detection range of 30 nmi (55.6 kilometers). In figure 51, the 10-kilometer offset speed error curve
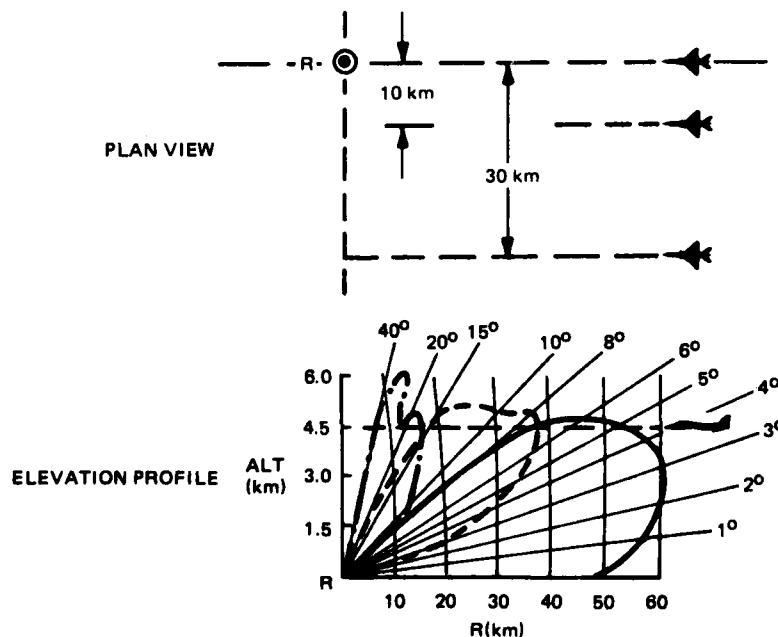
Figure 50. Simulated Target Flight Paths

illustrates an exceedance at 50 kilometers of 40 meters/second error. In this case, additional track smoothing to below the 50-kilometer range was required to reduce the error to within acceptable limits.

The altitude of 4.5 kilometers (15,000 ft) was selected to test the tracking capability in all of the three elevation beams as the targets penetrated the coverage. (See elevation profile of figure 50.) Target reports on all true targets were provided throughout the tracking range indicated on the figures. There were no false reports. The effects of ground clutter for these high altitude scenarios are still present in the low beam, requiring the necessary MTI and doppler suppression.

Initial simulation performance data in rain for the scenarios of figure 50 were also acquired utilizing the following additional run parameters:

Rain rate	=	4 mm/hr
Wind speed	=	27 m/sec
Wind direction	=	same as target direction
Rain altitude (max)	=	6.1 km
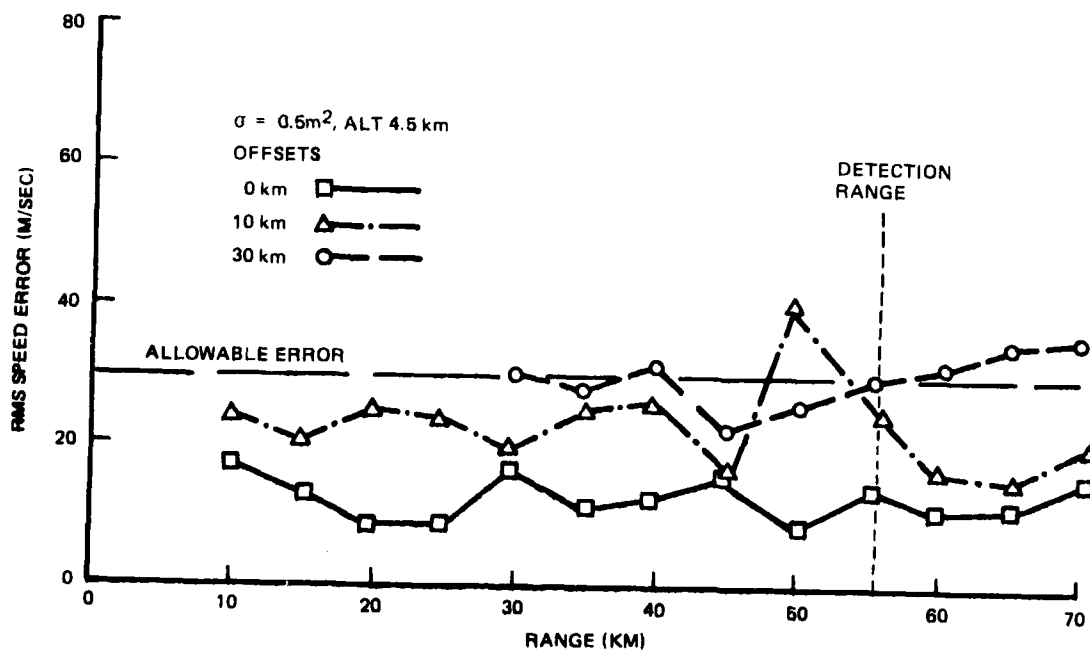
Figure 51. Rms Speed Error Versus Range (Clear Weather)
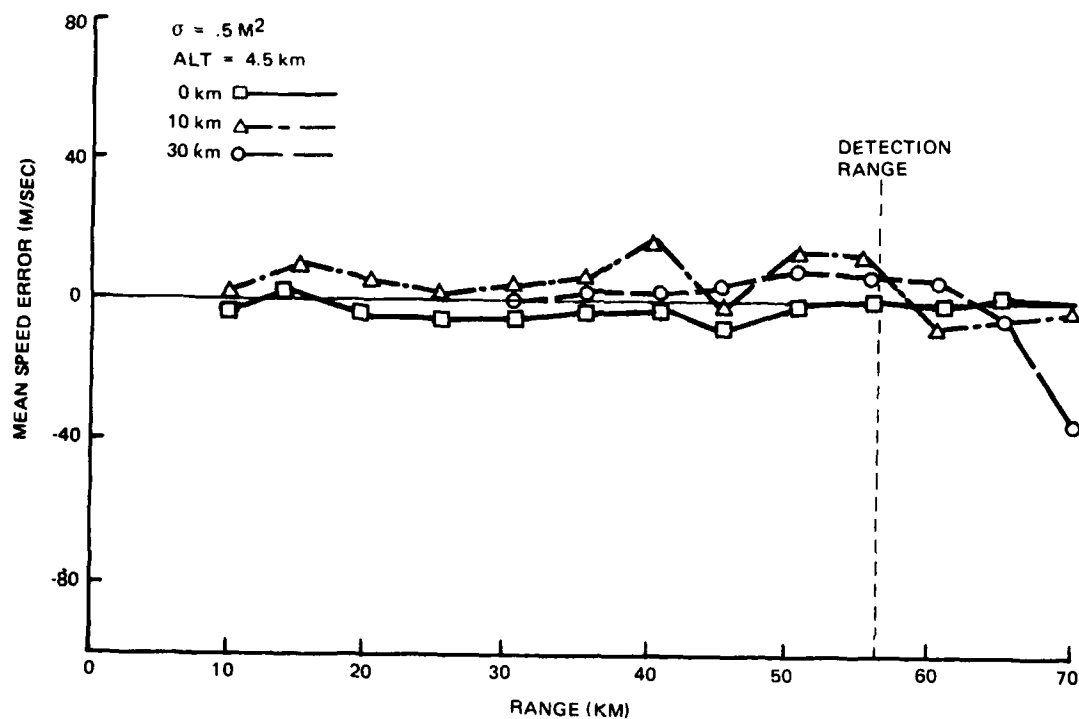
Figure 52.   Mean Speed Error Versus Range (Clear Weather)
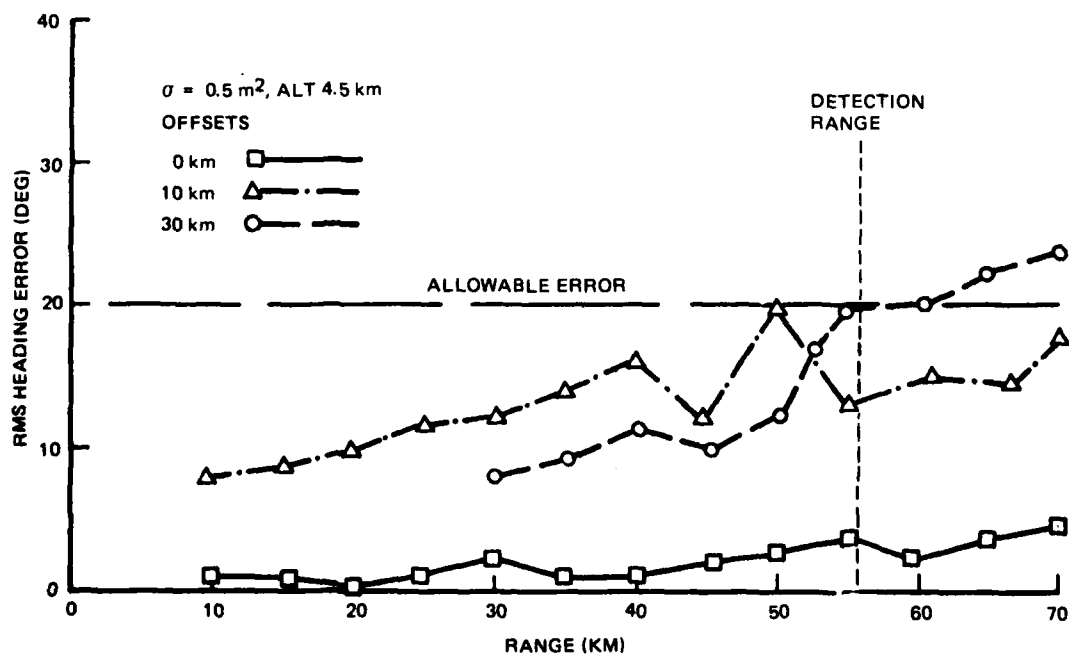
Figure 53.   Rms Heading Error Versus Range (Clear Weather)
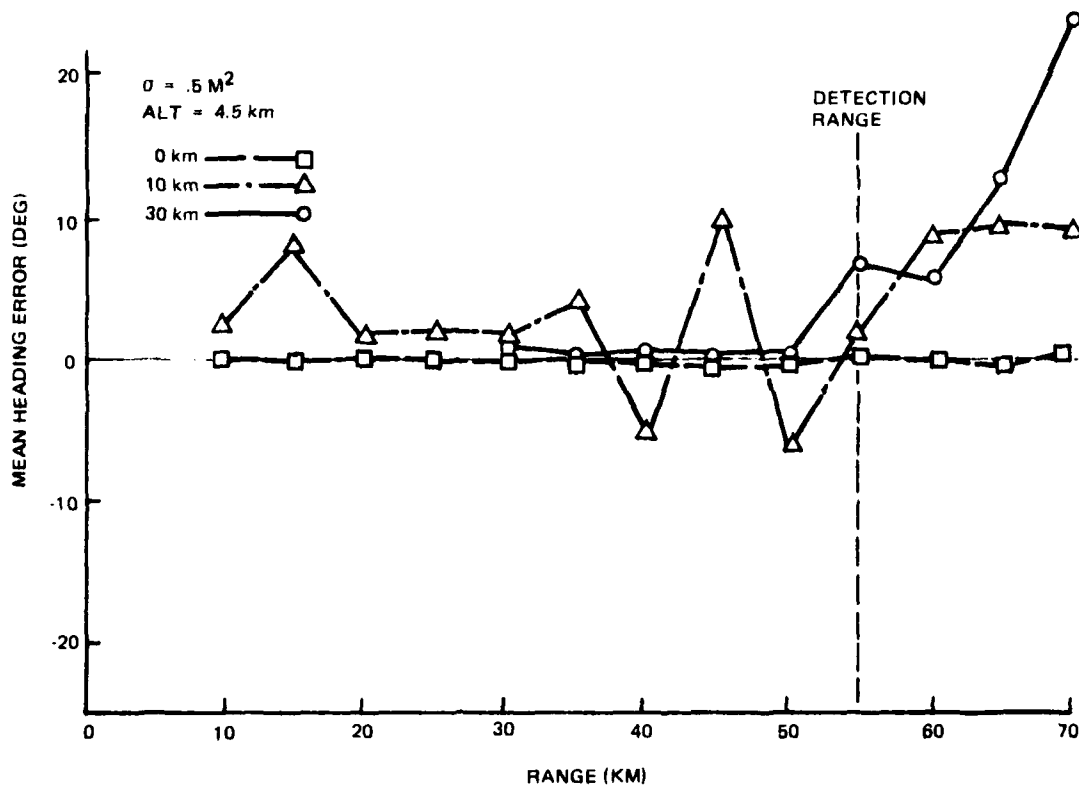
Figure 54. Mean Heading Error Versus Range (Clear Weather)

The rms heading errors presented in figure 55 fall within the $\pm$20-degree specification. However, in examining the rms speed errors of figure 56, performance degradation is indicated by these errors exceeding the allowable 10 percent limit. The errors are approximately 15 percent of actual speed at 55 kilometers (detection range for the 0.5 meter^2 target), dropping to within limits below 40 kilometers. Algorithms and techniques are presently being formulated to eliminate this deficiency. No difficulty is anticipated in this area during radar optimization.

118
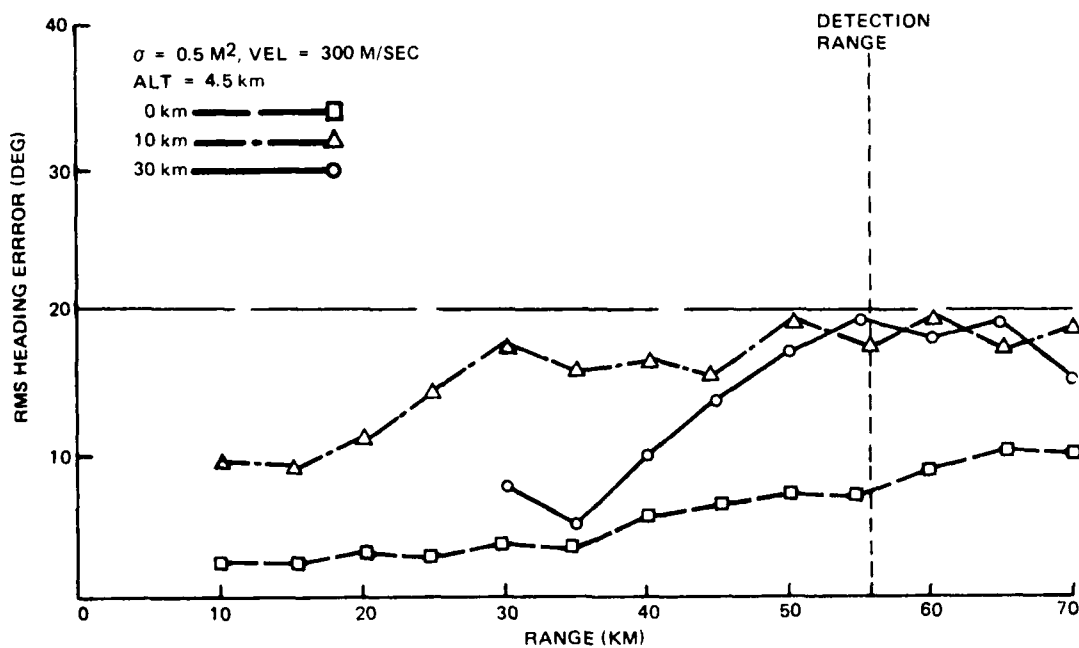
Figure 55. RMS Heading Error Versus Range (4mm/hr Rain Rate)
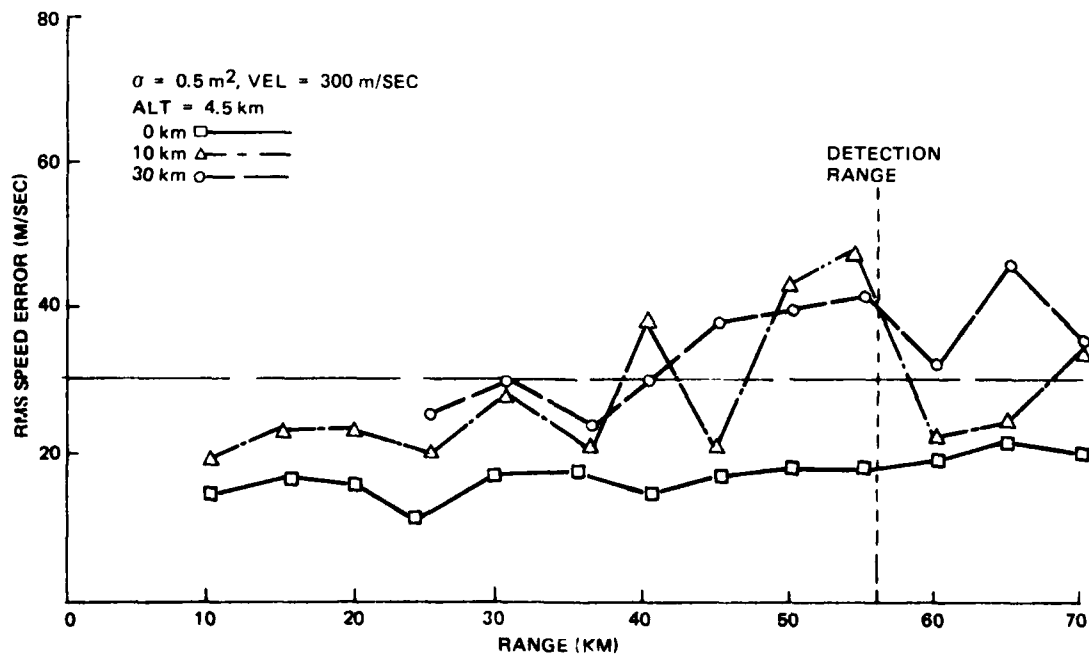
Figure 56. RMS Speed Error Versus Range (4 mm/hr Rain Rate)

119

Section 6

RELIABILITY

The measures which are most appropriate for expressing the radar reliability are probability of success $P_S(t)$ and mean time between failure MTBF. Since the radar in this study is to be unmanned, the system maintenance philosophy not only impacts its logistic support requirements, but it also influences the radar system reliability.

In this study, the radar site is operating unattended for periods of one to several months. It is assumed that a roving maintenance team will visit each site on a fixed periodic schedule for general site upkeep, preventive maintenance, and repair of all failed items. Thus, during each visit, the site is restored to a "full-up" condition. Sufficient built-in test capability is included in the baseline radar design to permit remote monitoring of all failures which occur while the radar is in operation. Advanced knowledge of repair tasks will be known to the maintenance team prior to the site visit.

The reliability of the baseline radar is achieved through judicious choice of redundancy to minimize the amount of hardware required. Moreover, where possible, stand-by redundancies are employed to minimize the power consumption.

The reliability goals for the radar were selected as:

Probability of success $(P_S) \geq 0.80$
Scheduled Site Maintenance Interval $\geq$ 3 months

The reliability block diagram for the baseline system is shown in figure 57. The types of redundancy employed in the various subsystems within the radar are so indicated. The probability of success $P_S(t)$ for each block, or a group of blocks which are redundant, is individually calculated using the following mathematical models:

Serial (Non-Redundant)

$$P_S(t) = e^{-\lambda t}$$

where t = scheduled maintenance interval
λ = failure rate of serial block

Operational Redundancy

$$P_S(t) = \sum_{m}^{n} \binom{n}{m} (e^{-m \lambda t})(1-e^{\lambda t})^{n-m}$$

where n = total number of units in parallel
m = minimum number of units required for operation

121

Standby Redundancy

$$P_s(t) = e^{-\lambda t} \left[\sum_{j=0}^{n-m} \frac{(m\lambda t)^j}{j!} \right]$$

where n = total number of units in parallel
      m = minimum number of units required for operation

System Reliability

$$P_s(t) = \prod_i P_i(t)$$

where $P_i(t)$ represents the probability of success for each block identified in figure 57.

The system reliability in terms of MTBF has been determined by the equation

$$MTBF_s = \frac{1}{\sum\limits_i \lambda_i + \sum\limits_j (\lambda_e)_j}$$

where MTBFs is the system MTBF. The $_i$ term represents the failure rate for the ith serial block in the system. A serial block is defined as a part of the system which has no redundancy.

The $(\lambda e)_j$ term represents the equivalent failure rate for the jth redundant block in the system. These failure rates have been computed using Epstein's formula.*

$$\lambda_e = \frac{1}{\sum\limits_{k=0}^{n-m} 1_{r+k, r+k-1}}$$

where

$$1_{r,r-1} = \frac{1}{\lambda_r} \left[1 + \frac{u_r}{\lambda_{r+1}} + \frac{u_r u_{r+1}}{\lambda_{r+1} \lambda_{r+2}} + \ldots + \frac{u_r u_{r+1} \cdots u_{r+m-1}}{\lambda_{r+1} \lambda_{r+2} \ldots \lambda_{r+m}} \right]$$

- - - - - - -

*B. Epstein, IEEE Proceedings, July 1965.

ANTENNA

UD 19
CIRCULATORS

λ_{19}

λ_{19}

STANDBY REDUNDANCY

3 OF 4

λ_{19}

λ_{19}

UD 18
TRANSMIT AMPLIFIER MODULE

λ_{18}

λ_{18}

STANDBY REDUNDANCY

3 OF 4

λ_{18}

λ_{18}

UD 15
COLUMN NETWORK
λ_{15}

UD 14
SP4T SWITCHES
λ_{14}

UD 13
AZIMUTH SWITCHING NETWORK
λ_{13}

UD 17
AZIMUTH PHASING NETWORK
λ_{17}

UD 12
DUPLEXERS
λ_{12}

UD 11
TRANSMIT DISTRIBUTION NETWORK
λ_{11}

UD 16
SIGNAL PROCESSOR

UD 16-1
UPPER BEAMS
$\lambda_{16.1}$

STANDBY REDUNDANCY
2 OF 3

UD 16-4
SYNCHRONIZER
$\lambda_{16.4}$

UD 16-2
LOWER BEAMS
$\lambda_{16.2}$

UD 16-5
SWITCHING MATRIX
$\lambda_{16.5}$

UD 16-3
SPARE
$\lambda_{16.3}$

TO SH 2

UD 2
FREQUENCY SYNTHESIZER

UNIT #1
$\lambda_{2.2}$

STANDBY REDUNDANCY

$\lambda_{2.1}$

UNIT #2
$\lambda_{2.2}$

MEMORY
λ_{7}

UD 1
RECEIVER

$\lambda_{1.4}$

STANDBY REDUNDANCY
1 OF 2

$\lambda_{1.4}$

STA
RE
1 O

1

Figure 57. RRAS Baseline System
Reliability Block Diagram
(Sheet 1 of 2)

123

DATA PROCESSOR

COMMON MEMORY $\lambda_{3.3}$

COMMON MEMORY $\lambda_{3.3}$

OPERATIONAL REDUNDANCY

FROM SH 1

COMMON MEMORY $\lambda_{3.3}$

3 OF 5

COMMON MEMORY $\lambda_{3.3}$

COMMON MEMORY $\lambda_{3.3}$

GENERAL PURPOSE CPU $\lambda_{3.2}$

STANDBY REDUNDANCY 1 OF 3

GENERAL PURPOSE CPU $\lambda_{3.2}$

GENERAL PURPOSE CPU $\lambda_{3.2}$

SPECIAL PURPOSE CPU $\lambda_{3.1}$

STANDBY REDUNDANCY 1 OF 2

SPECIAL PURPOSE CPU $\lambda_{3.1}$

SPECIAL PURPOSE CPU $\lambda_{3.1}$

SPECIAL PURPOSE CPU $\lambda_{3.1}$

SPECIAL PURPOSE CPU $\lambda_{3.1}$

SPECIAL PURPOSE EPU $\lambda_{3.1}$

UD-6,7

OPERATIONAL REDUNDANCY 1 OF 2

D.C. POWER SOURCES AND DISTRIBUTION

UD 5

A.C. POWER DISTRIBUTION λ_5

+3V P/S (SWITCHING) $\lambda_{6.2}$

+5V P/S (LINEAR) $\lambda_{6.3}$

+5V P/S (SWITCHING) $\lambda_{6.12}$

-5V P/S (LINEAR) $\lambda_{6.4}$

+8V P/S (LINEAR) $\lambda_{6.6}$

+8V P/S (SWITCHING) $\lambda_{6.5}$

+15V P/S (LINEAR) $\lambda_{6.7}$

+3V P/S (SWITCHING) $\lambda_{6.2}$

+5V P/S (LINEAR) $\lambda_{6.3}$

+5V P/S (SWITCHING) $\lambda_{6.12}$

-5V P/S (LINEAR) $\lambda_{6.4}$

+8V P/S (LINEAR) $\lambda_{6.6}$

+8V P/S (SWITCHING) $\lambda_{6.5}$

+15V P/S (LINEAR) $\lambda_{6.7}$

Figure 57. RRAS Baseline System
Reliability Block Diagram
(Sheet 2 of 2)

125

and

r = the state index

$l_{r,r-1}$ = average state transition time

λ_r = total state failure rate

n = total number of units in parallel

m = minimum number of units required for operation of the
redundant block

u_r = repair rate for a parallel unit

λ_e = equivalent failure rate for a redundant block

The estimated failure rates identified with λ_{sub} in the reliability
block diagram, figure 57, are tabulated in table 15.

The system reliability, both in terms of $P_s(t)$ and MTBF is plotted
in figure 58. This shows that the two reliability goals can be met when
the system is configured with adequate redundancies in subsystems requiring
more complex circuits.
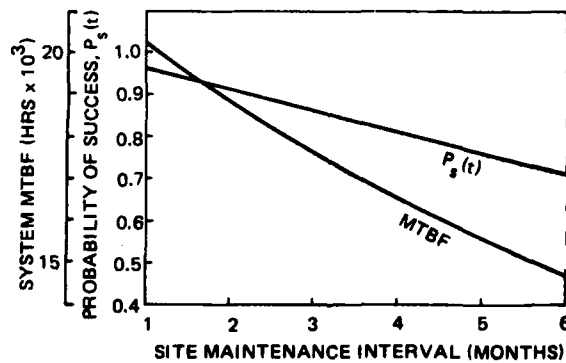
Figure 58. System MTBF and Probability of Success Versus
Maintenance Interval

Table 15. RRAS Baseline Reliability Estimates

λ Designation	Subsystem	Configuration	Failure Rate (λ) per Million Hrs	Equivalent Failure Rates (λ_e)		
				1 month	2 months	3 months
1.1	Receiver	Serial	2.444	2.444	2.444	2.444
1.2	Receiver	Standby	13.741	0.134	0.390	0.749
1.3	Receiver	}1 of 2	13.741	0.134	0.390	0.749
1.4	Receiver		13.741	0.134	0.390	0.749
2.1	Frequency synthesizer	Serial	0.082	0.082	0.082	0.082
2.2	Frequency synthesizer	Standby 1 of 2	20.396	0.293	0.843	1.523
3.1	Data processor, special purpose CPU	Standby 1 of 2	60.000	2.434	6.510	11.198
3.2	Data processor, general purpose CPU	Standby 1 of 3	25.000	0.0001	0.0002	0.0003
3.3	Common memory	Operational 3 of 5	25.000	0.040	0.336	1.226
4	Communications	Serial	4.350	4.350	4.350	4.350
5	AC power distribution	Serial	0.948	0.948	0.948	0.948
6.1	DC power distribution control ckt and bite	Serial	0.870	0.870	0.870	0.870
6.2	+3V Power supply (switching type)	Operational 1 of 2	10.000	0.071	0.209	0.406
6.3	+5V Power supply (linear type)	Operational 1 of 2	1.0	0.0007	0.002	0.004
6.4	-5V Power supply (linear type)	Operational 1 of 2	1.0	0.0007	0.002	0.004
6.5	+8V Power supply (switching type)	Operational 1 of 2	8.0	0.046	0.135	0.263
6.6	+8V Power supply (linear type)	Operational 1 of 2	1.0	0.0007	0.002	0.004
6.7	+15V Power supply (linear type)	Operational 1 of 2	2.0	0.003	0.009	0.017

Table 15. RRAS Baseline Reliability Estimates (Cont'd)

λ Designation	Subsystem	Configuration	Failure Rate (λ) per Million Hrs	Equivalent Failure Rates (λe)		
				1 month	2 months	3 months
6.8	-15V Power supply (linear type)	Operational 1 of 2	2.0	0.003	0.009	0.017
6.9	+28V Power supply (switching type)	Operational 1 of 2	10.0	0.071	0.209	0.406
6.10	+28V Power supply (linear type)	Operational 1 of 2	1.0	0.0007	0.002	0.004
6.11	+100v Power supply (linear type)	Operational 1 of 2	1.0	0.0007	0.002	0.004
6.12	+5V Power supply (switching type)	Operational 1 of 2	10.0	0.071	0.209	0.406
6.13	Load sharing and sensor circuits	Serial	0.082	0.082	0.082	0.082
7	Memory	Serial	1.1	1.1	1.1	1.1
8	Bite DAU	Serial	8.7	8.7	8.7	8.7
9	Solid state amplifier	Standby 10 of 11	1.06	0.044	0.130	0.255
10	Beam control unit	Operational 808 of 810	25.757	0.235	0.679	1.290
11	Transmitter distribution netw.	Serial	1.0	1.0	1.0	1.0
12	Duplexers (2)	Serial	4.0	4.0	4.0	4.0
13	Azimuth switching networks (3)	Serial	2.916	2.916	2.916	2.916
14	SP4T switches (3)	Serial	1.944	1.944	1.944	1.944

Table 15. RRAS Baseline Reliability Estimates (Cont'd)

λ Designation	Subsystem	Configuration	Failure Rate (λ) per Million Hrs	Equivalent Failure Rates (λ_e)		
				1 month	2 months	3 months
15	Column network	Serial	0.1	0.1	0.1	0.1
16.1 16.2 16.3	Signal processor beams	Standby 2 of 3	21.794	0.987	2.754	4.983
16.4	Signal processor synchronizer	Serial	10.478	10.478	10.478	10.478
16.5	Signal processor switching matrix	Serial	3.388	3.388	3.388	3.388
17	Azimuth phasing network	Serial	0.81	0.81	0.81	0.81
18	Transmitter amplifier	Standby 3 of 4	4.35	0.081	0.237	0.460
19	Circulators	Standby 3 of 4	1.5	0.0097	0.0288	0.057

Section 7

CONCLUSIONS

A baseline radar has been defined to the subsystem level and evaluated in a minimally adverse arctic environment which assumes remote unattended operation, optimal siting, and a ground clutter environment which requires coherent doppler processing. The design was tailored to meet a level of performance defined by: detection probability (0.9), track initiate probability (0.95), track maintenance probability (0.95), track accuracy (20 degrees heading, 10 percent speed), and false report rate (one in 30 days). The radar design has an inherent management capability which was not exercised in establishing baseline performance. This results from flexible hardware architecture, software control of scheduling and processing, inertialless beam pointing, and transmitter tolerance to waveform diversity. Growth paths to incorporate allocation algorithms can be established with minimal hardware redesign.

Baseline performance was evaluated by a two-phase computer simulation consisting of a pulse-to-pulse radar simulation to develop functional relationships between clutter models and target detectability, and a tracking simulation which uses the functional relationship as a detection algorithm. The pulse-to-pulse model transforms signal plus Weibull and Rayleigh spatial clutter model distributions into detector voltage distributions. It includes the convolution of the antenna pattern with the spatial distribution, STC, range sidelobe summation effects of pulse compression, hard limiting, and coherent receiver digital doppler processing. Results of the pulse-to-pulse simulation are incorporated in the detection algorithm of the tracking simulation which includes detection, multi-target track processing, and target correlation. Results of the combined simulations validate baseline performance.

During the next phase of the study, the hostile environmental models of birds, weather, mutual interference, multi-lobing, and siting problems will be applied to the baseline to determine the performance degradation and to develop corrective algorithms. Mathematical analysis of the hostile environment, weather, and sea clutter indicates that edge filter visibility is diminished under extreme wind conditions and drop tracks are expected in the unmanaged system. High altitude siting also presents visibility limitations in sea clutter because of the dependence of the backscatter coefficient on grazing angle. While high elevation siting minimizes ground shadowing effects, it causes clutter problems because the radar must look down at the surface to detect low altitude penetrators.

The types of performance degradation expected are (1) blind zones in both spatial and doppler coverage due to terrain shadowing, multi-lobing, weather, clutter, and sector overloads, and (2) false track reports due to overlapping velocity and amplitude signatures of birds and targets. The functional requirements and corresponding resources required to correct these deficiencies will be evaluated and algorithms developed to allocate the required resources. Radar modifications to implement individual techniques and compatible algorithm sets will then be defined.

131

Appendix A

CLUTTER PERFORMANCE

The signal-to-clutter performance of each doppler filter in the RRAS baseline radar was evaluated in the minimally adverse arctic clutter environment. The clutter consisted of terrain, sea, and weather. The clutter model used in the analysis was that of the SEEK FROST program and was provided by the "Enhanced Distant Early Warning (EDEW) Draft Specification," Number ESD-SS-SF-12412, dated 23 March 1979. This model is summarized in Appendix B. The subsections which follow present the doppler filter responses and the signal-to-clutter performance of the doppler filters for each of the clutter types.

A.1 DOPPLER FILTER RESPONSE

The RRAS signal processor consists of eight doppler filters which are identified as doppler filters 0 through 7. Figure A-1 shows the eight-filter composite voltage response which has been normalized to a unity output noise level. In the figure, a phase precession of 360 degrees corresponds to a zero-doppler velocity or blind speed. The blind speeds occur at $n \lambda f_r/2$, where n is an integer, λ is the radar wavelength, and f_r is the pulse repetition frequency (prf). For the baseline radar, both frequency and prf were varied on alternate bursts to control blind speed locations. When the ratio of blind speeds is 3/4, the first common blind speed occurs at 3 times the blind speed of the high prf transmission as shown in figure 6 of Section 1. Four prf's are used in the system, but one pair is a small perturbation of the other for the purpose of range ambiguity resolution. Since the difference is so small, it has a negligible effect on clutter performance, and the clutter analysis was conducted for the average high prf (1235 Hz) and the average low prf (979). The frequencies assigned to these values are 1300 and 1369 MHz, respectively. It should be noted that filter pairs 1 and 7, filters 2 and 6, and filters 3 and 5 have voltage responses which are mirror images. Filter zero contains substantially all of the clutter spectrum and therefore has no inherent SCI. Targets are detected by means of intra- and supra-clutter visibility provided by clutter maps.

A.2 TERRAIN CLUTTER

The terrain clutter voltage distribution is defined in Appendix B by the Weibull probability density function. The probability distribution function for the backscatter coefficient σ_0 (after transition through a power law device) can then be expressed as

$$P(\sigma \leq \sigma_0) = 1 - \exp \left\{ \ln 0.5 \left[\frac{\sigma_0}{\sigma_m} \right]^{b/2} \right\}, \quad \sigma_0 \geq 0$$

133
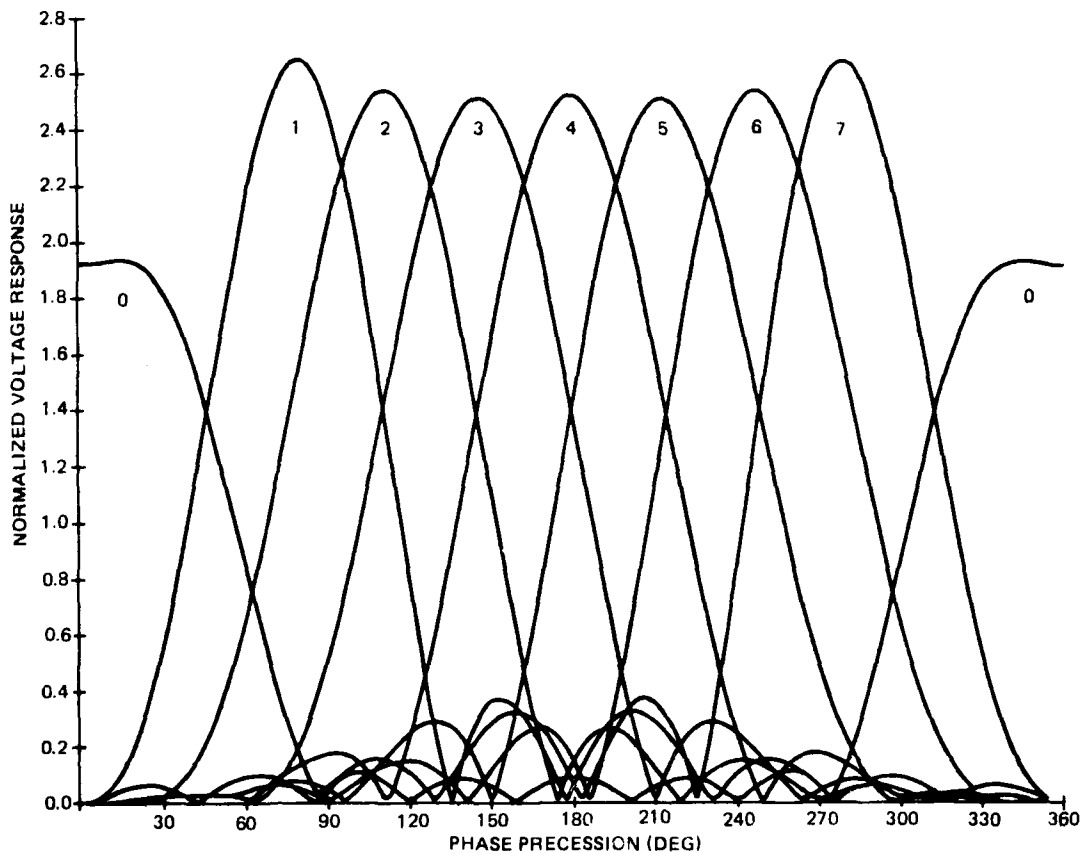
Figure A-1.   Doppler Filter Response

This equation gives the probability that the backscatter coefficient does not exceed σ_o.   b is defined as the shape parameter and σ_m is the median value of the backscatter coefficient.   The equation can be rearranged to solve   for σ_o.

$$\sigma_o = \sigma_m \left[\frac{\ln (1-P)}{\ln 0.5} \right]^{2/b}$$

Values for σ_m and b are given in table A-1 for tundra, moderate hills and mountains, and severe hills and mountains.   A 99-percentile design value for P was selected.   This means that 99 percent of the clutter will not exceed the resulting value of σ_o.   The clutter RCS σ_c is listed in table A-1 for a range of 30 nmi, a 300-meter range resolution, and a 3-degree azimuth beamwidth.

134

Table A-1. Terrain Clutter Cross Section

Clutter Type	σ_m (db)	b	σ_o (dB)	Clutter Area (dBm^2)	σ_c (m^2)
Tundra (P$_1$)	-50	2.3	-42.8	57.9	32.4
Moderate Hills/Mountains (P$_2$)	-42	3.3	-37.0	57.9	123.0
Severe Hills/Mountains (P$_3$)	-35	3.2	-29.9	57.9	631.0

Table A-2 lists the required signal-to-clutter (SCI) improvement factor for each of the baseline radar doppler filters. This is based on detecting a 0.5-meter^2 target in the severe hills/mountains environment (RCS = 631.0 meters^2) with a visibility factor Vo of 2.7 dB per pulse (an integrated signal-to-interference ratio of 11.7 dB). The computation accounts for the gain of each doppler filter (also known as the signal-to-noise improvement factor). As can be seen from the table, the required SCI is 49.5 dB for each filter. For the moderate hills/mountains characteristic (P$_2$), the required SCI is reduced by 7.1 dB for each filter; for tundra (P$_1$), it is reduced by 12.9 dB for each filter.

The power spectral density for terrain clutter consists of an impulse function at zero doppler plus a symmetric, continuous polynomial function. Based on this spectrum, the SCI achieved for each doppler filter is presented in table A-2 for each prf. It is evident from the table that the SCI of each filter (except the zero-doppler filter) far exceeds the required SCI, even for the severe terrain characteristic (P$_3$). This is a result of the relatively narrow clutter spectrum and the radar double canceller and stability.

Table A-2. Terrain Clutter Filter Performance

Doppler Filter Number	Filter Gain (dB)	SCI Required (dB)	SCI Achieved* (dB)
1,7	8.5	49.5	>90
2,6	8.1	49.5	>90
3,5	8.0	49.5	>90
4	8.1	49.5	>90

* Filter shape characteristic; however, instrumentation limit is 60 dB.

135

A.3 WEATHER CLUTTER

The weather clutter model is defined for both Arctic Circle and Labrador sites (Appendix B). The clutter is characterized by cellular, uniform, and bright band rainfall. The precipitation extends to a 6000-foot altitude in the arctic, and to 10,000 feet in Labrador. In addition, the rainfall rates are greater in Labrador than they are in the Arctic Circle region.

The weather clutter is characterized by a volume cell Vc given by

$$Vc = \left[\frac{\pi R^2}{8} \right] \left[\frac{c\tau}{2} \right] \theta_1 \phi_1$$

where R is the slant range

$c\tau/2$ is the range resolution cell

θ_1 is the one-way, 3-dB azimuth beamwidth

ϕ_1 is the one-way, 3-dB elevation beamwidth

For certain geometries, the elevation beamwidth ϕ_1 must be replaced by the angular extent of the clutter up to the altitude cutoff. For the present analysis, the slant range selected was 30 nmi, the range resolution cell was 300 meters, the azimuth beamwidth was 3 degrees, and the elevation extent was 3.2 degrees for Labrador (10,000-foot cutoff) and 1.9 degrees for the Arctic Circle (6000-foot cutoff). The reflectivity η is given by

$$\eta = (6.12 \times 10^{-14}) \frac{r^{1.6}}{\lambda^4} \ (m^{-1})$$

where r is the rainfall rate (mm/hr)

λ is the radar wavelength (meters)

Using the maximum cellular rainfall rate of 10 mm/hr for Labrador and 6 mm/hr for the Arctic Circle, the weather clutter RCS was 0.90 meter^2 and 0.24 meter^2 respectively, for Labrador and the arctic. For the same detectability parameters used previously with terrain and sea clutter, the required SCI to detect a 0.5-meter^2 target is presented in table A-3. The table distuinguishes between Labrador and Arctic Circle weather clutter.

The weather clutter spectrum is a Gaussian density function. The mean velocity of the power spectral density can have any value between ±25 meters per second. The standard deviation σ_v is given by

136

$$\sigma_v = 1.12 \quad [1 + 7.68R^2\emptyset^2]^{1/2}$$

where R is the radar range (nmi)

$\emptyset$ is the vertical beamwidth (rad)

If the vertical beamwidth is greater than the angular sector from the ground
to the altitude cutoff, then the smaller of the two values must be used for
$\emptyset$. For 30 nmi, the standard deviation of the spectrum is 5.2 meters/second
for Labrador and 3.3 meters/second for the Arctic Circle.

For this clutter spectrum, the performance of doppler filters 1 through 3
is shown in figures A-2 and A-3 for Labrador and Arctic Circle sites, respec-
tively. The asymmetric shape of the curves is caused by the filter shapes
and sidelobes. For positive velocities, the mean of the clutter spectrum is
shifted toward the main lobe of the filter response. As more clutter is re-
ceived in a given filter, the SCI degrades, correspondingly, to the point
where clutter is enhanced rather than suppressed. For negative velocities,
the clutter is shifted out of the zero notch into far-out sidelobes where the
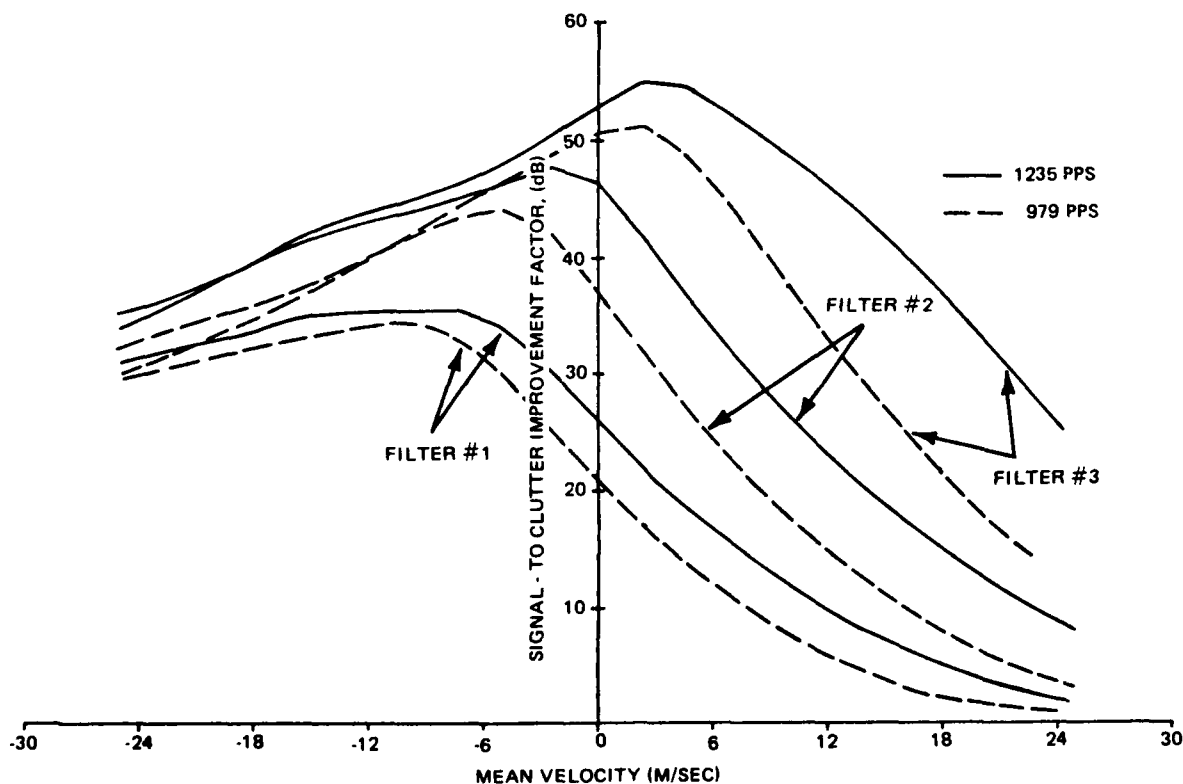curves flatten out at the average doppler sidelobe level.

Figure A-2.   Labrador Weather Clutter SCI for 30-nmi Range
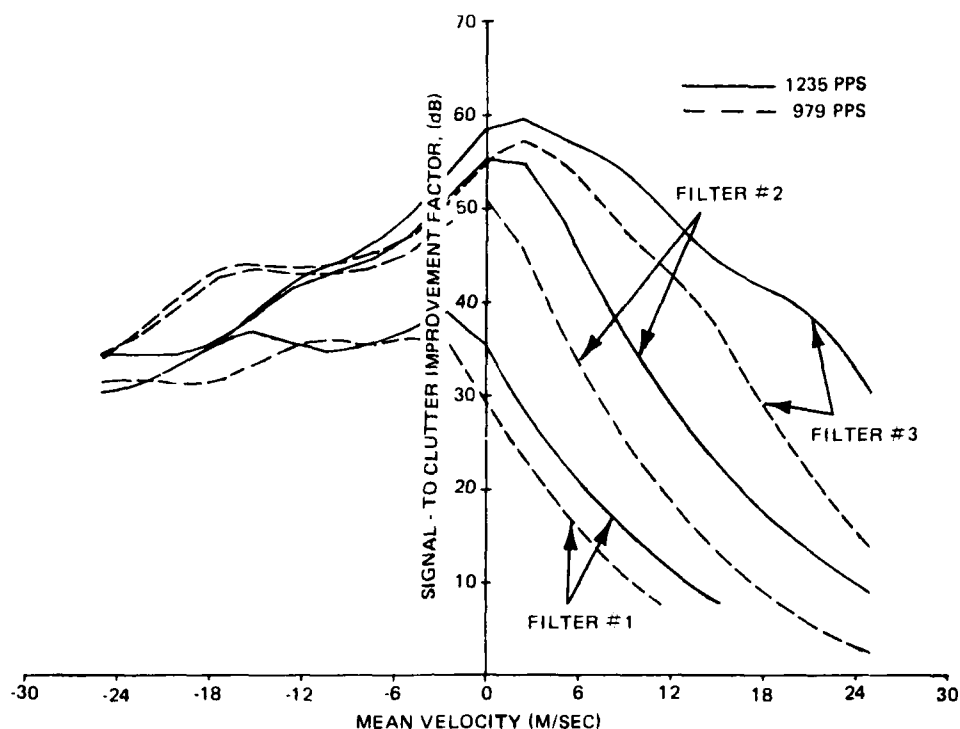and 10,000-foot Altitude

137

Figure A-3. Arctic Circle Weather Clutter SCI for 30-nmi Range
and 6,000-foot Altitude

Table A-3 lists the range of mean velocities for each filter in which the
doppler filter performance meets the system requirements. Analysis of the
data indicates that portions of filters 1, 2, and 3 do not satisfy the re-
quired improvement factor requirements for the low prf while portions of fil-
ters 1 and 2 do not meet the SCI requirements for the high prf. It should be
recalled that these are worst-case results, based on maximum rainfall rates,
maximum altitudes and range. For the uniform rainfall rate of 2 mm/hr
(Labrador) and 1 mm/hr (Arctic Circle), the clutter RCS is reduced by 11.2 dB
and 12.4 dB, respectively. This increases the range of mean velocities for
which the filters satisfy the signal-to-clutter improvement factor require-
ments (see table A-4). For Labrador, only filters 1 and 2 fail to satisfy
the SCI required; for the Arctic Circle, only filter 1 has a degraded per-
formance for all ranges of mean velocity.

A.4 SEA CLUTTER

The spatial distribution for distributed sea clutter is characterized by
the Weibull function. Values of $_m$ for various depression angles, radar
operating bands, and antenna polarizations are given in Appendix B. For
radar sites in the eastern sector, the maximum site altitude is given as 3400
feet above MSL. For a target at 30 nmi, this results in a 0.88-degree

138

Table A-3. Weather Clutter Filter Performance

Doppler Filter No.	Labrador (RCS = 0.9 meter²)			Arctic Circle (RCS = 0.24 meter²)		
	SCI Required (dB)	Mean Velocities (m/s) Providing Required SCI 1235 pps	979 pps	SCI Required (dB)	Mean Velocities (m/s) Providing Required SCI 1235 pps	979 pps
1, 7	21.0	-25 to 3	-25 to 0	15.2	-25 to 9.4	-25 to 6.4
2, 6	21.0	-25 to 13.5	-25 to 8	15.2	-25 to 19.8	-25 to 14.0
3, 5	21.0	-25 to 25	-25 to 18.2	15.2	-25 to 25	-25 to 24.6
4	21.0	-25 to 25	-25 to 25	15.2	-25 to 25	-25 to 25

Table A-4. Uniform Rain Clutter Performance

Doppler Filter No.	Labrador (RCS = 0.068 meter²)			Arctic Circle (RCS = 0.014 meter²)		
	SCI Required (dB)	Mean Velocities (m/s) Meeting Required SCI 1235 pps	979 pps	SCI Required (dB)	Mean Velocities (m/s) Meeting Required SCI 1235 pps	979 pps
1, 7	9.8	-25 to 11.9	-25 to 7.8	2.8	-25 to 22.5	-25 to 17.2
2, 6	9.8	-25 to 23	-25 to 16.1	2.8	-25 to 25	-25 to 25
3, 5	9.8	-25 to 25	-25 to 25	2.8	-25 to 25	-25 to 25
4	9.8	-25 to 25	-25 to 25	2.8	-25 to 25	-25 to 25

139

maximum grazing angle. Therefore, since the baseline radar operates at L-band with vertical polarization, the median value of the backscatter coefficient is interpolated as -45.4 dB. However, the shape parameter b is not defined in Appendix B. Schleher* defines the shape parameter as ranging from 1.160 to 1.783 for sea state 3. For this analysis, therefore, the mid-range value of 1.472 was selected for b. Again, choosing a 99 percentile value, σ_o is -34.2 dB. The resultant RCS for the sea clutter at 30 nmi is 236.2 meters^2.

The signal-to-clutter improvement factor required to detect a 0.5-meter^2 target in sea clutter (RCS = 236.2 meters^2) is 45.2 dB as shown in table A-5. This value of SCI is for a 2.7 dB/pulse visibility factor, an 11.7 dB signal-to-interference ratio, and eastern sector sites.

Table A-5. Sea Clutter Filter Performance

Dopper Filter Number	SCI Required (dB)	Filter SCI* (dB) Mean Clutter Velocity		
		-2.5 m/s	0	+2.5 m/s
1,7	45.2	45.7	55.9	40.2
2,6	45.2	58.3	72.0	60.1
3,5	45.2	61.7	76.0	64.7
4	45.2	73.0	90.4	73.0

* Filter shape characteristic; however, instrumentation limit is 60 dB.

The sea clutter power spectral density is defined by a Gaussian function with a 3 dB width of 2.5 meters/second. The mean velocity can have any value between -2.5 and 2.5 meters/second. The doppler filter performance for sea clutter is listed in table A-5 for a prf of 1235 pps. Comparison of SCI performance versus requirements reveals that only doppler filter 1 does not exceed the required SCI for all values of mean velocity, and this is only for a small range of positive mean velocities. As noted before, this is a worst-case result only for the eastern sector sites which are at a maximum of 3400 feet above sea level. For eastern sites at altitudes below 3400 feet, the grazing angle would be reduced, the clutter cross section would be reduced, and, consequently, the required SCI would be reduced.

The western and central sector sites are at a maximum altitude of 1300 feet above MSL. This results in a 0.22 degree maximum grazing angle. Via interpolation, the median backscatter value is -57.7 dB and the sea clutter RCS is 13.6 meters^2. This is a change of -12.4 dB with respect to the eastern sector cross section of 236.2 meters^2. Hence, the required SCI is reduced by 12.4 dB for each doppler filter. Therefore, the improvement factor of all of the doppler filters meets this requirement.

- - - - - - -

*Schleher, D.C., "Radar Detection in Weibull Clutter," IEEE Transactions on Aerospace and Electronic Systems, Vol. AES-12, No. 6, Nov. 1976.
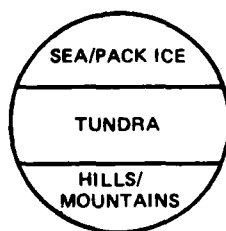
Appendix B

RRAS CLUTTER MODEL

B.1 SITING

- <u>Clutter Extent</u>: Out to 100 nmi.

- <u>Radar Heights</u>:

  - Western Sector (west of Bar-Main) 5 to 1300 feet above MSL
  - Central Sector (Fox-2 to Bar-Main) 20 to 1300 feet above MSL
  - Eastern Sector (Labrador to Fox-2) 320 to 3400 feet above MSL

- <u>Clutter Type Mixture</u>:
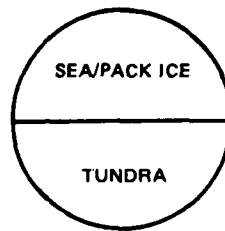
WESTERN SECTOR   CENTRAL SECTOR   EASTERN SECTOR

B.2 GROUND CLUTTER

B.2.1 <u>Discrete</u>

- <u>Distribution</u>: Uniform over 360 degrees within a 100-nmi radius of site.

RCS (dBm^2)	Hills/Mountains
60	1
50	2
40	7
30	10
20	10
10	10
0	10

B.2.2 **Distributed**

- **Radar Cross Section:** $RCS = \sigma_o A_c$

- **Clutter Cell Area:** $A_c = [R_c \ \tau/\sqrt{2}][\tan \theta /2]$

  where R_c = radar range

  τ = 2 x range resolution cell

  θ = 3 dB azimuth beamwidth

- **Distribution:** 315 uniformly distributed irregularly-shaped patches within 100 nmi of radar.

  240 areas of 20 $(nmi)^2$
  60 areas of 75 $(nmi)^2$
  15 areas of 300 $(nmi)^2$

- **Spatial Distribution:** Defined by Weibull p.d.f.

$$P(\sigma) = \frac{b(\ln 2)\sigma^{b-1}}{\sigma_m^b} \exp [-(\ln 2)(\sigma /\sigma_m)^b]$$

where σ_m = median value

b = shape parameter

	σ_m	b
- Tundra (P_1)	-50 dB	2.3
- Moderate Hills/Mountains (P_2)	-42 dB	3.3
- Severe Hills/Mountains (P_3)	-35 dB	3.2

- Region of Hills/Mountains: Half of patches defined by P_2, half by P_3

B.2.3 **Temporal Fluctuation**

- **Discrete Targets:** Non-fluctuating

- **Distributed Targets:** Rayleigh about a time-varying mean defined by spatial distribution.

B.2.4 **Power Spectral Density**

$$P(v) = 0.964 \ \delta(v) + \frac{0.705}{1+(v/0.023)^4}$$

where $\delta(v)$ = dirac delta function

v = velocity in m/sec

B.3 SEA/PACK ICE CLUTTER

B.3.1 Discrete

- Distribution: Uniform over 360 degrees within a 100-nmi radius of site.

RCS (dBm^2)	Icebergs
60	5
50	20
40	100
30	150
20	175
10	–
0	–

B.3.2 Distributed

- Radar Cross Section: $RCS = \sigma_o A_c$

- Clutter Cell Area: $A_c = [Rc^T/\sqrt{2}][\tan \theta/2]$

- Spatial Distribution:

$$P(\sigma) = \frac{b(\ln 2)\sigma^{b-1}}{\sigma_m b} \exp[-(\ln 2)(\sigma/\sigma_m)^b]$$

- Sea Parameters:

Radar Depression Angle (deg)	Frequency Band	σ_m Horizontal Polarization (dB)	σ_m Vertical Polarization (dB)	b
0.1	L	-65	-60	TBD
1.0	L	-50	-43	TBD
3.0	L	-46	-38	TBD
0.1	S	-53	-50	TBD
1.0	S	-42	-38	TBD
3.0	S	-37	-35	TBD

- Pack Ice Parameters:

    σ_m – TBD
    b – TBD

B.3.3 Temporal Fluctuation

- Icebergs: Non-fluctuating

- Distributed Targets: Rayleigh about a time-varying mean defined by spatial distribution.

B.3.4 Power Spectral Density

- Gaussian

- 3 dB width: 2.5 m/sec

- Mean Velocity: Any value between $\pm$ 2.5 meters/second

B.4 WEATHER CLUTTER

- Radar Cross Section: $RCS = \eta V_c$

- Clutter Cell Volume: $V_c = [\pi R^2/8][c\tau/2]\theta_1 \phi_1$

  where R = radar range
  $c\tau/2$ = range resolution cell
  θ_1 = 3 dB azimuth beamwidth
  ϕ_1 = 3 dB elevation beamwidth

- Reflectivity: $\eta = (6.12 \times 10^{-14})(r^{1.6}/\lambda^4)$ (meters $^{-1}$)

  where r = rainfall rate (mm/hr)
        λ = wavelength (meters)

- Attenuation Factor: $K = 0.02[3.2/f_{(GHz)}]^{2.8}[r]$ (dB/nmi)

- Altitude Extent of Precipitation:

	Arctic Circle (feet)	Labrador (feet)
-Cellular	0 to 6,000	0 to 10,000
-Uniform	0 to 6,000	0 to 10,000

- Bright Band of Uniform Rain: At maximum altitude.

- Bright Band Altitude Extent: 500 feet

- Edge Fall-off Rate for Cellular Precipitation: 7.14 mm/hr/nmi

- Uniform Rainfall Rate (mm/hr): Arctic Circle (1) - Labrador (2)

- Cellular Rainfall Rate (mm/hr): Arctic Circle (6) - Labrador (10)

- Bright Band Rainfall Rate (mm/hr): Arctic Circle (4) - Labrador (10)

- Number of Cells Within 100-nmi Radius: Arctic Circle (100) - Labrador (120)

- Diameter of Cells at Half Rainfall Rate (nmi): Arctic Circle (2.6) - Labrador (4.0)

- Circular Polarization Cancellation Ratio: 15 dB (rain)

- Power Spectral Density: Gaussian

    - standard deviation: $\sigma_v = 1.12[1 + 7.68\ R^2\phi^2]^{1/2}$

    where R = range (nmi)
    ϕ = vertical beamwidth (rad)

    - mean velocity: Any value between ± 25 meters/second

B.5 BIRD CLUTTER

B.5.1 Distributed

Individual birds acting independently in search of food.

- Location: Coastal regions, 50 nmi inland to 20 nmi off-shore

- RCS of Individual Bird: 0.02 meter^2

- Number of Birds per Square Mile: 20,000

- Bird Height Above Local Surface: Uniformly distributed between 25 and 500 feet

B.5.2 Discrete

Migrating birds

- Migration Period: May-June and August-September

- Number of Flocks: 350 uniformly distributed within 60-nmi radius from radar site

- Composition of Flock: 70% eider, 20% pintail, 10% lesser snow geese

- Flock Shape and Dimensions:

  - eider: long wavy line (applies to western Canada sites and represents peak flock load); length is 50 to 3000 feet.

  - pintail: wavy line; length is 100 to 300 feet

  - lesser snow geese: U-shaped and oblique line; length is 200 to 3000 feet

- Ground Speed Distribution: Approximately Gaussian

  - mean: 45 knots

  - standard deviation: 7 knots

- Height Distribution:

  - eider: 50% < 80 feet; 99% < 140 feet

  - pintail: to be determined

  - lesser snow geese: 50% < 3000 feet; 99% < 6000 feet

- Flock RCS: (See figure B-1.) Slow fluctuation rate with RCS constant from pulse-to-pulse within beamwidth, independent from scan-to-scan.

B.5.3 Temporal Fluctuation

- Discrete Bird Clutter: Does not fluctuate from pulse-to-pulse; has Rayleigh fluctuation from scan-to-scan

- Distributed Clutter: Rayleigh about a time-varying mean defined by the spatial distribution

B.5.4 Power Spectral Density

Gaussian (for distributed bird clutter)

- Standard Deviation:
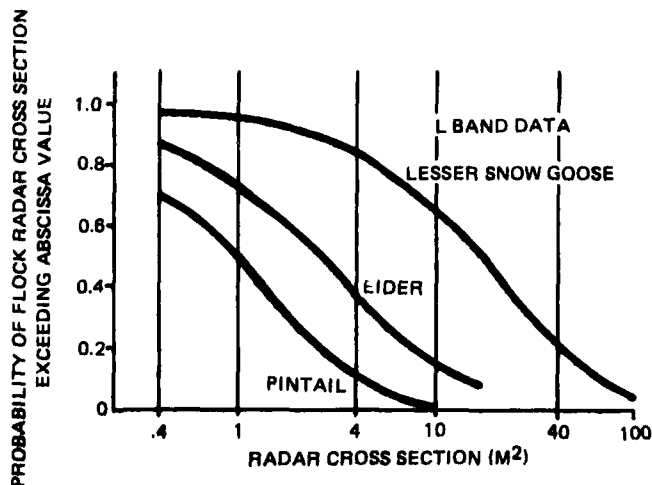 $$\sigma_V = 1.12 \ (1 + 7.68R^2\phi^2)^{1/2}$$

- Mean Velocity: TBD

Figure B-1. Flock Radar Cross Section

146

Appendix C

DERIVATION OF TRACK MAINTENANCE PROBABILITY CRITERIA

Define   "0"   as a missed detection
        "1"   as a detection
        P as the scan detection probability
        Q as $1-P$
        P_0 as the probability of being in a "0" state and still maintaining track
        P_1 as the probability of being in a "1" state and still maintaining track
        P_{MT} as the probability of maintaining track
        n as the scan number.

For a 2-consecutive miss criterion:

$$P_{MT}(n) = P_0(n) + P_1(n)$$

$$P_0(n) = P_1(n-1) \times Q$$

$$P_1(n) = P_0(n-1) \times P + P_1(n-1) \times P$$

$$= P[P_0(n-1) + P_1(n-1)]$$

$$P_1(n) = P\, P_{MT}(n-1)$$

$$P_0(n) = Q\, P_1(n-1) = Q\, P\, P_{MT}(n-2)$$

$$\therefore P_{MT}(n) = Q\, P\, P_{MT}(n-2) + P\, P_{MT}(n-1)$$

$$= P\,[Q\, P_{MT}(n-2) + P_{MT}(n-1)]$$

$$P_{MT}(n+2) = P[Q\, P_{MT}(n) + P_{MT}(n+1)] \quad \text{2-consecutive miss criterion}$$

$$\begin{array}{ccc} \underline{n-1} & & \underline{n} \\ & Q & \\ 1 & \longrightarrow & 0 \\ & P & \\ 0 & \longrightarrow & 1 \\ & P & \\ 1 & \longrightarrow & 1 \end{array}$$

Initial conditions: $P_0(1) = 0$

$$P_1(1) = 1$$

$$P_{MT}(1) = 1$$

$$P_{MT}(2) = 1$$

For a 3-consecutive miss criterion:

$$P_{MT}(n) = P_0(n) + P_1(n)$$

$$
\begin{array}{ccc}
n-2 & n-1 & n \\
 & P & \\
\end{array}
$$

$$P_1(n) = P_0(n-1) \times P + P_1(n-1) \times P \qquad 0 \xrightarrow{P} 1$$

$$= P[P_0(n-1) + P_1(n-1)] \qquad 1 \xrightarrow{P} 1$$

$$P_0(n) = P_1(n-2) \times Q \times Q + \qquad 1 \xrightarrow{Q} 0 \xrightarrow{Q} 0$$

$$P_0(n-2) \times P \times Q + \qquad 0 \xrightarrow{P} 1 \xrightarrow{Q} 0$$

$$P_1(n-2) \times P \times Q \qquad 1 \xrightarrow{P} 1 \xrightarrow{Q} 0$$

$$= P_1(n-2)[Q^2 + PQ] + PQP_0(n-2)$$

$$= Q\underset{1}{\underbrace{(Q+P)}} P_1(n-2) + PQP_0(n-2)$$

$$= QP_1(n-2) + PQP_0(n-2)$$

$$P_0(n) = Q[P_1(n-2) + PP_0(n-2)]$$

$$P_{MT}(n+3) = P_0(n+3) + P_1(n+3)$$

$$= Q[P_1(n+1) + PP_0(n+1)] + P[P_0(n+2) + P_1(n+2)]$$

$$= QP[P_0(n) + P_1(n)] + PQP_0(n+1) + P[P_{MT}(n+2)]$$

$$= PQP_{MT}(n) + PQP_0(n+1) + PP_{MT}(n+2)$$

$$P_0(n+1) = P_{MT}(n+1) - P_1(n+1)$$

$$= P_{MT}(n+1) - P[P_0(n) + P_1(n)] = P_{MT}(n+1) - PP_{MT}(n)$$

$$P_{MT}(n+3) = PQP_{MT}(n) + PQ[P_{MT}(n+1) - PP_{MT}(n)] + PP_{MT}(n+2)$$

$$= PQP_{MT}(n) + PQP_{MT}(n+1) - P^2QP_{MT}(n) + PP_{MT}(n+2)$$

$$= (PQ-P^2Q) P_{MT}(n) + PQP_{MT}(n+1) + PP_{MT}(n+2)$$

$$= PQ\underset{Q}{\underbrace{(1-P)}}P_{MT}(n) + PQP_{MT}(n+1) + PP_{MT}(n+2)$$

$$P_{MT}(n+3) = P\left\{Q^2 P_{MT}(n) + QP_{MT}(n+1) + P_{MT}(n+2)\right\} \begin{array}{l}\text{3-consecutive}\\ \text{miss criterion}\end{array}$$

Initial conditions: $P_0(1) = 0$

$$P_1(1) = 1$$

$$P_{MT}(1) = P_{MT}(2) = P_{MT}(3) = 1$$

Appendix D

KALMAN FILTER STRUCTURE

D.1 STATE SPACE COORDINATES AND MEASUREMENT NON-LINEARITY

The Kalman filter structure is partly dependent on the particular co-ordinate system used to characterize target dynamics in the state space equation. The choice significantly influences the nature of the non-linearities in the system equations.

The measurements provided by the RRAS baseline radar include target range (R), azimuth (B), and elevation (E) - although there are only three beams providing elevation data. The concept of coordinate may be generalized to encompass all linear and non-linear combinations of these measurements. Let $\underline{z}^T = [\ R\ B\ E\ ]$. Then, the coordinates of the plant can be represented as $\underline{x}^* = \underline{f}\ (\underline{z})$, where $\underline{x}^*$ is the vector of selected coordinates (a subset of the state vector), $\underline{z}$ is the three-dimensional measurement vector, and $\underline{f}$ is a vector-valued mapping. Given that $\underline{f}$ is one-one and onto, then the inverse function exists and (notationally) $\underline{z} = \underline{f}^{-1}\ (\underline{x}^*)$ - this defines the non-linear function ($\underline{h}$) in the measurement equation.

It is usual to select physically meaningful coordinates. The major options in this case are a polar (R,B,E) or a Cartesian (R_x, R_y, R_z) coordinate f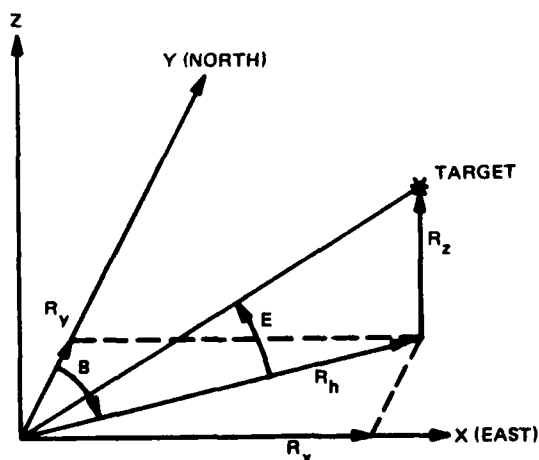rame. Since the primary targets of interest may be generally categorized as penetrators with crossing trajectories, the state space coordinates were selected to be an (x,y,z) orthogonal triad. This notation denotes a Cartesian coordinate frame with origin at the radar and with x axis directed east, y axis directed north, and z axis up (i.e., along the local vertical). This particular system was selected because of all the viable candidates, it permits a simple, efficient, and (possibly) the most accurate representation of target dynamics.

Figure D-1 depicts the relationship between the measurement coordinates, $\underline{z}^T = [R\ B\ E]$, and the state space coordinates, $X^{*T} = [R_x R_y R_z]$.

Figure D-1. Coordinate Frames and Measurement Non-Linearity

149

'From figure D-1,

$$\underline{X}^* = \underline{f}\ (\underline{Z}) = \begin{bmatrix} R_x \\ \\ R_y \\ \\ R_z \end{bmatrix} = \begin{bmatrix} R \cos E \sin B \\ \\ R \cos E \cos B \\ \\ R \sin E \end{bmatrix}$$

$$\underline{Z} = \underline{f}^{-1}\ (\underline{X}^*) = \begin{bmatrix} R \\ \\ B \\ \\ E \end{bmatrix} = \begin{bmatrix} [R_x^2 + R_y^2 + R_y^2]^{1/2} \\ \\ \tan^{-1}\ (R_x/R_y) \\ \\ \sin^{-1}\left[R_z/(R_x^2 + R_y^2 + R_z^2)^{1/2} \right] \end{bmatrix}$$

The Jacobian of the measurement non-linearity is required by the extended Kalman filter algorithm (table D-1). It is a 3 x 3 matrix with the (i, j) element equal to

$\partial f_i^{-1}/\partial x^*_j$. The Jacobian can be written as follows:

$$\left[\partial f_i^{-1}/\partial x^*_j \right] = \begin{bmatrix} R_x/R & R_y/R & R_z/R \\ \\ R_y/R_H^2 & -R_x/R_H^2 & 0 \\ \\ -R_x R_y/R_H R^2 & -R_y R_z/R_H R^2 & R_H/R^2 \end{bmatrix}$$

where $R_H = [R_x^2 + R_y^2]^{1/2}$

Table D-1.   Extended Kalman Filter Algorithm

State Space Equation: $x(t_{k+1}) = \Phi[x(t_k)] + \Gamma[x(t_k)] u(t_k)$

Measurement Equation: $z(t_k) = h[x(t_k)] + v(t_k)$

For convenience of notation, dependence of Φ, Γ, h on t_k has been suppressed.   Now, let

$$E[u(t_k)] = E[v(t_k)] = 0$$

$$cov[u(t_k), u(t_j)] = Q(t_k) \delta_{kj}$$

$$cov[v(t_k), v(t_j)] = R(t_k) \delta_{kj}$$

$$cov[v(t_k), u(t_j)] = 0$$

ALGORITHM

Time Update:

$$\hat{x}[t_k/t_{k-1}] = \Phi \left\{ \hat{x}[t_{k-1}/t_{k-1}] \right\}$$

$$P[t_k/t_{k-1}] = \phi_x \left\{ \hat{x}[t_{k-1}/t_{k-1}] \right\} P[t_{k-1}/t_{k-1}] \Phi_x^T \left\{ \hat{x}[t_{k-1}/t_{k-1}] \right\}$$

$$+ \Gamma \left\{ \hat{x}[t_{k-1}/t_{k-1}] \right\} Q[t_{k-1}] \Gamma^T \left\{ \hat{x}[t_{k-1}/t_{k-1}] \right\}$$

Gain:

$$K[t_k] = P[t_k/t_k] h_x \left\{ \hat{x}[t_k/t_{k-1}] \right\}$$

$$* \left\{ h_x \left[\hat{x}[t_k/t_{k-1}] \right] P[t_k/t_{k-1}] h_x^T \left[\hat{x}[t_k/t_{k-1}] \right] + R[t_k] \right\}^{-1}$$

Measurement Update:

$$x[t_k/t_k] = x[t_k/t_{k-1}] + K[t_k] \left\{ z[t_k] - h \left[\hat{x}[t_k/t_{k-1}] \right] \right\}$$

$$P[t_k/t_k] = \left\{ I - K[t_k] h_x \left[\hat{x}[t_k/t_{k-1}] \right] \right\} * P[t_k/t_{k-1}]$$

$$\phi_x \left[\hat{x}[t_k] \right]_{ij} = \left. \frac{\partial \Phi_i}{x_j} \right|_{x(t_k)} \overset{\Delta}{=} \text{Jacobian of } \Phi$$

$$h_x \left[\hat{x}[t_k] \right]_{ij} = \left. \frac{\partial h_i}{\partial x_j} \right|_{x(t_k)} \overset{\Delta}{=} \text{Jacobian of } h$$

D.2. STATE SPACE EQUATION AND PLANT NOISE VECTOR

In this case, the state space equation is based on a kinematic model of target motion. The state vector, then, generally consists of elements which define target position ($\underline{X}^*$, the selected state space coordinates), as well as related higher derivatives (velocity, acceleration, etc.). It is assumed here that zero mean random accelerations act on the targets of interest to cause perturbations from a straight line trajectory.

Because of the computational implications, it is desirable to select a state vector of minimal dimension. For example, only those states which are observable, given the available measurements and measurement rate, need be included. A five-state structure was considered adequate for studies with the RRAS baseline radar; the state vector is specifically defined as $\underline{X}^T =$ $[R_x \; V_x \; R_y \; V_y \; R_z]$, where V_x, V_y represent target northerly and easterly velocities, respectively. Estimates of these five states provide sufficient data to compute (smoothed) target range, bearing, elevation, heading, and horizontal velocity, i.e., the desired outputs. The observ-ability of target motions in the Z axis is dependent on radar elevation measurements. Since only three elevation beams are used in the RRAS baseline radar, there is relatively little information available to form accurate estimates of R_z, much less of higher derivatives of Z motions. Vertical (Z) velocity/acceleration states were therefore not included in the state vector; neither were horizontal axis accelerations. The ability to generate useful estimates of target horizontal accelerations depends not only on the accuracy of radar measurements, but also on the measurement rate and the statistics of target accelerations. For example, if the correlation time of target ac-celerations is significantly larger than the time between (accurate) measurements, then the use of acceleration states may be warranted. This situation pertains to tactical tracking radars where target acceleration es-timates are desired for accurate gun fire control. However, the scan time in the RRAS baseline radar is 4 seconds, and penetrating targets may not main-tain turns over much longer time periods. The inclusion of horizontal ac-celerations in the state vector is not considered useful under these cir-cumstances, and such states are not ordinarily included in a surveillance radar system. Of course, the exclusion of these acceleration states also re-sults in a saving of at least 2 states - with favorable implications on the computational burden.

Selection of the indicated state vector results in a linear, time-invari-ant transition matrix, i.e., from table D-1: $\Phi \; [\underline{x}(t_k),t_k] = \emptyset \; (t_{k+1}$ $-t_k) \; \underline{x}(t_k)$ and the Jacobian of Φ is $\emptyset$. The influence of target acceleration on the modeled states is incorporated into the state space equation via the plant noise vector. Several alternate filter configurations can be defined, based on assumptions as to the statistical nature of the accelerations. These configurations result in variations in the Q and Γ matrices (table D-1). Three particular variants were used in the simulation studies.

- Configuration I. The accelerations in the x, y axes were modeled as independent, zero mean, random processes. In particular, the ac-celeration in each of these axes was represented as a continuous white Gaussian process. Figure D-2 provides a block diagram of the

(continuous) target model used in this case. The discretized system equations are also shown.

- Configuration II. This is the same as in configuration I, except that the x, y axis accelerations are modeled as a discrete white Gaussian time series, i.e., the accelerations are constant over each scan period with Gaussian distributed magnitude, and the value in an interval is independent of the value in any other interval. The discrete system equations used in this case are given in figure D-3.

- Configuration III. In contrast to configuration I and II, target accelerations are assumed to occur in a track-oriented coordinate system, i.e., accelerations are directed along and are orthogonal to the velocity vector. As in configuration II, these accelerations are modeled as independent discrete white noise sequences. The associated system equations are shown in figure D-3. Note that the distribution matrix (Γ) is dependent on target heading. As indicated in table D-1, state estimates are used to compute the required terms in the extended Kalman filter algorithm. This configuration is considered to provide the most realistic representation of target dynamics. In contrast to configurations I and II, it provides the flexibility to distinguish between the relatively low level accelerations along the velocity vector (speed changes) and the higher level lateral accelerations (associated with turn maneuvers). This configuration is proposed for the baseline system.

D.3 MEASUREMENT ERRORS

Under ideal circumstances (high P_D), the baseline radar may be considered to be a quantizer,[1,2] i.e., it provides range, bearing, and elevation measurements which indicate the region (rather than the point) in which the target is located. The presence of quantized measurements represents a specialized type of non-linearity not amenable to the quasi-linear approach outlined in table D-1. (That approach uses the Jacobian of the non-linearity; however, the slope of the staircase quantization non-linearity is either zero or infinite.) Optimal estimators for systems involving quantized measurements have been examined in the literature.[2,3,4] Even the assumption of Gaussian distributions can lead to significant increases in algorithm computational requirements. The commonly used approach is to assume that quantization noise (quantizer output minus input) is uncorrelated

- - - - - - -

[1]A quantizer is any zero memory input-output device that designates the interval or intervals in which its input lies.[2]

[2]R.E. Curry, Jr., Estimation and Control with Quantized Measurements, TE-23, MIT PhD Thesis, May 1968.

[3]K.A. Clements, Optimal Recursive Filtering of Quantized Data, PhD Thesis, Polytechnic Institute of Brooklyn, 1970.

[4]J.C. Keenan, Estimation with Quantized Measurements, PhD Thesis, Penn State University, 1974.

DISCRETIZATION

From the figure:

$$\dot{x}_1 = x_2 + \eta_1$$
$$\dot{x}_2 = \eta_2$$
$$\dot{x}_3 = x_4 + \eta_3$$
$$\dot{x}_4 = \eta_4$$
$$\dot{x}_5 = \eta_5$$

Let $\quad \underline{x}^T = [x_1 \; x_2 \; x_3 \; x_4 \; x_5]$

$\quad\quad \underline{\eta}^T = [\eta_1 \; \eta_2 \; \eta_3 \; \eta_4 \; \eta_5]$

then $\quad \underline{\dot{x}} = A\underline{x} + \underline{\eta}$

and $\quad \underline{x}(t_1 + \tau) = \emptyset(\tau)\underline{x}(t_1) + \underline{u}(t_1)$

where $\quad \underline{u}(t_1) = \displaystyle\int_{t_1}^{t_1+\tau} \emptyset(t_1 + \tau - \lambda)\,\underline{\eta}(\lambda)\,d\lambda = \emptyset(\tau)\int_{t_1}^{t_1+\tau} \Phi(t_1 - \lambda)\underline{\eta}(\lambda)\,d\lambda$

$$\emptyset(\tau) = \begin{bmatrix} 1 & \tau & 0 & 0 & 0 \\ 0 & 1 & 0 & 0 & 0 \\ 0 & 0 & 1 & \tau & 0 \\ 0 & 0 & 0 & 1 & 0 \\ 0 & 0 & 0 & 0 & 1 \end{bmatrix}$$

NOTE: The Γ matrix of table D-1 is the identity matrix for this configuration

$\underline{\eta} \overset{\Delta}{=}$ continuous, white Gaussian, zero-mean, independent vector random process

$\therefore \; \text{cov}[\underline{\eta}(t_1)\underline{\eta}^T(t_j)] = \psi\,\delta\,(t_1 - t_j)$

where $\psi = $ diagonal $[\sigma_1^2 \quad \sigma_2^2 \quad \sigma_3^2 \quad \sigma_4^2 \quad \sigma_5^2]$

$Q = E\,[\underline{u}(t_1)\underline{u}^T(t_1)]$: a symmetric matrix

$Q_{11} = \sigma_1^2\,\tau + \sigma_2^2\tau^3/3 \quad\quad Q_{34} = \sigma_4^2\,\tau^2/2 = Q_{43}$

$Q_{12} = \sigma_2^2\,\tau^2/2 = Q_{21} \quad\quad Q_{44} = \sigma_4^2\,\tau$

$Q_{22} = \sigma_2^2\,\tau \quad\quad\quad\quad\quad\quad Q_{55} = \sigma_5^2\,\tau$

$Q_{33} = \sigma_3^2\,\tau + \sigma_4^2\,\tau^3/3$

Other off-diagonal Q terms are zero.

Figure D-2. Configuration I,
Block Diagram

Discrete State Equation

$$x(t_{k+1}) = \phi(\tau) \, x(t_k) + \Gamma[x(t_k), t_k] \, u(t_k)$$

where $\tau = t_{k+1} - t_k$

Configuration II:

$$x^T = [R_x \; V_x \; R_y \; V_y \; R_z]$$

$$u^T = [\eta(V_x) \; \eta(A_x) \; \eta(V_y) \; \eta(A_y) \; \eta(V_z)]$$

$$\phi(\tau) = \begin{bmatrix} 1 & \tau & 0 & 0 & 0 \\ 0 & 1 & 0 & 0 & 0 \\ 0 & 0 & 1 & \tau & 0 \\ 0 & 0 & 0 & 1 & 0 \\ 0 & 0 & 0 & 0 & 1 \end{bmatrix} \qquad \Gamma = \begin{bmatrix} \tau & \tau^2/2 & 0 & 0 & 0 \\ 0 & \tau & 0 & 0 & 0 \\ 0 & 0 & \tau & \tau^2/2 & 0 \\ 0 & 0 & 0 & \tau & 0 \\ 0 & 0 & 0 & 0 & \tau \end{bmatrix}$$

Configuration III:

$$x^T = [R_x \; V_x \; R_y \; V_y \; R_z]$$

$$u^T = [\eta(V_x) \; \eta(A_t) \; \eta(V_y) \; \eta(A_m) \; \eta(V_z)]$$

$A_t \overset{\Delta}{=}$ acceleration directed along the velocity vector (speed change)

$A_m \overset{\Delta}{=}$ acceleration orthogonal to velocity vector (turn maneuvers)

$$\phi(\tau) = \begin{bmatrix} 1 & \tau & 0 & 0 & 0 \\ 0 & 1 & 0 & 0 & 0 \\ 0 & 0 & 1 & \tau & 0 \\ 0 & 0 & 0 & 1 & 0 \\ 0 & 0 & 0 & 0 & 1 \end{bmatrix}$$

$$\Gamma = \begin{bmatrix} \tau & (\tau^2/2)\sin\theta_{HO} & 0 & (\tau^2/2)\cos\theta_{HO} & 0 \\ 0 & \tau\sin\theta_{HO} & 0 & \tau\cos\theta_{HO} & 0 \\ 0 & (\tau^2/2)\cos\theta_{HO} & \tau & -(\tau^2/2)\sin\theta_{HO} & 0 \\ 0 & \tau\cos\theta_{HO} & 0 & -\tau\sin\theta_{HO} & 0 \\ 0 & 0 & 0 & 0 & \tau \end{bmatrix}$$

$\theta_{HO} \overset{\Delta}{=}$ velocity vector direction relative to north at $t = t_k$

Γ matrix based on first order approximations

Figure D-3. ϕ, Γ Matrices for
Configurations II and III

observation noise with variance equal to the variance of a uniform error
distribution in that interval. It has been shown that this technique
provides similar performance to an approximate non-linear estimator based on
a truncated power series expansion. (The power series approach neglects
fourth and higher order terms, and is especially suitable to cases where the
quantum-interval-to-standard-deviation ratio is small.) This simplified
approach was essentially used in the simulation to generate the (diagonal)
elements of the measurement noise (R) matrix required in the algorithm (table
D-1). The quantization intervals span ± 75 meters in range, and ± 0.75 degree
in azimuth. The elevation quantization intervals are non-uniform; they are
$(0°, 5°)$, $(5°, 8°)$, $(8°, 15°)$, $(15°, 18°)$, $(18°, 30°)$.

D.4 INITIALIZATION

Use of the Kalman recursive algorithm requires initialization of the
state vector and of the covariance matrix. Two sets of measurements (at $t = t_{-1}$ and $t = t_0$) are required for initialization. The most recent range,
bearing, elevation data are used to compute target position in Cartesian
coordinates and to initialize corresponding terms of the state vector. The
(x, y) velocity states are initialized by using the difference between
indicated position at t_{-1} and t_0.

Appendix E

WEIBULL DENSITY AND DISTRIBUTION FUNCTIONS

E.1 WEIBULL DENSITY FUNCTION

$$p(V) = a\rho(\rho V)^{a-1} e^{-(\rho V)^a}, \ V > 0$$

$$p(V) = 0, \ V < 0$$

where ρ and a are constants

E.2 WEIBULL DISTRIBUTION FUNCTION

$$P = P(V > V_n) = e^{-(\rho V_n)^a}$$

$$\ln[1/P] = (\rho V_n)^a$$

If power is normalized to unity, $\overline{V^2} = 1$ (see figures 36, 37, and 38).

Then $$E[V^2] = \frac{\Gamma[(2/a)+1]}{\rho^2} = 1$$

where $$\Gamma(x) = \int_0^\infty t^{x-1} e^{-t} \, dt \quad \text{and} \quad \rho = \sqrt{\Gamma[(2/a)+1]}$$

CONTRIBUTORS

System

F.J. Scire (principal investigator)

J.H. Chin

W.H. Heiss

R.E. Mulno

R.S. Pierro

C.P. SanGiovanni

Subsystems

J.P. Garilli

G.L. Hanley

I.R. Hoxie

A.M. Kerdock

R.R. Moxham

J.A. O'Hare

C. Rothenberg

R.D. Viola

Simulation

W.R. Hanley

N. Frush

F. Herman

L.J. Lawdermilt

J. Protola

MISSION
of
Rome Air Development Center

RADC plans and executes research, development, test and selected acquisition programs in support of Command, Control Communications and Intelligence (C^3I) activities. Technical and engineering support within areas of technical competence is provided to ESD Program Offices (POs) and other ESD elements. The principal technical mission areas are communications, electromagnetic guidance and control, surveillance of ground and aerospace objects, intelligence data collection and handling, information system technology, ionospheric propagation, solid state sciences, microwave physics and electronic reliability, maintainability and compatibility.